UNIVERSITY OF CALIFORNIA, SAN DIEGO

Multiscale Simulations of Biochemically Reacting Systems

A dissertation submitted in partial satisfaction of the
requirements for the degree Doctor of Philosophy
in
Chemistry

by

Yuhui Cheng

Committee in charge:

Professor J. Andrew McCammon, Chair
Professor Gourisankar Ghosh
Professor Michael J. Holst
Professor John H. Weare
Professor Peter Wolynes

2007

The dissertation of Yuhui Cheng is approved, and it is acceptable in quality and form for publication on microfilm:

_____

_____

_____

_____

_____

Chair

University of California, San Diego

2007

This dissertation is dedicated to my beloved grandmother Zuying Min, on the occasion of her 80th birthday.

TABLE OF CONTENTS

LIST OF TABLES

LIST OF FIGURES

ACKNOWLEDGEMENTS

Over the years as I have grown up, it has been my good fortune to encounter many people who have given me their time, companionship, professional and personal help, and above all: patience.

Most importantly, I wish to say "xiexie" to my PhD advisor, J. Andrew McCammon for his patient guidance in my graduate studies. First of all, due to his constant financial support, I can finish my graduate study. His profound wisdom in science opens the door to succeed in my future career. I am much indebted to him for introducing me to the topic of structure-based system biology, as well as his encouragement and continued guidance specifically. Furthermore, I highly appreciate his continuous encouragement, support and mentoring for my English skills during the past five years. I must also mention all the time and energy he spent on improving my English writing and proofreading all my manuscripts, including this dissertation.

Next, I would like to thank my other advisor, Michael Holst. His excellent finite element tool kit provides me the powerful programming libraries, and he has been a patient tutor to guide me into applied mathematics. The inspiring and interesting discussions with him over phone and at his office shape my understanding of numerical applications on biological simulations.

I want to thank all the members in McCammon and Holst groups. During the past five years in UCSD, I have gained lots of help from them. Especially, I would like to thank Prof. Yingkai Zhang, Nathan Baker and Steven Bond, Dr. Jason Suen, Xiaolin Cheng, Zeyun Yu, Benzhuo Lu, Yongcheng Zhou, and Deqiang Zhang for being great friends, collabortors, proof-reading of my papers and some even role models during my graduate studies. I also thank Dr. Donald Hamelberg and Robert Konecny for administrating the computer resources. Meanwhile, I thank all of my collaborators: Prof. Palmer Taylor and Dr. Zoran Radić, Prof. Chandrajit L. Bajaj and Dr. Yongjie Zhang for their trust in collaborating with me. Finally, I appreciate Wilfred Li and Christopher Misleh to manage the computer resource for NBCR.

I am, of course, particularly indebted to my family for their unwavering love and encouragement. Specifically I thank my parents, who provided for all my needs, since the earliest years. Their unselfish love inspires my success in the graduate school.

Last but not least, I would like to thank my girl friend Yuhan, for her love, patience

and encouragements during writing my dissertation.

Chapter I contains material from "How Does the cAMP-Dependent Protein Kinase Catalyze the Phosphorylation Reaction: an *ab initio* QM/MM Study" published in 2005 in *J. Am. Chem. Soc.* (Volumn 127, pages 1553-1562), authored by Yuhui Cheng, Yingkai Zhang, and J. Andrew McCammon;" How does activation loop phosphorylation modulate catalytic activity in the cAMP-dependent protein kinase: A Theoretical Study" published in 2006 in *Protein Science* (Volumn 15, pages 672-683), authored by Yuhui Cheng, Yingkai Zhang, and J. Andrew McCammon; "Acetylcholinesterase: Mechanisms of Covalent Inhibition of Wild-type and H447I Mutant Determined by Computational Analyses" published in 2007 in *J. Am. Chem. Soc.* (Volumn 129, pages 6562-6570), authored by Yuhui Cheng, Xiaolin Cheng, Zoran Radić, and J. Andrew McCammon.

Chapter II is taken from "Finite Element Analysis of the Time-Dependent Smoluchowski Equation for Acetylcholinesterase Reaction Rate Calculations" published in 2007 in *Biophys. J.* (Volumn 92, pages 3397-3406), authored by Yuhui Cheng, Jason K. Suen, Deqiang Zhang, Stephen D. Bond, Yongjie Zhang, Yuhua Song, Nathan A. Baker, Chandrajit L. Bajaj, Michael J. Holst, and J. Andrew McCammon.

Chapter III is adapted from "Continuum Simulations of Acetylcholine Diffusion with Reaction-determined Boundaries in Neuromuscular Junction Models" published in 2007 in *Biophys. Chem.* (Volumn 127, pages 129-139), authored by Yuhui Cheng, Jason K. Suen, Zoran Radić, Stephen D. Bond, Michael J. Holst and J. Andrew McCammon.

All material has been reproduced with the consent of all other authors.

–Yuhui Cheng

VITA

February 20, 1978	Born, Yicheng, Hubei, P. R. China
1997-2002	Department of Chemical Physics University of Science and Technology of China
2004	Master of Science, University of California, San Diego
2007	Doctor of Philosophy, University of California, San Diego

PUBLICATIONS

Yuhui Cheng, Xiaolin Cheng, Zoran Radić, and J. Andrew McCammon, Acetylcholinesterase: Mechanisms of Covalent Inhibition of Wild-type and H447I Mutant Determined by Computational Analyses, J. Am. Chem. Soc, 2007, 129: 6562-6570.

Yuhui Cheng, Jason K. Suen, Deqiang Zhang, Stephen D. Bond, Yongjie Zhang, Yuhua Song, Nathan A. Baker, Chandrajit L. Bajaj, Michael J. Holst, and J. Andrew McCammon, Finite Element Analysis of the Time-Dependent Smoluchowski Equation for Acetylcholinesterase Reaction Rate Calculations, Biophys. J., 2007, 92: 3397-3406.

Yuhui Cheng, Jason K. Suen, Zoran Radić, Stephen D. Bond, Michael J. Holst and J. Andrew McCammon, Continuum Simulations of Acetylcholine Diffusion with Reaction-determined Boundaries in Neuromuscular Junction Models, Biophys. Chem., 2007, 127: 129-139.

Kai Wei, Lei, Liu, **Yuhui Cheng**, Yao Fu and Qing-Xiang Guo, Theoretical study of the mechanism of HDV ribozyme self-cleaving reaction, J. Phys. Chem. B, 2007, 111: 1514-1516.

Sanjib Senapati, **Yuhui Cheng**, and J. Andrew McCammon, "Why is the syn isomer of TZ2PA6 the sole product of "click chemistry" in the acetylcholinesterase environment", J. Med. Chem. 2006, 49: 6222-6230.

Yuhui Cheng, Yingkai Zhang, and J. Andrew McCammon, How does activation loop phosphorylation modulate catalytic activity in the cAMP-dependent protein kinase: A Theoretical Study, Protein Science. 2006, 15: 672-683.

Yuhui Cheng, Yingkai Zhang, and J. Andrew McCammon, How Does the cAMP-Dependent Protein Kinase Catalyze the Phosphorylation Reaction: an *ab initio* QM/MM Study, J. Am. Chem. Soc. 2005, 127: 1553-1562.

Yuhui Cheng, Yao Fu, Lei Liu, Qing-Xiang Guo, Substituent effects on the hydrogen bonding between 4-substituted phenols and HF, H_2O, NH_3, Chinese Journal of Chemistry, 2003, 21: 1433-1439

Yuhui Cheng, Lei Liu, Yao Fu, Rong Chen, Xiao-Song Li, Qing-Xiang Guo, Counterion effects on the cation-pi interaction between alkaline earth cations and benzene, J. Phys. Chem. A, 2002, 106: 11215-11220.

Yuhui Cheng, Xing Zhao, Ke-Sheng Song, Lei Liu, Qingxiang Guo, Remote substituent effects on bond dissociation energies of para-substituted aromatic silanes, J. Org. Chem., 2002, 67: 6638-6645.

Yuhui Cheng, Ying Fang, Xing Zhao, Lei Liu, Qing-Xiang Guo, A theoretical study of the substituent effects on the P-X (X = H, F, Cl) bond dissociation energies in para- and meta-substituted aromatic phosphines, Bull. Chem. Soc. Jpn., 2002, 75: 1715-1722.

Yuhui Cheng, Lei Liu, Ke-Sheng Song, Qing-Xiang Guo, A theoretical study on the homolytic dissociation energies of H-N^+ bonds, J. Chem. Soc. Perkin Trans. II, 2002, 2: 1406-1411.

FIELDS OF STUDY

Major Field: Biophysical Chemistry

Studies in computational modeling for biochemically reacting systems,
Professor J. Andrew McCammon

ABSTRACT OF THE DISSERTATION

Multiscale Simulations of Biochemically Reacting Systems

by

Yuhui Cheng
Doctor of Philosophy in Chemistry
University of California, San Diego, 2007
Professor J. Andrew McCammon, Chair

My work focuses on gaining a deeper understanding on the catalytic mechanism of enzymes and reaction-diffusion relations in various biological systems, using computational methods and theories. It is of profound interest and great practical value to explore the physical and biological chemistry of drug diffusion and binding at multiple time and size scales. For example, it helps us understand why a drug can or cannot bind with the mutation(s) of its target protein, how efficient the binding process is and how we can design synthetic receptors to serve as drug carriers or to separate chemical mixtures. A brief summary of this dissertation is as follows.

Combined quantum mechanics and molecular mechanics (QM/MM) and molecular dynamics (MD) have enabled probing the potential surface accurately in various enzymatic reactions. For an unusual residue or drug molecule, the RESP charge parameters were first prepared with quantum mechanics calculations. Since the resolution of the X-ray crystal structures were not high enough to determine the protonated state of each residue, pKa calculations were carried out. Then molecular dynamics was used to study the conformational changes of the enzymes. Finally, QM/MM studies were conducted to calculate the reaction barrier and even the free energy path.

When I was in the Laboratory of Biomass Clean Energy (BCEL) at University of Science and Technology of China, I focused on studying the stability of various radicals, π-cation interactions and the reaction mechanisms in several organic reactions, using the quantum chemistry [12]. This experience provided the fundamental base for my first PhD project, *ab initio* QM/MM studies on the catalytic subunit of cAMP-Dependent Protein Kinase (PKA) (Chapter I). The QM/MM calculations confirmed that the phosphorylation reaction catalyzed by PKA is mainly dissociative, and Asp166 serves as the catalytic base to accept the proton delivered by

the substrate peptide. Furthermore, we have studied the effects of the residues on the reaction barrier using the QM/MM free energy perturbation theory, and analyzed the role of the phosphorylated Thr-197 in the activation segment. We have found that pThr-197 not only facilitates the phosphoryl transfer reaction by stabilizing the transition state through electrostatic interactions, but also strongly affects the functional protein dynamics as well as the active site conformation. Similarly, we have carried out QM/MM calculations to explore the reaction mechanism in both the wild-type and His447Ile mouse acetylcholinesterase (mAChE). Our studies indicated that the catalytic base His447 can be replaced with the catalytic water molecule in the binding of some inhibitors to the mAChE.

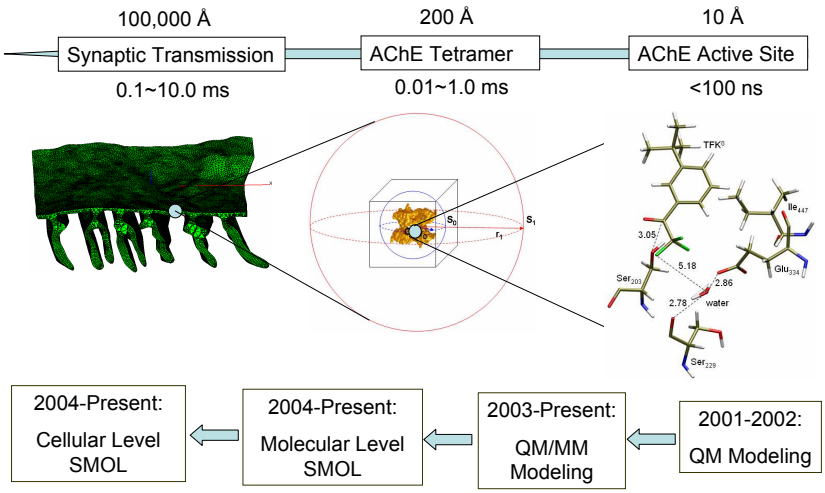

Figure .1: My research projects at three different level in the graduate school.

Although the QM/MM and MD methods can play important roles in determining reaction mechanisms, as well as the motion and folding of the protein, these methods are still quite expensive to probe larger spatial and time scale problems, such as modeling the synaptic transmission and determining the ligand association rate constant k_{on}, as shown in the first and second stages of my research (see Fig..1). To model these biological systems, we have developed the SMOL package (http://mccammon.ucsd.edu/smol). The SMOL package mainly aims

to model the electrostatics and time-dependent diffusion in various biological systems using the finite element method. We have implemented it to solve the diffusion and reaction equations at the molecular level, as well as for the cholinergic synapse. Different from the QM/MM and classical MD simulations, the problem domain is discretized by Delaunay tessellation instead of atomic positions. The application of the adaptive finite element meshes can adjust the quality of the computation according the user's specific requirements.

In summary, Chapter I of this dissertation addresses my QM/MM and MD work for probing the enzymatic reaction mechanism in the protein kinase A and acetylcholinesterase, Chapter II considers the time-dependent Smoluchowski diffusion equation in the acetylcholinesterase monomer and tetramers, and Chapter III considers the time-dependent diffusion equation with chemically reactive boundaries in the cholinergic synapse.

I

Combined Quantum Mechanical and Molecular Mechanical Applications

I.A The cAMP-Dependent Protein Kinase: Phosphorylation Reaction Mechanism Studies

I.A.1 Abstract

We have carried out density functional theory QM/MM calculations on the catalytic subunit of cAMP-Dependent Protein Kinase (PKA). The QM/MM calculations indicate that the phosphorylation reaction catalyzed by PKA is mainly dissociative, and Asp166 serves as the catalytic base to accept the proton delivered by the substrate peptide. Among the key interactions in the active site, the Mg^{2+} ions, glycine rich loop, and Lys72 are found to stabilize the transition state through electrostatic interactions. On the other hand, Lys168, Asn171, Asp184, and the conserved waters bound to Mg^{2+} ions do not directly contribute to lower the energy barrier of the phosphorylation reaction, and possible roles for these residues are proposed. The QM/MM calculations with different QM/MM partition schemes or different initial structures yield consistent results. In addition, we have carried out 12 ns molecular dynamics simulations on both wild type and K168A mutated PKA respectively to demonstrate that the catalytic role of Lys168 is to keep ATP and substrate peptide in the near-attack reactive conformation.

I.A.2 Introduction

Protein phosphorylation, a common reversible covalent modification catalyzed by protein kinases, plays a critical role in cellular regulation and signal transduction. There are more than 500 protein kinase genes identified, representing about 1.7 percent of all human genes. In the large and very diverse family of protein kinases, the catalytic subunit (C-subunit) of cyclic AMP-dependent Protein Kinase (PKA) is the best characterized member, and often serves as a paradigm for the entire family [13]. This subunit has only about 350 residues and a bilobal structure. It catalyzes the transfer of γ-phosphate of ATP to specific serine or threonine residues of the substrate peptides. Experimentally, it was the first protein kinase to be discovered and purified [14], the first to be sequenced [15], and the first to be cloned and expressed in large quantities in *Escherichia coli* [16].

Extensive experimental studies have been reported, including mutagenesis [17, 18, 19, 20, 21, 22, 23], NMR solution studies, chemical footprints, catalytic trapping, rapid quench flow, mass spectrometry, fluorescence anisotropy [13, 24, 25, 26, 27, 21], and crystal structures of several complexes (including reactant and transition state mimics) [28, 29, 30, 31]. Much information has been provided. However, due to experimental challenges in defining the reaction mechanism, some detailed questions regarding how PKA catalyzes the phosphorylation reaction remain unsettled, including whether the reaction is associative or dissociative, and the respective catalytic roles of specific residues, metal ions and structural elements. There are particularly intriguing questions regarding the catalytic roles of Asp166, Lys168, the glycine rich loop, etc.

Asp166 is a residue conserved in the active site of all protein kinases and resides in a position likely to form hydrogen bonds with the substrate Ser [32, 31]. Mutation to Ala causes at least a 300-fold reduction of the V_{max} without greatly affecting the K_m's for either ATP or the substrate peptide [17]. It was first suggested to be the catalytic base, which accepts the proton from the substrate hydroxyl, and enhances the nucleophilic reactivity of the P-site serine. This suggestion is consistent with the early *pH* dependence studies [33], which indicate that there is a catalytic base existing in the active site. However, more recent kinetic studies in which the burst phase in PKA activity was monitored with rapid quench flow techniques have shown that the rate constant for this phase is independent of *pH* between *pH* 6 and 9 [34]. Meantime, considering the basicities of aspartate (pK_a of less than 5) and serine (pK_a of 14) in the aqueous solvent, it was suggested that Asp166 may not be an effective general base, and the catalytic roles for

Asp166 may be the substrate orientation or to accept the proton late in the reaction process [34]. Lys168 is another important residue in the PKA active site. It is conserved in all Ser/Thr kinases and replaced by an Arg in tyrosine kinases [35, 36]. It interacts with γ-phosphate in various crystal structures before and after phosphoryl transfer [31], and the replacement of Lys168 with Ala leads to a 50-fold reduction of the k_{cat}. Although Lys168 is recognized to be important, the respective catalytic role is not clear: whether stabilizing the transition state through electrostatic interaction, or directly participating in the reaction by transferring one of its protons to the phosphate group, or something else. The glycine-rich loop [KTLG^{50}TG^{52}SFG^{55}RV] in the small lobe is one of the most important motifs in the conserved protein kinase catalytic core. With ATP in the active site cleft, the glycine-rich loop takes on a "U" shape and covers ATP with stable hydrophobic interactions and hydrogen bonding (cf. Fig. I.1). The analysis of different PKA crystal structures shows that the conformation of this loop is quite related to the ATP loading and the release of ADP product [37]. Structural studies [28] suggest that the loop may play a role in stabilizing the transition state. However, Ala/Ser mutagenesis studies demonstrated that mutations to single glycines had little effect on the catalytic activity of PKA. The most severe effect on k_{cat} was no larger than 6-fold [22]. Other studies showed that the replacement of Ser53 with Thr, Gly or Pro didn't affect k_{cat} [23]. It seems that there are some inconsistencies between the suggestions from the structural studies and the results from the mutation studies.

Considering the significance of the phosphorylation reaction and the uncertainties of the experimental studies, computational study of the phosphoryl transfer reaction catalyzed by PKA should be helpful. In principle, computational studies can provide detailed information and insights to complement experimental studies. However, this goal can only be attained when appropriate computational approaches are employed and the system studied is a good mimic of the enzyme system. Early semi-empirical QM (AM1, PM3) or semi-empirical QM/MM calculations on the phosphorylation reaction catalyzed by kinase [3, 4, 5] suggested very high energy barriers, and a minimal role of Asp166. Their calculations suggest that the proton in the substrate hydroxyl directly transfers to γ-phosphate of ATP with or even without the aid of Asp166. The results are inconsistent with the experimental results. Furthermore, *ab initio* QM calculations and hybrid B3LYP/MM single point calculations by Sheppard et. al. [38] have shown that semi-empirical methods may not be adequate to study the phosphorylation reaction catalyzed by kinases. Recently, several density functional calculations [6, 39, 7, 8, 9, 10] on kinase model

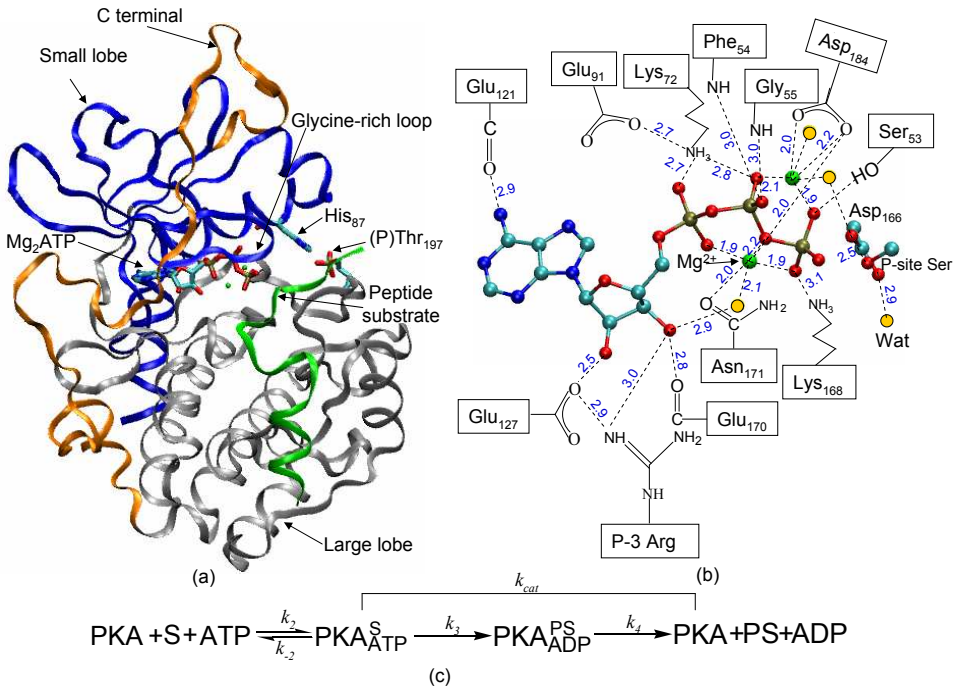

Figure I.1: The structure of the ternary PKA-substrate complex. (a) Ribbon representation of the catalytic subunit with the N-terminal (in purple), small-lobe core (in blue), large-lobe core (in tan) and the C-terminal (in orange), including Mg_2ATP (in licorice representation) and a 20-residue peptide substrate (in green) resulting from the initial MM geometry optimization. (b) The schematic representation of the active site. Residues displayed in ball-and-stick representation exhibit the exact conformation and relative orientation, including ATP ligand, side-chains of P-site Ser and Asp166, two Mg ions (in green) and three conserved waters (in yellow). (c) The overall phosphoryl-transfer reaction scheme. k_3 is the rate constant of the phosphoryl-transfer step and k_4 is the rate constant of the product-release step. k_{cat} is the first-order rate constant for the overall phosphoryl transfer and product release.

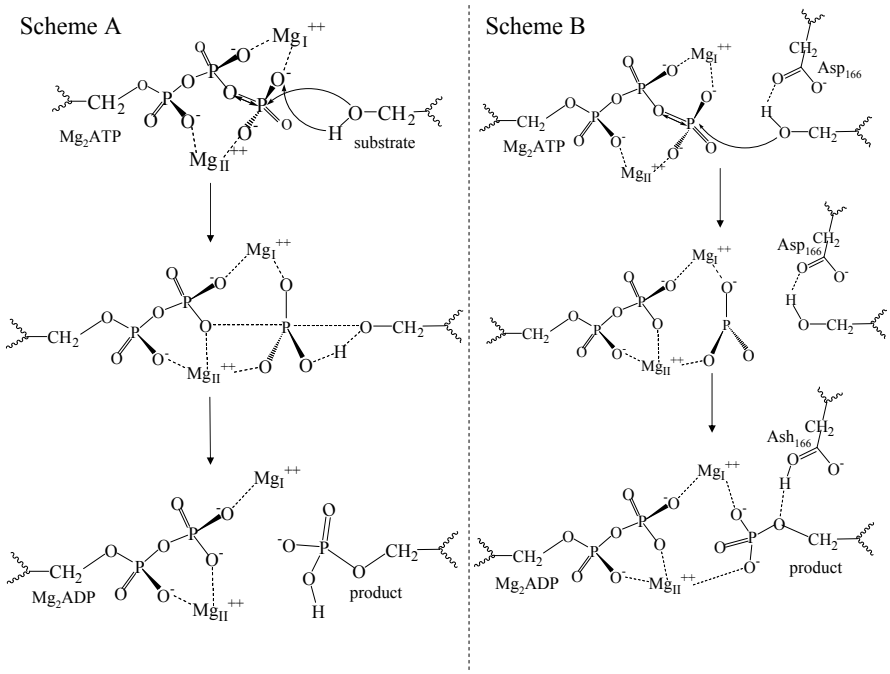

Figure I.2: Two phosphoryl transfer schemes provided by previous theoretical calculations. Scheme A is the concerted phosphoryl and proton transfer model suggested by previous semiemprical calculations and some DFT calculations [3, 4, 5, 6, 7]; scheme B described a dissociative phosphoryl transfer and the shift of the proton to Asp166, which suggested by the most recent DFT calculations [8, 9, 10].

complexes have been carried out to study the phosphorylation reaction. In such model complex studies, the size of the system is limited, the enzyme environment can not be simulated and the calculation results are often quite dependent on the choice of model complexes. For example, the calculation results by Hirano et al. [6] and Cavalli et al. [7] yielded the reaction scheme (A) as shown in Fig. I.2 and obtained a high reaction barrier of $36 \sim 42$ kcal/mol, while Valiev et al. [8] and Diaz et al. [9] obtained a dissociative reaction pathway (scheme B in Fig. I.2) with reaction barriers between 10 and 20 kcal/mol. Very recently, Henkelman et al. provided further evidences that the reaction barrier is quite dependent on the model size and initial crystal structures [10].

In this work, we have performed computational studies on the phosphoryl transfer catalyzed by PKA using combined *ab initio* quantum mechanical and molecular mechanical

(QM/MM) methods. In the study, the whole enzyme complex is simulated. The active site, which participates in making and breaking bonds, is treated by *ab initio* quantum mechanical methods, while the rest of the enzyme is described by molecular mechanical methods. Calculations with different QM/MM partition schemes and different initial structures yield consistent results, which indicate that the phosphorylation reaction catalyzed by PKA is mainly dissociative and that Asp166 serves as the catalytic base to accept the proton delivered by the substrate peptide. Furthermore, we have elucidated the respective catalytic roles of the key interactions throughout the PKA enzyme through reaction barrier decomposition analysis and long molecular dynamics simulations on wild type as well as mutated PKA complexes. The catalytic role of Lys168 is demonstrated to keep ATP and substrate peptide in the near-attack reactive conformation [40].

I.A.3 Computational Methods

In the current study, we employed the pseudobond *ab initio* QM/MM approach [41, 42, 43], which has been demonstrated to be effective in the study of several enzymes, including enolase [44], acetylcholinesterase [45, 46] and 4-oxalocrotonate tautomerase [47, 48]. Throughout the study, the charged phosphate groups were included in the QM subsystem and were calculated at B3LYP/6-31G* level. This level of calculation is similar to that used in other contemporary studies [8, 9].

Preparation of the Enzyme-Substrate System

The initial structure was chosen from two PKA-ligand complexes (PDB code: 1L3R and 1ATP). The 1L3R structure is that of PKA in complex with ADP, AlF_3, Mg^{2+}, while the 1ATP structure is that of a ground state analog in which the thermally stable inhibitor PKI instead of the substrate peptide (SP20) is included. For the 1L3R structure, we mutated AlF_3 back to γ-phosphate using Insight II. For the 1ATP structure, we phosphorylated Ser139, replaced two Mn^{2+} with Mg^{2+} ions, and mutated the P-1 and P site residues of PKI to change it into the substrate peptide (SP20). For both 1L3R and 1ATP models, hydrogens for heavy atoms were added by Leap in the Amber 7.0 package [49], while hydrogens for crystal conserved waters were added and optimized by WHATIF [50]. For histidine residues, calculations of the local electrostatic microenvironment and the effective pK_a with WHATIF indicated that His87 should

doubly be protonated on both N_η and N_δ, while the others are neutral residues: HID62, HID68, HID260 with N_δ protonated; HIE131, HIE142, HIE158, HIE294 with N_η protonated. Whether HID/HIE is chosen is determined by the local hydrogen bonding network. Since the charge parameters of Mg_2ATP, phosphorylated serine and threonine are not available in the Amber force field, we have determined them using QM calculation and the RESP module in the Amber 7.0 package. All other force field parameters are from the parm99 parameter set [51] and the polyphosphate parameters developed by Meagher et al.[52].

After relaxing the added atoms using the Amber 7.0 package in the gas phase, each structure was immersed in a cubic TIP3P water box (90*90*90 $Å^3$) and neutralized by addition of Cl^- counter-ions using the Amber Leap module. This led to a 1L3R simulation system of 40,332 atoms and a 1ATP simulation system of 37,117 atoms, respectively. Molecular dynamics simulation with periodic boundary conditions was conducted. A default cutoff radius of 8 $Å$ was introduced for nonbonding interactions, updating the neighbor pair list every 10 steps. The electrostatic interactions were calculated with the Particle Mesh Ewald method [53]. The SHAKE algorithm [54] was used to constrain all bond lengths involving hydrogens. Optimization and 50 *ps* relaxation of solvent and ions were performed at first under constant volume conditions, keeping all the heavy atoms constrained to their initial positions with a force constant of 50 kcal/mol·$Å^2$, then under constant pressure and the same constraint, the whole complex was relaxed for 60 *ps*. The systems were then energy refined with 50, 20 kcal/mol·$Å^2$ constraints, respectively. The QM/MM model was obtained by deleting the water more than 27.0 $Å$ away from the β-phosphorus of ATP. The total atom numbers in our QM/MM models are 8610 in 1L3R and 9652 in 1ATP. At the same time, free MD simulations of both 1L3R and 1ATP were continued to obtain 12 ns trajectories.

QM/MM calculations

The enzyme-substrate models 1L3R and 1ATP prepared as described above were each partitioned into a QM subsystem and a MM subsystem. We have employed two partition schemes, with the sole difference in whether to cut the ATP molecule. In the small QM subsystem partition scheme, the QM subsystem comprises the triphosphate arm of ATP, side chains of P-site Ser, Asp166, and Lys168, and two Mg^{2+} ions with 49 atoms. The large QM subsystem consists of the whole ATP molecule, side chains of P-site Ser, Asp166, Lys168, and two Mg^{2+}

ions for a total of 75 atoms. The boundary between the QM and MM subsystems was treated using the pseudobond approach [41]. The total energy of the QM/MM system is :

$$E_{Total} = E_{MM} + E_{QM} + E_{QM/MM} \tag{I.1}$$

The QM/MM interactions consist of bonding and nonbonding interactions. The nonbonding interactions between two subsystems include the vdW part through the Lennard-Jones potential and the electrostatic part calculated through a coulombic term in an effective Hamiltonian. The energy of the effective Hamiltonian, which is obtained by QM calculations, is the sum of the QM energy of the QM subsystem (E_{QM}) and the electrostatic interaction between QM and MM subsystems [41].

With each prepared QM/MM system an iterative optimization procedure [42] was applied to the system with B3LYP(6-31G*) QM/MM calculations, leading to an optimized structure for the reactant. We then employed the reaction coordinate driving method [55, 42] to search for the transition state and product. By experimenting with several possible reaction coordinates, the following reaction coordinate turns out to be most appropriate for this phosphorylation reaction: $RC = d_1 + d_3 - d_2 - d_4$, where the definitions of d_1, d_2, d_3 and d_4 are described in Fig.I.3. An iterative restrained minimization was then repeatedly applied to different points along the reaction coordinate, resulting in a minimum energy path for the reaction in the enzymatic environment and its associated potential energy surface. Given that the determined minimum energy path is smooth and continuous, Hessian matrices for degrees of freedom involving atoms in the QM subsystem were calculated at stationary points, leading to determination of the corresponding vibrational frequencies [43]. The energy maximum on the path with one and only one imaginary frequency is the transition state, while the energy minima along the path with no imaginary frequencies are characterized as the reactant or the intermediate. For the reactant, transition state, and tetrahedral intermediate, we further carried out single-point higher level (MP2 and B3LYP) QM/MM calculations with a larger 6-31+G* basis set.

Other Computational Details

Geometry optimizations for all the above QM subgroups were at the B3LYP(6-31G*) level, with the interactions from the MM subgroup treated by the QM/MM method. The subsequent single-point calculations at the 6-31+G* level with B3LYP and MP2 were performed on

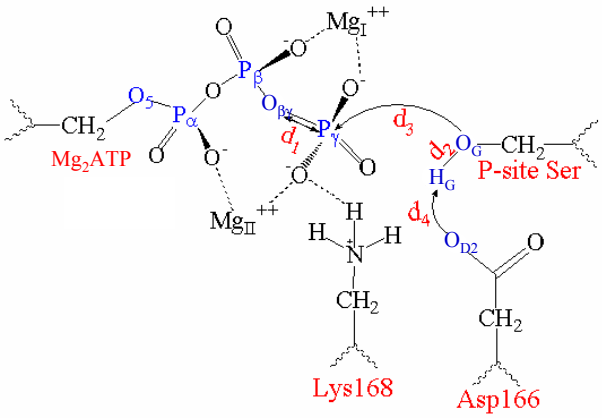

Figure I.3: The 49-atom QM subgroup in our QM/MM calculations (the small QM/MM model).

the geometries optimized at the B3LYP(6-31G*) level. Throughout the QM/MM calculations, pseudobonds were treated with the 3-21G basis set and its corresponding effective core potential parameters. The calculations were carried out using modified versions of the Gaussian98 and TINKER programs [56]. For the QM subsystem, criteria used for geometry optimizations follow Gaussian98 defaults. For the MM subsystem, the convergence criterion used is to have the root mean square (RMS) energy gradient be less than 0.1 $kcal \cdot mol^{-1}\AA^{-1}$. In the MM minimizations, only atoms within 20 $\AA$ of the β phosphorus of ATP were allowed to move. No cutoff for nonbonding interactions was used in the QM/MM calculations and the MM minimizations.

I.A.4 Results and Discussions

For the phosphoryl-transfer reaction step, the calculated potential energy results are listed in Table I.1, and the reaction energy profiles and the corresponding geometries for the reactant, transition state and the intermediate are shown in Fig. I.4. The calculated minimum-energy paths are shown in the Fig. I.5. Despite the choices of the different initial structures (1L3R vs. 1ATP) and the different QM/MM partition schemes, the calculations provide a consistent picture. Our results do not support the mechanism proposed from previous semi-empirical QM studies [4, 3, 5]. We found that the phosphorylation reaction proceeds through a mainly dissociative transition state, and Asp166 serves as the catalytic base to accept the late proton transfer, which is consistent with the reaction scheme (B) [8, 9] as shown in Fig. I.2. The calculated potential energy barriers at the B3LYP(6-31+G*) QM/MM level are 11.6, 14.3 and 10.0 kcal/mol for 1L3R (small QM subsystem), 1ATP (small QM subsystem) and 1L3R (large QM subsystem) respectively. The value of the barriers is quite consistent with the experimental measurement of about 500 sec^{-1} for the phosphoryl-transfer step (i.e. k_3, cf. Fig. I.1(c))[1] [21].

To test whether reaction scheme (A) is possible, in which the proton of the P-site serine transfers to the oxygen of the phosphate, we also conducted the corresponding B3LYP(6-31G*) QM/MM calculation using the 1L3R small model and found that the energy barrier is over 20 kcal/mol for reaction scheme (A) in comparison with 11.6 kcal/mol for the reaction scheme (B).

[1] According to the enzymatic reaction rate theory, the relation between the phenomenoloical reaction barrier and the rate constant can be written as

$$k(T) = (k_B T/h)(c^0)^{1-n} exp[-\Delta G^0_{act}(T)/RT] \tag{I.2}$$

For ours case, the approximate reaction barrier is around 13.8 kcal/mol.

Table I.1: The calculated total QM/MM potential energy difference (kcal/mol) for three QM/MM models. The geometries are calculated at the B3LYP(6-31G*)/MM level.

	MP2(6-31+G*)/MM	B3LYP(6-31+G*)/MM	B3LYP(6-31G*)/MM
		1L3R small model	
Reactant	0.0	0.00	0.00
Transition State	9.1	11.6	10.9
Intermediate	6.6	9.5	7.8
		1ATP small model	
Reactant	0.0	0.0	0.0
Transition State	11.6	14.3	12.3
Intermediate	10.1	12.6	10.4
		1L3R large model	
Reactant	0.0	0.0	0.0
Transition State	7.7	10.0	9.5
Intermediate	4.3	7.4	6.3

So our calculations do not support reaction scheme (A) in Fig. I.2 [4, 3, 5, 6, 7]. Our reaction barriers are quite close to the recent DFT calculations on the active site of PKA. For example, Valiev et al. proposed 11.0 kcal/mol reaction barrier while 16.5 kcal/mol by Diaz et al. [8, 9].

From the calculated geometry for the transition state, we can see that the phosphoryl transfer in PKA is mainly dissociative. Both of the QM/MM calculations for 1L3R showed symmetric transition states and about 80% dissociative character using Pauling's formula as suggested by Mildvan [57]. The PO_3 plane is almost in the middle of the entering and leaving oxygens, and the distances between the phosphorus and the entering and leaving oxygens are 2.1 $\AA$ and 2.3$\AA$, respectively. For the 1ATP small QM model, a similar trigonal bipyramidal coordination for the transition state was obtained. PO_3 is in a planar geometry, too. The distances between the phosphorus and the donor and recipient oxygens are 2.5 $\AA$ and 2.0 $\AA$, respectively. Overall, the active site geometries of our transition states are quite similar to the above two DFT calculations [8, 9].

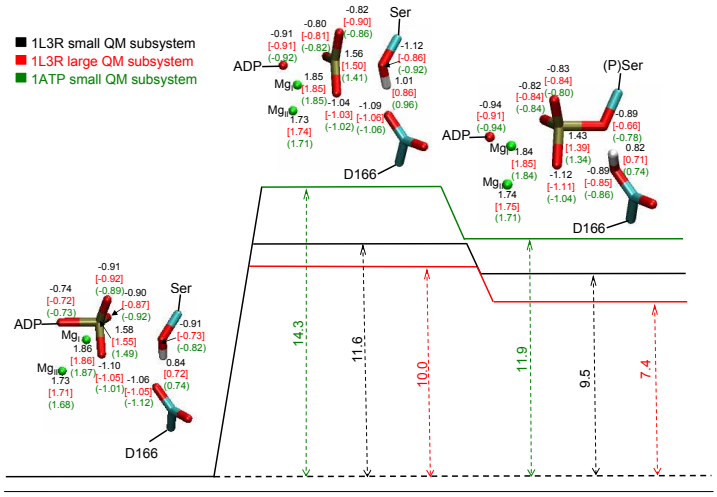

Figure I.4: Calculated reaction scheme for the phosphoryl transfer step of 1L3R and 1ATP models. The values on the atoms indicate B3LYP/6-31+G* ESP charges for molecules in the QM subgroup (in a.u.); the unit of the height of the barrier is kcal/mol.

The role of Asp166

Asp166 was confirmed to be the catalytic base again in our calculations. Despite the choice of the different initial crystal structures and different partitions, the calculated distances show that the substrate Ser still keeps its hydroxyl proton at the transition state, which confirms the late proton transfer result by Valiev et al. [8] and is also consistent with recent experimental results [58, 59, 60, 61, 62, 28, 63, 64].

To test the hypothesis that Asp166 also acts as a structural anchor to maintain the configuration of the active site, we have mutated Asp166 to Ala at the beginning of setting up the wild type 1L3R model, then performed 12 ns classical MD simulation using the Amber99 force field for this mutated PKA with the same procedure for the wild type 1L3R. By analyzing the MD trajectories, we did not find a significant change in the configuration of the active site between two simulations, cf. Fig. I.6. The average distance between γ-phosphorus and the hydroxyl oxygen of substrate Ser is 3.36±0.21 *Å* for the mutated PKA, and 3.72±0.42 *Å* in the wild type 1L3R model. The mean-square fluctuations of the positions of the ATP atoms are also similar in the two simulations. Such an observation is quite consistent with only a small, 3-fold increase in K_m(pep) and similar K_m(ATP) in D166A mutation experiments [17]. So our QM/MM

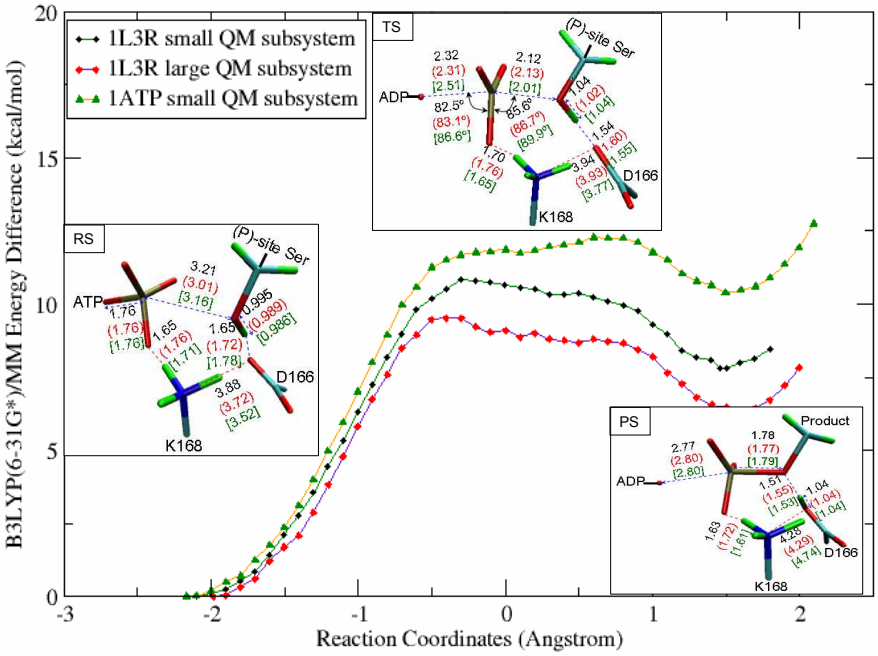

Figure I.5: The determined minimum energy paths for the small and large QM/MM models of 1L3R. Distances between atoms involved in bond breaking and forming are given in *Å*.

and MD simulation results indicate that the role of Asp166 is as the catalytic base, rather than a structural anchor to maintain the configuration.

The role of Lys168

Besides Asp166, Lys168 is another important residue in the PKA active site. It is conserved in all Ser/Thr kinases and replaced by an Arg in the tyrosine kinases [35, 36]. It interacts with the γ-phosphate in various crystals before and after phosphoryl transfer [31], and the replacement of Lys168 with Ala leads to large increases of K_m. There have been mainly two possible catalytic roles for this residue proposed in the literature: one is that it directly participates in the reaction by late transfer of one of its protons to the phosphate group, and the other is that it stabilizes the transition state through electrostatic interaction. We have conducted calculations to examine both hypotheses.

First we have conducted B3LYP(6-31G*) QM/MM calculations on the 1L3R small model to study whether the proton transfer step between Lys168 and the phosphate group could take place. The results indicate that the transfer of a proton from Lys168 to the phosphate group is uphill and the resulting product is destabilized by 3.3 kcal/mol. So our calculations do not support that Lys168 directly participates in the reaction. Then we conducted the calculations to test whether the role of Lys168 is to stabilize the transition state. Here one difficulty is that we have included Lys168 in the QM subsystem which makes it difficult to analyze its interaction with the rest of the active site. So we have conducted B3LYP(6-31G*) QM/MM calculations on the 1L3R model and 1ATP model with a even smaller QM/MM partition in which Lys168 is treated molecular mechanically, and we determined the reactant and transition states using the same procedure. We then analyzed the interaction between the Lys168 and the QM sub-system to determine its contribution to the stability of the transition state. Surprisingly, we found that the electrostatic interaction between Lys168 and the QM subsystem strongly destabilizes the transition state.

Our calculations so far do not support either of the hypotheses. So what is the catalytic role of Lys168? Here we mutated Lys168 with Ala in our 1L3R model, and performed a 12 ns classical MD simulation on the K168A mutant with the same procedure as the wild type model. By analyzing the two trajectories and comparing their results, we found that although the K168A mutant has a very similar RMSD to that of the wild type, the distance between P_γ of ATP and the hydroxyl oxygen of the P-site Ser is significantly (on average 2.9 $\AA$) longer in the K168A model

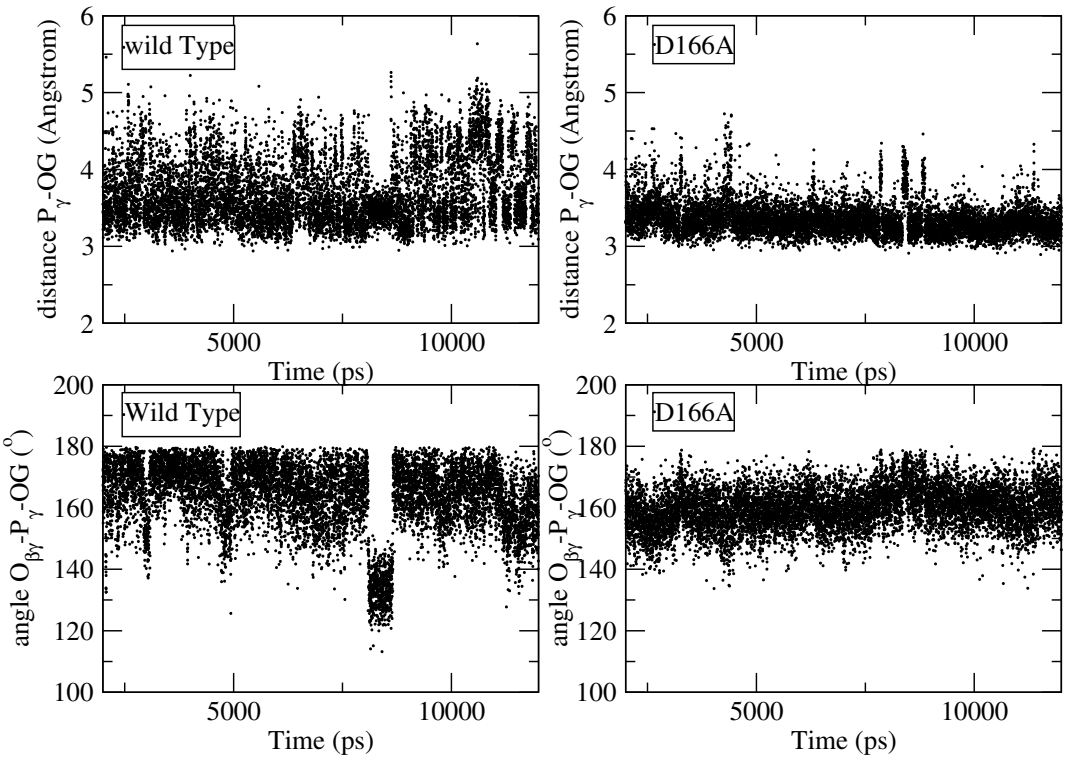

Figure I.6: The distances between P_γ and the OG atom in the wild type and D166A mutation; the ATP-substrate alignment angle $O_{\beta\gamma} - P_\gamma - OG$ in the wild type and D166A mutant.

than in the wild type, as shown in Fig. I.7. Moreover, The atomic mean-square fluctuations of Mg_2ATP in the K168A mutant is 0.18 $\AA^2$ compared to 0.14 $\AA^2$ in the wild type 1L3R. So our MD simulations indicate that the main catalytic role of Lys168 is to keep ATP and the substrate peptide in the near-attack reactive conformation. The larger distance between the ATP and the substrate peptide also indicates weaker binding of the peptide substrate, which is consistent with the mutagenesis result of increased K_m in yeast C-subunits [17].

Catalytic roles of individual MM residues interacting with the active site

To understand the role of each residue in catalysis, we performed vdW and electrostatic energy contribution calculations between the QM sub-system and individual MM residues as the phosphorylation reaction proceeds from the reactant to the transition state based on the geometries of the small B3LYP(6-31G*) QM/MM models of 1L3R and 1ATP, respectively. While the results of the energy decomposition are suggestive, it must be recognized that the details would vary somewhat with the use of different models for the quantum mechanical or molecular mechanical calculations. Such analyses have been demonstrated to be able to provide detailed insights into enzyme catalysis [44, 45, 47], among which some computational hypotheses [44, 47] have been confirmed by later experimental studies [65, 47]. The charges of the transition states (TS) and the reactant states (RS) were determined with B3LYP(6-31+G*)/MM calculation (MP2(6-31+G*)/MM calculation gives very similar results). The electrostatic and vdW interaction energies between the given residue and the QM sub-group were calculated classically for the reactant and transition state, respectively. The difference between the corresponding RS and TS results indicates the contribution of each residue to the reaction barrier. A negative number indicates that the residue stabilizes the TS, and vice versa. Since the effects of conformational change and dielectric screening are absent in our analysis, and the original *ab initio* QM/MM calculations were performed variationally, we only use these numbers as a qualitative indicator, and not as a quantitative prediction. The vdW interaction change is generally quite small, therefore the results shown in Fig.I.8 only include the electrostatic interactions. We can see that the results for the two kinase structures are consistent with one another.

The glycine-rich loop is one of the most important motifs in the conserved protein kinase catalytic core. As discussed in the introduction, it seems that there is some inconsistency between the suggestions from the structural studies [28] and the results from the mutation studies [22, 23]: structural studies suggest that the loop may play an important role in stabilizing the

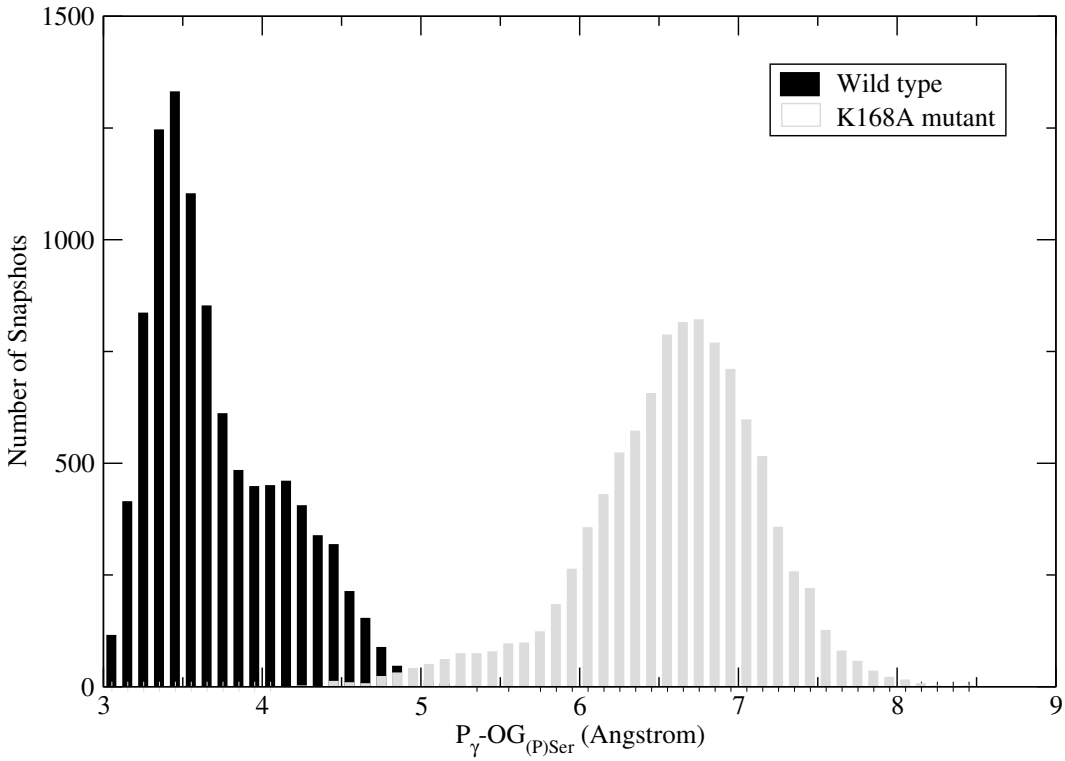

Figure I.7: Time-dependent variation of separation of P_γ in ATP and the hydroxyl oxygen OG in P-site Ser. For the definition of OG and P_γ (see Fig. I.3).

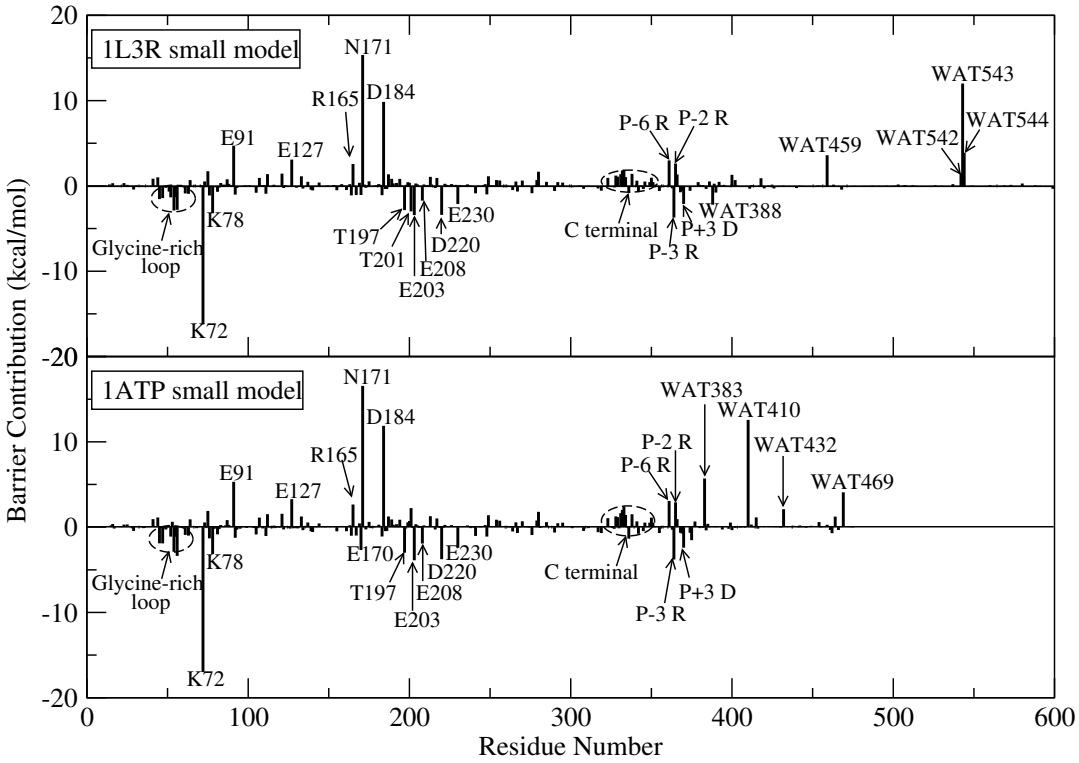

Figure I.8: The individual MM residue electrostatic contribution to the transition state stabilization and destabilization.

transition state while mutagenesis studies indicated that mutation of a single glycine has modest effects on the catalytic activity of PKA. Our calculation results for this structural unit are shown in Table I.2. We can see that despite the modest contributions of the individual residues in the loop to the barrier according to Fig.I.8, almost every residue in the whole loop (except Ser53) contributes to stabilize the transition state to some degree. The total contributions to stabilize the reaction barrier are 7.4 and 8.8 kcal/mol in 1L3R and 1ATP models respectively. Thus, our calculation results indicate that the catalytic role of the glycine-rich loop comes from the collective effect rather than a single residue, and there is actually no inconsistency between the suggestions from the structural studies [28] and the results from the mutation studies [22, 23].

Table I.2: Glycine-rich loop individual residue contributions to the transition state stabilization or destabilization for two crystal structures (calculation based on B3LYP(6-31+G*)/MM calculations) $E_{ele+vdw}$ refers to the total nonbonding interaction energy including electrostatic and vdW parts. "MM Total" refers to the interaction between the total glycine-rich loop and QM subgroups. Energy units are in kcal/mol.

	$E_{ele+vdw}$	
Residue	1L3R	1ATP
Lys47	-1.1	-2.0
Thr48	-0.1	-0.2
Leu49	-0.2	-0.3
Gly50	0.1	-0.1
Thr51	-0.8	-0.1
Gly52	-0.2	0.3
Ser53	0.6	1.1
Phe54	-2.2	-2.8
Gly55	-1.3	-1.3
Arg56	-2.2	-3.5
Val57	-0.0	-0.0
MM Total	-7.4	-8.8

Residue Lys72 and Glu91 are another two conserved charged residues in the small

lobe. Structural studies [31] have shown that Lys72 anchors α- and β-phosphate and Glu91 bridges to Lys72, cf. Fig. I.1(b). The results in Fig. I.8 show that Lys72 strongly stabilizes the transition state through electrostatic interactions, while the Glu91 does not. Here we propose that the main role of Glu91 is to position the Lys72. Our finding that Lys72 strongly stabilizes the transition state is consistent with mutation studies [17] showing that replacement of Lys72 with Ala led to an 800-fold decrease in V_{max} with only a 5-fold increase in K_m(ATP). [17].

Lys78 is another transition-state stabilizer which contributes around 2∼2.5 kcal/mol. This residue lies in the C helix and has the potential to form hydrogen bonds with the carbonyl oxygens of Phe54 and Ser53 (d_{NZ-O} = 4.31 $\AA$ and 3.81 $\AA$ in 1L3R crystal) in the glycine-rich loop. The 12 ns MD simulation of the wild type 1L3R enzyme captured around 1% H-bonding between them. Glu127 lies in the ATP pocket, forming a hydrogen bond with the hydroxyl in the ribose of ATP. Our analysis indicates that it destabilizes the transition state. Experimental replacement with Alanine decreases the reactivity of PKA to 2.3% of the wild type [17]. So we propose that the main role of Glu127 is likely to bind ATP in the right reactive conformation.

Although Arg165 destabilizes the transition state, it lies in the catalytic loop, and forms two stable H-bonds with (P)Thr197. Experimental replacement of Arg165 with Alanine decreases the reactivity of the kinase to 10.5% of the wild type [17]. Fig. I.9 shows that Arg165 has double hydrogen bonds with (P)Thr197 and directly links with Asp166, the catalytic base. The displacement of Arg165 essentially affects the hydrogen bonding network among ATP, P-site serine and Asp166. Arg165 functions as the bridge to communicate between the activation loop and the active site. Asp220, anchoring the backbones of Arg165 and Tyr164 via hydrogen bonds, helps to hold the Arg165-Asp166 chain in the proper conformation and stabilizes the transition-state.

Asn171 and Asp184 strongly destabilize the transition-state, and contribute over 10 kcal/mol to the transition-state individually. Structurally, both of them bind to Mg^{2+} ions. We believe that these two residues are essential for binding Mg^{2+} ions , which provide stabilization to the transition-state (discussed later). The fact that replacement of Asp184 with Alanine made the PKA inviable emphasized such a role [17]. In addition, three active-site conserved waters, Asn171 and Asp184, all of which bond with the two conserved magnesium ions, extensively destabilize the transition state.

All the residues between Asp184 and Glu280 that interact with the QM subgroup by

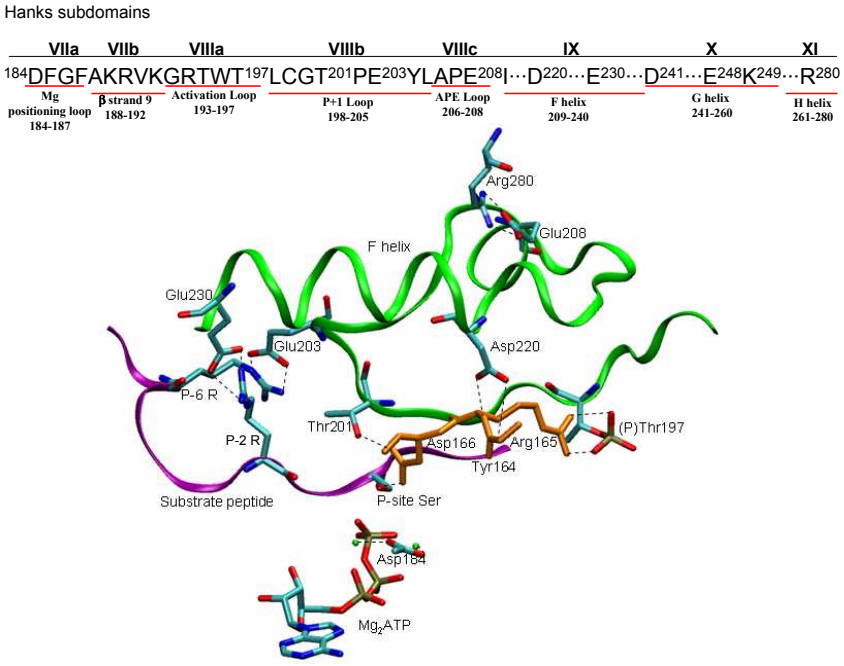

Figure I.9: The individual nonbonding interactions between the residues 184-280 and the QM subgroup.

more than 0.8 kcal/mol have been listed in Table I.3 and shown in Fig. I.9. (P)Thr197 contributes stabilization to the transition state, as do Glu203 and Glu230 by hydrogen bonding with the substrate peptide. Thr201 forms a hydrogen bond with Asp166 and contributes to stabilize the transition-state in the 1L3R model, but somehow destabilizes in the 1ATP model. The role of this conserved residue is still not clear. Experimental replacement with Ala impaired the ability to autophosphorylate Thr197, and abolished activity because of steric factors [66, 67]. In our calculation models, Lys168 bridged the phosphate to the peptide via an -OH of Thr201. To sum up, the overall catalytic effect for the residues between Asp184 and Glu280 is to stabilize the transition state more than 12 kcal/mol. Another conserved water, WAT459 in 1L3R (WAT383 in 1ATP), forming a bridge between the OD1 of Asp166 and the carbonyl oxygen of Leu167, destabilizes the transition state by 3.6 kcal/mol in 1L3R and 5.7 kcal/mol in 1ATP. So the role of this water is apparently structural.

Several charged residues in the substrate peptide affect the stabilization of the transition-state, too. P-6 and P-2 Arg destabilize the transition-state, while P-3 Arg and P+3 Asp always stabilize the transition state. To sum up, the net effect is that the transition state is stabilized slightly, i.e. -0.6 kcal/mol in 1L3R and -1.1 kcal/mol in 1ATP.

The role of the two Mg^{2+} ions

In PKA studies, Mg_I (binding with β- and γ-phosphates) is generally identified as a catalytic activator, while Mg_{II} (binding with α- and γ-phosphates) as an inhibitor. A more thermostable conformation, secured by two metal sites being occupied, appears to switch with a catalytically more active but less thermostable conformation with one metal site occupied [69, 70]. In our calculations, although the two magnesium ions are treated quantum mechanically, the charges on the magnesium ions change very little from the reactant to the transition state, and to the product. So we have calculated the classical electrostatic interaction energies between the magnesium ion and the rest of the QM sub-system without magnesium ions, as shown in Table I.4. We can see that both metal ions contribute greatly to lower the transition state barrier through electrostatic interactions. Mg_{II} contributes even more stabilization to TS than Mg_I, which seems to be inconsistent with the experimental results [69, 70]. Here we make the following two hypotheses. First, the role of the two magnesium ions is to activate the phosphoryl transfer, while residues like Asn171 and Asp184 and several active-site conserved waters binding with them destabilize TS and play an ”inhibitory” role. When only one magnesium ion is bound,

those anchoring residues will also be positioned differently and may have less inhibitory effect on the reaction. The second reason is that the rate determining step is the dissociation of the product, so that the enzyme with one magnesium ion bound, which is less thermostable, may have larger conformational fluctuations to facilitate the product release.

I.A.5 Conclusions

The phosphoryl transfer reaction catalyzed by the catalytic subunit of cAMP-Dependent Protein Kinase has been studied by density functional theory QM/MM calculations. Using different initial structures, the calculated reaction barrier at the B3LYP QM/MM level is 11.6 kcal/mol for an initial structure coming from a crystal mimic of the transition state, while 14.3 kcal/mol for an initial structure coming from a reactant complex mimic, which are very consistent with the experimental estimation of 13.8 kcal/mol.

Our calculations confirm that the phosphorylation reaction proceeds through a symmetric transition state, and then Asp166 serves as the catalytic base to accept the proton delivered by the substrate peptide. Although Lys168 strongly destabilizes the transition state in the phosphoryl-transfer step and does not directly participate in the reaction, our 12 ns molecular dynamics simulations on both wild type and K168A mutant respectively demonstrate that the catalytic role of Lys168 is to keep ATP and substrate peptide in the near-attack reactive conformation.

Barrier decomposition analysis qualitatively explained individual residue contributions in the whole enzyme. The glycine-rich loop, providing both hydrophobic and electrostatic interactions with ATP or ADP, always stabilizes the transition state. Lys72, binding with non-transferable phosphates of ATP, strongly stabilizes the transition state, while Lys168, Arg171 and Asp184 strongly destabilize the transition state. Although most of residues in the large domain are not located in the active site, the overall effect is to stabilize the transition-state. The role of Mg^2 ions appears to stabilize the transition state through electrostatic interactions, although the residues as well as water molecules binding to Mg^2 ions mainly play a structural role and destabilize the transition-state.

I.A.6 Acknowledgments

This work has been supported in part by grants from the NSF and NIH. Additional support has been provided by NBCR, CTBP, HHMI, the W. M. Keck Foundation, and Accelrys, Inc.

I.B The cAMP-Dependent Protein Kinase: How does Activation Loop Phosphorylation Modulate Catalytic Activity?

I.B.1 Abstract

Phosphorylation mediates the function of many proteins and enzymes. In the catalytic subunit of cAMP-dependent protein kinase, phosphorylation of Thr-197 in the activation loop strongly influences its catalytic activity. In order to provide theoretical understanding about this important regulatory process, classical molecular dynamics simulations and *ab initio* QM/MM calculations have been carried out on the wild type PKA-Mg_2ATP-substrate complex and its dephosphorylated mutant T197A. It was found that pThr-197 not only facilitates the phosphoryl transfer reaction by stabilizing the transition state through electrostatic interactions, but also strongly affects its essential protein dynamics as well as the active site conformation.

I.B.2 Introduction

Protein phosphorylation controls a myriad of key biological processes in cellular pathways, ranging from metabolic pathways to cell cycle control and gene transcription [71]. The abnormal phosphorylation of cellular proteins has been associated with many human diseases [72, 73]. Protein kinases, which catalyze the phosphoryl transfer reaction, are themselves regulated by phosphorylation. Due to its central importance, there is intense interest in understanding how phosphorylation modulates protein kinase activity [13, 74, 75, 76].

Among protein kinases, cAMP-dependent protein kinase (PKA) is the best characterized member, and often serves as a paradigm for the entire family [13]. Its catalytic subunit has only about 350 residues and forms a conserved bilobal structure [77, 78, 79], as shown in Fig. I.10. Its conserved core consists of two lobes: a small lobe (residues 40-120) dominated by β-sheets and a large lobe (residues 128-300) composed mostly of α helices. Most of highly conserved active site residues and residues involved in peptide binding are contributed by the large lobe. Mg_2ATP is bound in a deep cleft between the two lobes with the adenosine portion deeply buried in a hydrophobic pocket.

In PKA, Thr-197 in the activation loop is always auto-phosphorylated for full activity. In a variety of crystal structures, it is $8 \sim 10$ $\AA$ away from the catalytic site and forms several key contacts with charged residues from the large and small lobes [13]. The interaction with His-87

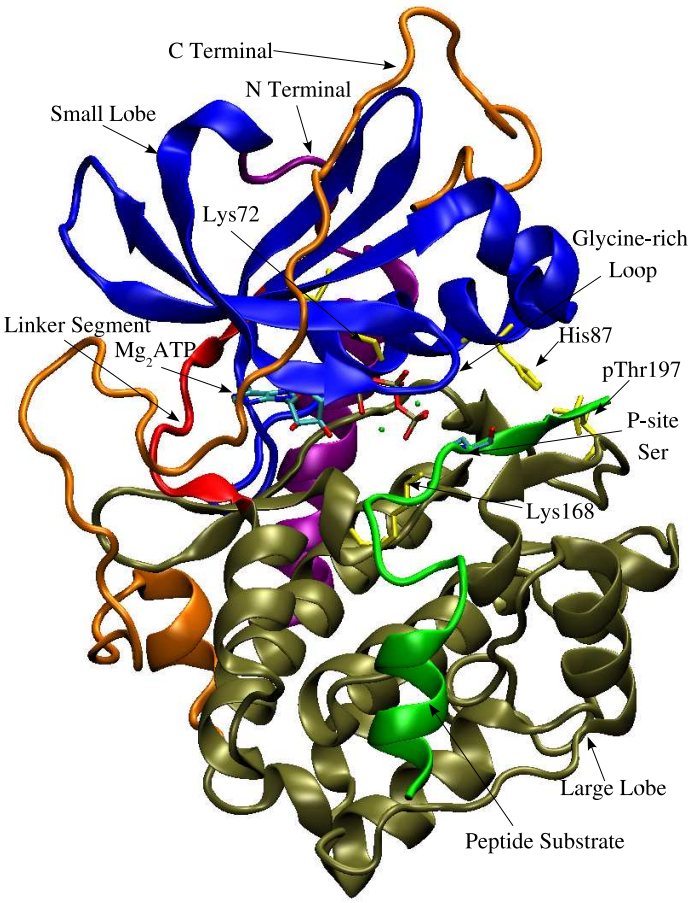

Figure I.10: The structure of the ternary PKA-substrate complex. Ribbon representation of the catalytic subunit with the N-terminal (in purple), small-lobe core (in blue), the linker segment (in red), large-lobe core (in tan) and the C-terminal (in orange), including Mg_2ATP (in licorice representation) and a 20-residue peptide substrate (in green) resulting from the original PDB.

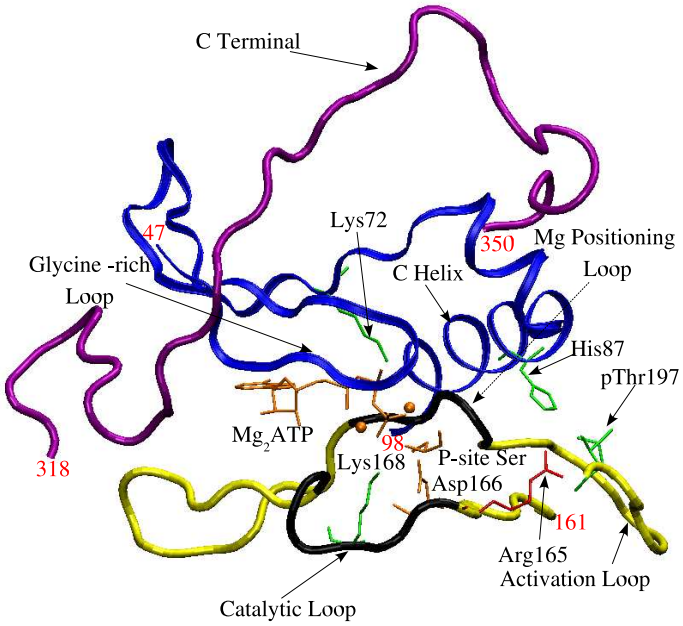

Figure I.11: Schematic depiction of the active site cleft. Residues 47−98 in the small lobe are blue displayed in ribbon representation, the linker and the region of β sheet in the large lobe (residues 161−197) are shown in yellow, with the catalytic loop (residues 166-171) and the Mg^{2+} positioning loop (residues 184−187) highlighted in black. The position of the carboxyl terminal tail that comes close to the activation site cleft, residues 318-350, is shown in purple.

in the small lobe is proposed to contribute to the closure of the catalytic site [75]. pThr-197 also forms a hydrogen bond with the catalytic loop residue Arg-165, which makes contact with Asp-166, the catalytic base in the catalytic site (fig. I.11) [8, 9, 80]. The removal of the activation loop phosphorylation site by T197A mutation reduces the phosphoryl transfer rate from over 500 sec^{-1} to 3.6 sec^{-1}, while it increases the K_m for ATP by two orders of magnitude [19, 21].

Although experimental studies have revealed the importance of this activation loop phosphorylation, its regulatory mechanism is still elusive [29, 81, 82, 24, 75, 76]. Several mechanisms have been proposed, including control of the active conformation [76], modulation of the phosphoryl transfer step [75], or formation of a P+1 substrate binding site at the C-terminal end

of the activation segment [81, 82, 24].

In our previous QM/MM investigations [80], we have studied the phosphoryl transfer reaction catalyzed by the wild-type PKA, and probed catalytic roles of individual residue contribution in enzyme catalysis. Based on barrier decomposition analysis, pThr-197 was found to contribute $\sim$2 kcal/mol to the electrostatic stabilization of the mainly dissociative transition state during the phosphoryl transfer reaction (see Fig. 8 in Ref. [80]), which is qualitatively in agreement with experimental studies[75]. However, since the method of barrier decomposition analysis assumes that the mutation of individual residue does not change the enzyme structure, such an analysis is very preliminary considering that the conformation change has been proposed as one possible mechanism for the activation loop phosphorylation [76]. Many questions remain unanswered, including: Does the auto-phosphorylation affect overall enzyme dynamics, or influence the active site conformation, or both? Is the reaction barrier for T197A mutated PKA-substrate complex really higher than the wild-type if structural relaxation has been taken account of? In order to answer those questions, more systematic computational studies should be carried out on both the wild type and T197A mutated PKA-substrate complexes. In the present work, by simulating the dynamics of PKA-substrate complexes, studying the phosphoryl transfer reaction with combined *ab initio* QM/MM methods, and analyzing the global molecular motions, we have provide more detailed understanding about how auto-phosphorylation of Thr-197 modulates catalytic activity of PKA.

I.B.3 Computational Methods

In the current study, we employed the pseudobond *ab initio* QM/MM approach [41, 42, 83, 84, 85], which has been demonstrated to be powerful in the study of several enzymes, including enolase [44], acetylcholinesterase [86, 46] and 4-oxalocrotonate tautomerase [47, 48]. Throughout the study, the charged phosphate groups were included in the QM subsystem and were calculated at B3LYP/6-31G* level. Such a level of calculation is similar to that used in other contemporary studies [8, 9].

Preparation of the initial PKA-substrate complex, and the procedures of the molecular dynamics simulation and QM/MM calculations have been described in detail in our previous paper [80]. Here we only highlight several key points.

Molecular dynamics simulation

The preparation of the initial wild type PKA-substrate complex was based on the 1L3R crystal structure [28], and has already been described in detail in our previous paper [80]. For the T197A mutated model, pThr-197 was replaced with Ala in SYBYL7.0 [87]. Based on the pKa calculation with WHAT IF, His-87 has a neutral charge with only N_δ protonated. Therefore, including water molecules, there are 40,332 and 40,592 atoms in the wild type and T197A mutated models, respectively. In order to test whether pThr-197 regulates the active site conformation through hydrogen bonding via Arg-165, we have prepared a R165A mutant system. Including water molecules, there are 40,338 atoms in this model.

For each system, the minimization, equilibration and simulation procedures were exactly the same as in the ref [80]. Here we only highlight several key points. Molecular dynamics simulation with periodic boundary conditions has been conducted using the Amber 7.0 package [49]. The charge parameters of Mg_2ATP, phosphorylated serine and threonine have been determined in ref [80]. All other force field parameters are from the parm99 parameter set [51] and the polyphosphate parameters developed by Meagher et al.[52]. A default cutoff radius of 8 $\AA$ was introduced for non-bonded interactions, updating the neighbor pair list every 10 steps. The electrostatic interactions were calculated with the Particle Mesh Ewald method [53], and the SHAKE algorithm [54] was used to constrain all bond lengths involving hydrogens. The simulations have been performed under the constant pressure 1 atm and the constant temperature 300K.

Umbrella sampling

In order to calculate the potential of mean force (PMF) along the 1st side-chain torsion angle OG-C_β-C_α-N (χ_1) of the P-site Ser, the umbrella sampling technique [88, 89, 90] has been employed. The potential energy of the system was biased with a harmonic potential, $\frac{1}{2}\mathrm{K}(\chi_1 - \chi_{1,i})^2$, centered on successive values of $\chi_{1,i}$, where K is the harmonic force constant. A total of 36 windows have been employed, centered on -180°, -170°,..., 170° with a harmonic force constant K of 30 kcal/mol-rad^2. For each window, MD simulation consists of 50 ps equilibration and 200 ps sampling. A time step of 1 fs was used. From these 36 biased simulations, the PMF was obtained with the Weighted Histogram Analysis Method (WHAM) [91]. The self-consistent

set of equations were iterated until changes in the free energy constants F_i were less than 0.1 kcal/mol.

QM/MM study

The phosphate transfer reaction step in both wild type PKA and T197A mutant has been studied by a pseudobond *ab initio* QM/MM approach [41, 42, 83, 84, 85]. In order to take account of enzyme dynamics, multiple *ab initio* QM/MM minimum reaction energy pathways were computed in two steps [46]: generating enzyme-substrate conformations with molecular dynamics simulation, and determining the QM/MM reaction energy barrier for each initial structure as described in our previous study [80].

From MD trajectories of the wild type and the T197A mutant respectively, 9 equally spaced snapshots at 2, 3, .., 10 ns have been chosen as initial structures for QM/MM studies. For T197A mutant, the optimization procedure failed to get a converged reactant structure for the snapshot at 9 ns so that an additional snapshot at 11 ns was chosen. Since we are interested in the active site, the water molecules beyond 27 $\AA$ of the P_β atom of ATP were removed in our QM/MM system and only atoms within 20 $\AA$ of the P_β atom of ATP were allowed to move in QM/MM minimizations. Thus, each QM/MM system consists of PKA, ATP, SP20 (peptide) and around 2,700 water molecules, a total of around 10,000 atoms. Each initial structure for the QM/MM study was first energy minimized with the MM method. The criterion used for convergence is the root-mean-square (RMS) energy gradient being less than 0.1 kcal$\cdot mol^{-1}\AA^{-1}$.

In the QM/MM studies, each QM subsystem consists of the tri-phosphate arm of ATP, side chains of P-site Ser, Asp-166, and Lys-168, and two Mg^{2+} ions for a total of 49 atoms, while the rest are MM atoms. Enzyme reaction paths were determined by B3LYP/(6-31G*) QM/MM calculations with an iterative minimization procedure and reaction coordinate driving method [42]. Frequency calculations have been carried out to characterize the reactant, transition state and intermediate. In addition, single point B3LYP/(6-31+G*) QM/MM calculations have been carried out to calculate their energy differences. Throughout the QM/MM calculations, pseudobonds were treated with the 3-21G basis set and its corresponding effective core potential parameters [41]. The calculations were carried out using modified versions of the Gaussian98 [92] and TINKER programs [56]. For the QM subsystem, criteria used for geometry optimizations follow Gaussian98 defaults. For the MM subsystem, the convergence criterion used is to have

the RMS energy gradient be less than 0.1 $kcal \cdot mol^{-1}\AA^{-1}$. No cutoff for non-bonded interactions was used in the QM/MM calculations. This QM/MM calculation protocol was demonstrated to be successful with our wild type models [80].

Cross-Correlation Analysis

In order to investigate the correlated motion between different regions of a protein, such as the domain-domain communication [93, 94, 95, 96, 97], we have calculated cross-correlation coefficients for C_α displacements using wild type and T197A mutant MD trajectories respectively. The snapshots used were between 2 ns and 22 ns. The cross-correlation coefficient Corr(i, j) is given by:

$$Corr(i,j) = \langle \Delta r_i \cdot \Delta r_j \rangle / (\langle \Delta r_i^2 \rangle^{1/2} \cdot \langle \Delta r_j^2 \rangle^{1/2}) \quad (2)$$

Δr_i is the vector displacement from the mean position of the C_α atom in residue i. The angle brackets denote an ensemble average. Corr(i, j) can be collected in matrix form and displayed as a two-dimensional dynamical cross-correlation map (DCCM) [97]. Positive value of Corr(i, j) indicates that two atoms move in the same direction, whereas a negative value signals anti-correlated motion. In order to remove translational and rotational motion of the protein complex, we first moved the center of mass for each structure to the origin, and then employed the quaternion method to superimpose C_α atoms in each snapshot to the 1st structure in the production run.

Principal Component Analysis

Principal component analysis (PCA) is a powerful approach to reduce the dimensionality of a data set. When applied to analyze a MD simulation trajectory [96, 98, 99, 100, 101, 102, 103], it can separate large-scale collective motions from random thermal fluctuations. PCA analysis is based on the covariance matrix

$$Cov(i,j) = \langle (r_i(t) - \langle r_i \rangle_t) \cdot (r_j(t) - \langle r_j \rangle_t) \rangle_t \quad (3)$$

where r_i, r_j are Cartesian coordinates of atom i and j respectively. $< (quantity) >_t$ represents the average over the whole MD trajectory. The eigenvectors and eigenvalues of the covariance matrix yield the collective dynamic modes and their amplitudes.

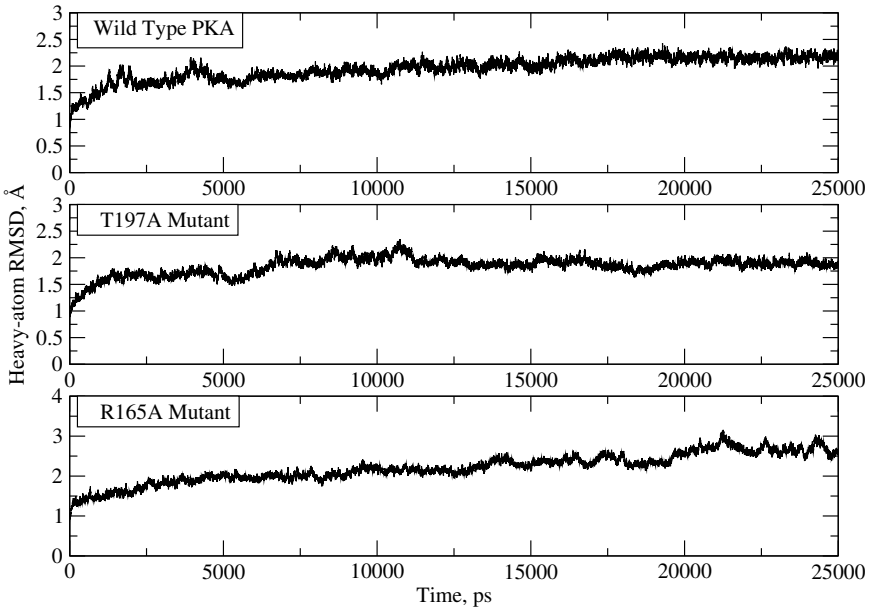

Figure I.12: Time dependence of rms deviations of heavy atoms of the wild type PKA, T197A and R165A mutants during 25 ns MD simulations, respectively.

The ptraj program in the Amber 8 package was employed to calculate covariance matrix elements. Since the diagonalization of the matrix for all atoms was found to exceed the memory capacity of the computer, only C_α atoms of both the PKA and peptide substrate were included in the analysis. We have employed porcupine plots [103] to visualize the collective dynamic modes. In this case, the functionally important motions include the opening of the active cleft and the inter-domain twisting, etc.

I.B.4 Results and Discussions

Stability of the trajectories

The molecular dynamics simulations of the wild type, T197A and R165A mutated PKA models were carried out for 25 ns respectively. As a measure of the structural stability, root-mean-square deviations (rmsd) for all heavy atoms found in the original PDB file between each snapshot and the initial structure were calculated, as shown in Fig. I.12. We can see that each trajectory is stable after 2 ns. Meanwhile, the temperature remains steady within 300$\pm$1.2 K over the course of the simulations.

Since there are an ATP ligand and the peptide substrate in the active cleft, we mea-

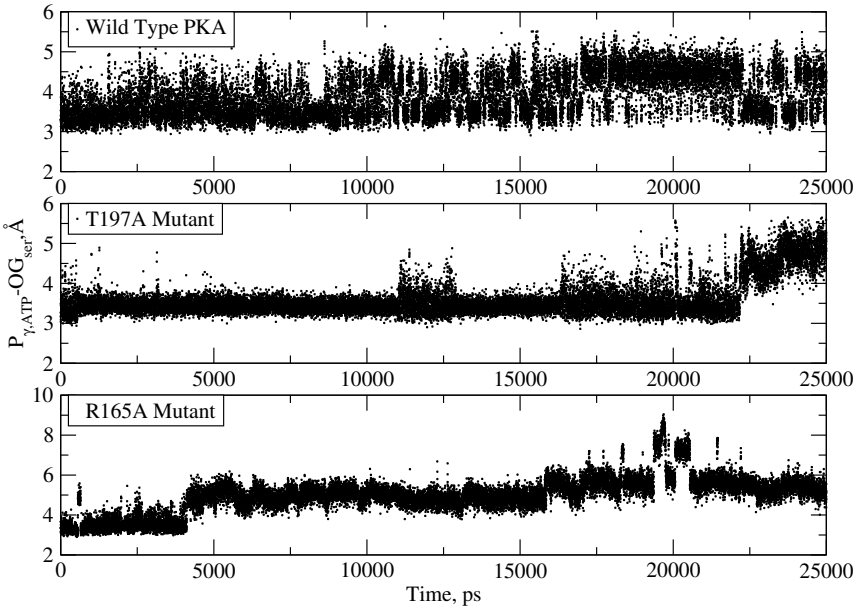

Figure I.13: Time dependence of the distance between ATP and the P-site Ser in the wild type PKA, T197A and R165A mutants during 25 ns simulations, respectively.

sured the distance between the P_γ atom of ATP and the hydroxyl atom OG of the P-site Ser to evaluate the stability of the substrate binding, as shown in Fig. I.13. Wild type PKA-substrate complex shows quite stable dynamic characteristics, with the average distance between P_γ and OG 3.95$\pm$0.46 $\AA$. The T197A mutant is stable for the first 16 ns MD simulation, but the distance increases a bit to around 5 $\AA$ after 22 ns, which might correspond to the larger $k_{peptide}$ and k_{ATP} in the T197A mutant [19]. Meanwhile, the corresponding distance between ATP and the P-site Ser in the R165A mutant is below 4 $\AA$ during the first 4 ns of MD simulation and then jumps to around 5 $\AA$. This indicates that Arg-165 might play a role in the binding affinity of the substrate peptide. The following analyses focusing on the active site of the T197A mutant are based on the trajectories between 2 ns and 22 ns.

Active-site configurations in the wild type PKA and T197A mutant models

Generally there are three different rotameric states for the first dihedral angle χ_1 of an amino acid side-chain. They are the G^+, G^- and T states (Fig. I.14) [104, 105].

The distributions of the χ_1 values of the P-site Ser during the MD simulations were calculated for the wild type and T197A mutant, respectively. As shown in Fig. I.15, the G^+

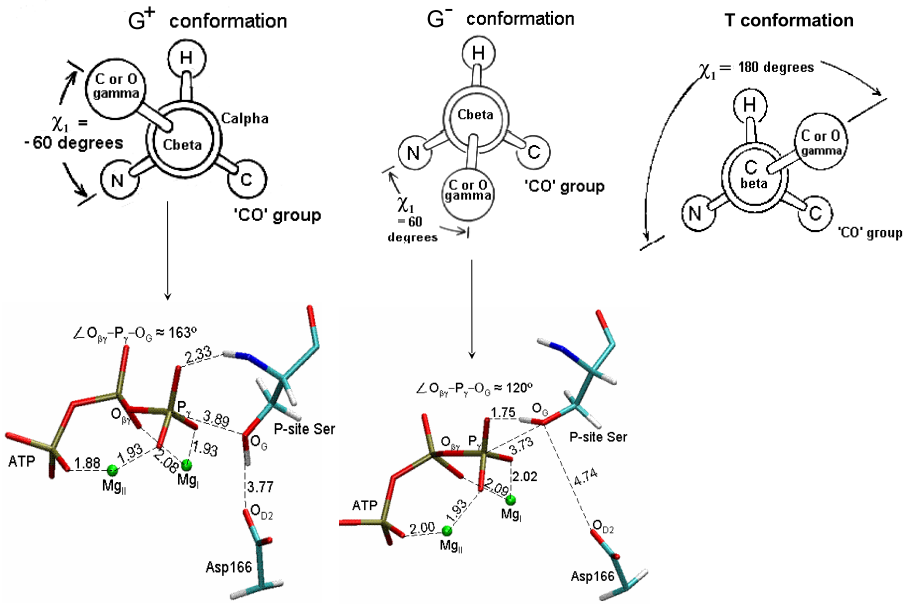

Figure I.14: The different rotameric states of a single amino acid and the corresponding stereo-image of the active site residues of the wild type PKA and T197A mutant interacting with ATP and the P-site Ser.

rotamer prevails in the MD trajectory of the wild type PKA model, while G^- is dominant in the T197A mutant. Similarly, due to the two different rotamer states of the P-site Ser, there are mainly two different configurations of the active site as shown in Fig. I.14. The G^+ rotamer features a hydrogen bond between the P-site Ser and Asp-166, the average distance between the OD2 atom of Asp-166 and OG of the P-site Ser is 3.77±0.61 $\AA$. The average distance between OG and the P_γ atom of ATP is 3.89±0.51 $\AA$ and the angle of OG, P_γ and $O_{\beta\gamma}$ is about 163±9°. In contrast, for the G^- rotamer, the P-site Ser forms a hydrogen bond with the non-bridging O_γ of ATP instead of Asp-166. The average distance between OG and OD2 is 4.74±0.55 $\AA$, and the average distance between OG and P_γ is 3.73±0.47 $\AA$, while the angle of OG, P_γ and $O_{\beta\gamma}$ is only around 125±14°. According to our previous study on the crystal structure (PDB code: 1L3R) [80], the G^+ rotamer should be catalytically more active, with Asp-166 serving as the catalytic base. G^- is more thermostable in the T197A mutant, in which the P-site Ser forms a hydrogen bond with the ATP. The result is consistent with the experimental observations of several X-ray crystal structures of both the PKA [31] and phosphorylase kinase [106, 107], as well as the thermo-stability analysis on PKA-substrate complexes [70].

The PMFs for the transition between the two rotamers have been calculated using the

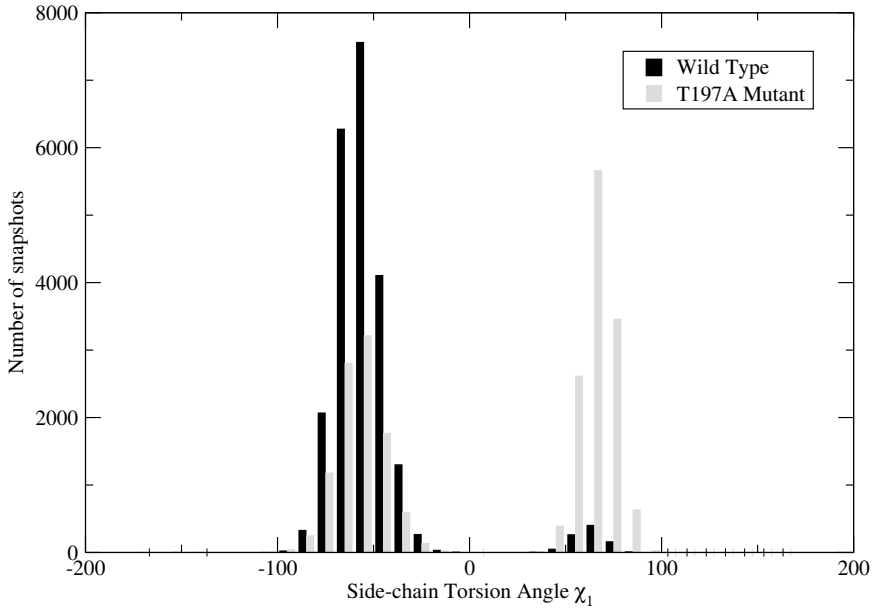

Figure I.15: The side-chain torsion angle distribution of the P-site Ser χ_1 distributions in the wild type PKA and T197A mutant.

umbrella sampling technique and are displayed in Fig. I.16. In the absence of PKA, the G^+ rotamer is much more stable than the G^-. The relative free energy difference is around 1.4 kcal/mol and the transition barrier from G^+ is $\sim$3.6 kcal/mol. In the wild-type PKA, the G^+ rotamer is more stable by less than 1 kcal/mol and the transition barrier is $\sim$ 5 kcal/mol. In the T197A mutant, the G^- is more stable, which is consistent with Fig. I.15.

As shown in Fig.I.11, the residue Arg-165 is directly connected to both pThr-197 and Asp-166, the catalytic base in the active site. In order to test whether pThr-197 regulates the active site conformation through Arg-165, a 15 ns MD simulations on R165A mutant has been carried out. From Fig.I.17, it can be seen that the side-chain conformations of the P-site Ser in the R165A mutant is similar to that in the wild-type PKA although the replacement of Arg-165 with Ala disconnects the interactions between the pThr-197 and the active site. This result suggests that pThr-197 does not affect the side-chain conformation of the P-site Ser via Arg-165, although the P-site Ser binding affinity has been weakened with the replacement of Arg-165 with Ala (Fig.I.13), which is consistent with the conclusion from a recent structural analysis [76].

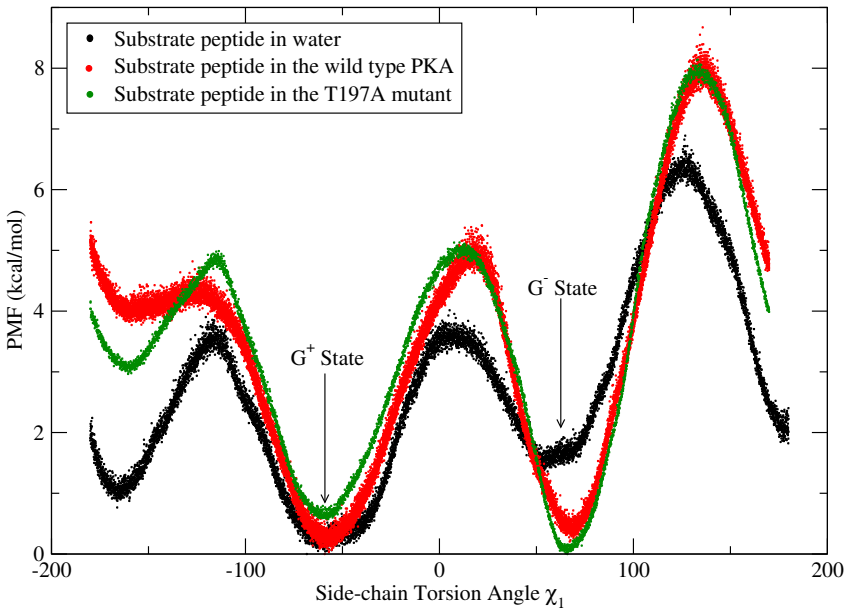

Figure I.16: The free energy barriers for the reorientation of the side-chain of the P-site Ser in the wild type and T197A mutated PKA-substrate complex.

Table I.3: Individual residue contributions to the transition state stabilization or destabilization ($|\Delta E_i^{tot}| \geq 0.8$ kcal/mol), calculation based on B3LYP(6-31+G*)/MM calculations. VDW refers to the van der Waals interaction energy, ELE refers to the electrostatic interaction energy. "MM Total" refers to the interaction of all residues between Asp184 and Arg280 and QM subgroups. Energy units are in kcal/mol.

Categories[a]	Residue	$\Delta E_{i,1L3R}^{vdw+ele}$	$\Delta E_{i,1ATP}^{vdw+ele}$	Region[b]
		from RS to TS		
1	Lys213	0.8	1.3	IX
	Lys249	1.1	1.6	X
	Arg280	1.2	1.8	XI
2	(P)Thr197	-1.8	-2.6	VIIIa
	Glu203	-3.4	-4.7	VIIIb
	Glu208	-1.2	-1.9	VIIIc
	Asp220	-1.9	-3.3	IX
	Glu230	-1.9	-2.8	IX
	Glu241	-1.0	-1.4	X
	Glu248	-0.9	-1.3	X
3	Thr201	-4.2	0.6	VII
MM Total		-13.4	-12.6	

[a] The residues in the 1st category are the positively charged and destabilize the transition state. The residues in the 2rd category are those having negative charges and stabilizing the transition state. The 3rd category includes the residues which have no net charges.

[b] The regions correspond the different subdomains, as defined by Hanks et al. [68].

Table I.4: The interaction between individual Mg^{2+} ions with the rest of the atoms in the QM subgroup. The energy unit is kcal/mol.

	B3LYP(6-31+G*)/MM		MP2(6-31+G*)/MM	
	1L3R	1ATP	1L3R	1ATP
		Mg_I		
Δ(TS-RS)	-12.4	-30.9	-13.4	-33.4
Δ(Int.-RS)	-42.9	-40.9	-46.6	-43.9
		Mg_{II}		
Δ(TS-RS)	-40.1	-83.8	-45.0	-92.6
Δ(Int.-RS)	-86.0	-91.6	-96.0	-100.7

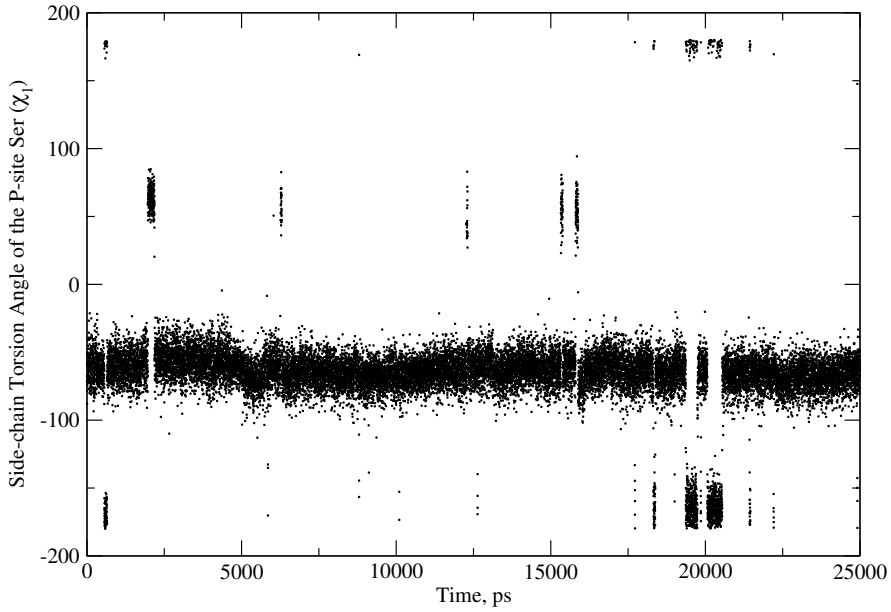

Figure I.17: Time dependence of the side-chain torsion angle χ_1 of the P-site Ser in the R165A mutant.

The phosphoryl transfer reaction barrier

To quantitatively describe the effect of activation loop phosphorylation on the phosphoryl transfer reaction barrier, we have calculated the reaction barriers with different initial structures for both the wild type and T197A mutant with DFT QM/MM calculations. Despite the two different conformations in the active site, our QM/MM studies indicate that only the G^+ conformation can directly participate in the phosphoryl transfer reaction, as shown in Tables.I.5 and I.6. It is necessary that Asp-166 is available as the catalytic base to accept the hydroxyl proton in the late stages of the phosphoryl transfer. In the G^- conformation, the P-site Ser must always first rotate its side-chain to the favorable G^+ to form a hydrogen bond with Asp-166, and then can participate in the phosphoryl transfer reaction.

The calculated reaction barriers for wild type PKA and the T197A mutant are summarized in Tables. I.5 and I.6 respectively. We can see that different initial structures lead to fluctuations in the reaction energy barriers. The average QM/MM reaction barrier for the phosphoryl transfer is 13.7 $\pm$ 2.2 kcal/mol for the wild type PKA, while it is 17.0 $\pm$ 2.9 kcal/mol

Table I.5: Energy barriers for the phosphoryl transfer reaction in the wild-type PKA enzyme. The energy unit is kcal/mol, the distance unit is *Å*, and the angle unit is °.

No.	Initial Structure			Reactant State			Activation
	χ_1	OG-P_γ	$O_{\beta\gamma}-P_\gamma$-OG	χ_1	OG-P_γ	$O_{\beta\gamma}-P_\gamma$-OG	Barrier[a]
2001	-55.4	3.56	179.8	-60.2	3.45	174.8	15.8
3001	16.1	3.66	171.3	-49.6	3.32	176.6	14.3
4001	-58.5	3.19	169.2	-65.8	2.97	170.7	12.9
5001	-57.0	3.70	154.9	-65.4	3.77	172.5	18.3
6001	-52.2	3.24	167.2	-62.3	3.30	166.5	11.9
7001	-53.9	3.37	165.7	-64.8	3.37	172.7	12.3
8001	-48.5	3.24	160.2	-67.2	3.54	175.2	13.8
9001	-53.9	3.37	165.7	-67.9	2.95	169.9	11.7
10001	-55.2	3.21	165.2	-57.5	2.97	168.0	12.6
average	-	-	-	-62.3	3.29	171.9	13.7±2.2

[a] The method used for the QM subsystem is the single-point B3LYP/6-31+G* calculation based on the geometries optimized at the B3LYP/6-31G* level.

for the T197A mutant. The average barriers are quite consistent with the experimental reaction rate constants for the phosphoryl transfer step which are $500s^{-1}$ and $3.6s^{-1}$ for the wild type and T197A mutant, respectively [34]. It should be noted that any single calculation of the barrier is not necessarily close to the average, and it is not meaningful to compare the individual barriers between the wild type PKA and the T197A mutant since their initialstructures are quite different. In addition, we have calculated the contribution of pThr-197 and Ala-197 to the transition state stabilization based on the geometries of all the QM/MM models of the wild type and T197A mutant, respectively. Our calculations indicate that on average the pThr-197 in the wild type PKA contributes about -3.4±0.9 kcal/mol to stabilize the transition state in comparison with the reactant, while the contribution of Ala-197 in the T197A mutant is less than -0.2 kcal/mol. This result is quite consistent with the difference in the average reaction energy barrier, which indicates that pThr-197 plays an important role in facilitating the phosphoryl transfer reaction

Table I.6: Activation barriers for the phosphoryl transfer reaction in the T197A mutant. The energy unit is kcal/mol, the distance unit is *Å*, and the angle unit is °.

No.	Initial Structure			Reactant State			Activation
	χ_1	OG-P_γ	$O_{\beta\gamma} - P_\gamma$-OG	χ_1	OG-P_γ	$O_{\beta\gamma} - P_\gamma$-OG	Barrier[a]
2001	59.3	3.44	134.9	-53.2	3.03	155.2	15.2
3001	65.8	3.43	144.6	-53.2	3.28	168.4	21.7
4001	66.4	3.36	136.2	-48.8	2.91	170.7	19.2
5001	62.0	3.45	139.0	-54.6	2.94	175.6	19.1
6001	63.6	3.37	136.8	-53.9	3.00	167.2	12.8
7001	65.1	3.47	133.8	-57.2	3.42	170.0	19.4
8001	64.5	3.39	133.7	-63.8	3.52	174.3	14.1
9001[b]	65.2	3.41	136.5	-44.9	2.95	166.7	16.2
10001[b]	58.1	3.38	138.3	-42.3	3.04	175.0	15.5
average	-	-	-	-53.2	3.11	169.3	17.0±2.9

[a] The method used for the QM subsystem is the single-point B3LYP/6-31+G* calculation based on the geometries optimized at the B3LYP/6-31G* level.

[b] Here 9001 and 10001 correspond the snapshots at 10 ns and 11 ns, respectively.

through the electrostatic stabilization of the transition state.

Cross-correlation analysis for the wild type and T197A mutant

In order to reveal the correlated motions, we have calculated a two-dimensional dynamical cross-correlation map (DCCM) for all the C_α atoms in the C subunit of PKA (residues 14 - 350) using the wild type and T197A mutant MD trajectories respectively, as shown in Fig. I.18. The snapshots used were between 2 ns and 22 ns.

From Fig. I.18, we can see that the two dynamical cross-correlation maps are quite different. In the wild type PKA, the dynamics of the small lobe (residues 14 - 119) and the C-terminal (residues 300 - 350) are strongly correlated. Several loops such as the catalytic loop (residues 166 - 171) and the Mg^{2+} positioning loop (residues 184 - 187) display strongly correlated motion with the small lobe as well. However, the region of the hinge between the small

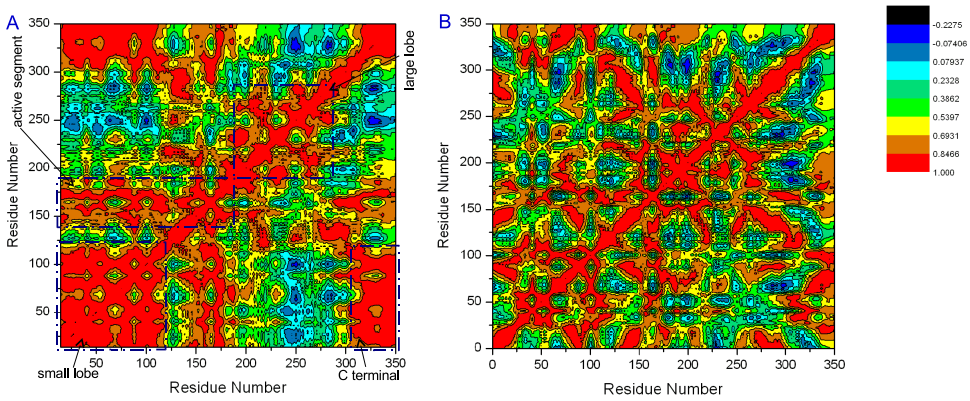

Figure I.18: Calculated residue-residue-based correlated motions within 2-20 ns MD simulations of the wild type PKA and T197A mutant. (A) is for the wild type PKA, (B) is for the T197A mutant.

and large lobe and the G-helix (residues 241 - 260)in the large lobe are anti-correlated with the small lobe and C terminal. This observationis quite consistent with the catalytic activity of the wild type PKA. In the ATP binding pocket, the glycine-rich loop (residues 47 - 58), the catalytic loop and the Mg^{2+} positioning loop all directly bind with the substrate ATP. The correlated motionreflects the stronger substrate binding, which might help to stabilize the G^{+} configuration discussed above. However, in the T197A mutant, the correlated motions have been weakened significantly (Fig. I.18 (b)). It indicates that pThr-197 may be an important bridge connecting the small lobe with the large lobe, which could facilitate cooperative operation of the two lobes during the enzyme action.

Collective modes of motion in the wild type and T197A mutant

We have performed principal component analysis to calculate and visualize the essential modes of motion using both the MD trajectories in the time interval of 2 ns to 22 ns of the wild type and T197A mutated PKA.

To eliminate the noise of the N/C terminal, we truncated the first and last 10 residues in both PKA structures. In other words, 317 backbone C_α atoms were sampled over 20,000 consecutive structures with a time increment of 1 *ps*. The below analysis indicates that our results are consistent with the above cross-correlation analysis, and have provided more detailed information regarding the internal motions of the different subunits.

The PCA averaged in the block of time interval of 10-22 ns agrees with results in the timeinterval of 2-22 ns. The corresponding figures of the wild type PKA are in "supplemental materials"[2] (not shown for the T197A mutant). The agreement between the two different timeintervals suggests that a converged picture of the collective motions emerges for the last12 ns. Overall, salient PCA motion modes, in sufficiently converged MD simulations, reveal the dynamic characteristics of the protein.

For the wild type PKA, the first two eigenvectors account for $\sim$87% of the motion observed in the first 22 ns of the simulation trajectory, with cosine contents [108] of 46% and 65%, respectively. The relative contributions of different eigenvectors to the overall motion are shown in Fig.I.19. And these eigenvectors for the PKA (except the first and last 10 residues of the N-terminal and C-terminal, respectively) are shown in Fig.I.20,W_I-II with the stick-cone

[2]http://www.proteinscience.org/cgi/content/full/ps.051852306/DC1

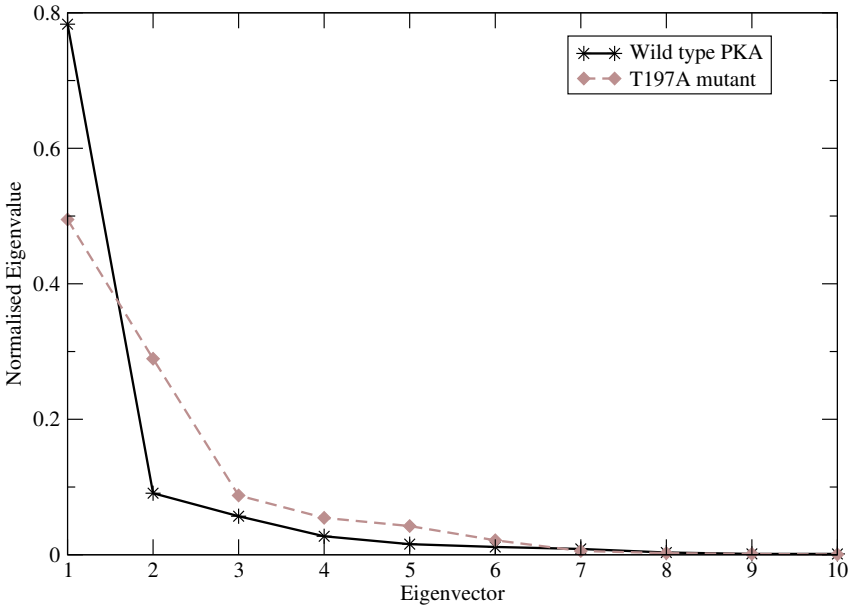

Figure I.19: Principal dynamic modes of the wild type PKA. W_I, II, porcupine plots of the first two most substantial principal motions of the wild type PKA, respectively. The blue color represents the small lobe, the purple for the activation segment, the lime for the large lobe, the white for the C-terminal and the pink for the substrate peptide.

representation.

The most significant motion of the wild type PKA in the context of a PKA-substrate complex is a "breathing" mode (Fig.I.20.*W_I*) with the two domains of the protein moving in opposition around the "hinge" region (residues 120 - 127). This region forms its own interaction with the edge of the ATP molecule and connects the N- and C-terminal lobes, each of which independently contributes a surface to the ATP binding site. Strikingly, the activation segment shown in purple shows a similar but less pronounced motion as the small lobe, which is consistent with our above cross-correlation analysis. By far the biggest contributor is this breathing mode. The axis of this motion is through a conserved residue Arg-171. As the protein kinase breathes, the active site including the activation segment opens and closes. The second most significant internal motion is a mixture of rotation and twisting between the two lobes. As shown in Fig.I.20,*W_II*, the twisting motion is around an axis perpendicular to the most significant motion mode, in which the active segment together with the rest of the residues in the large lobe move in the opposite direction with the small lobe. A similar motion has also been found in a study of ADP release [109].

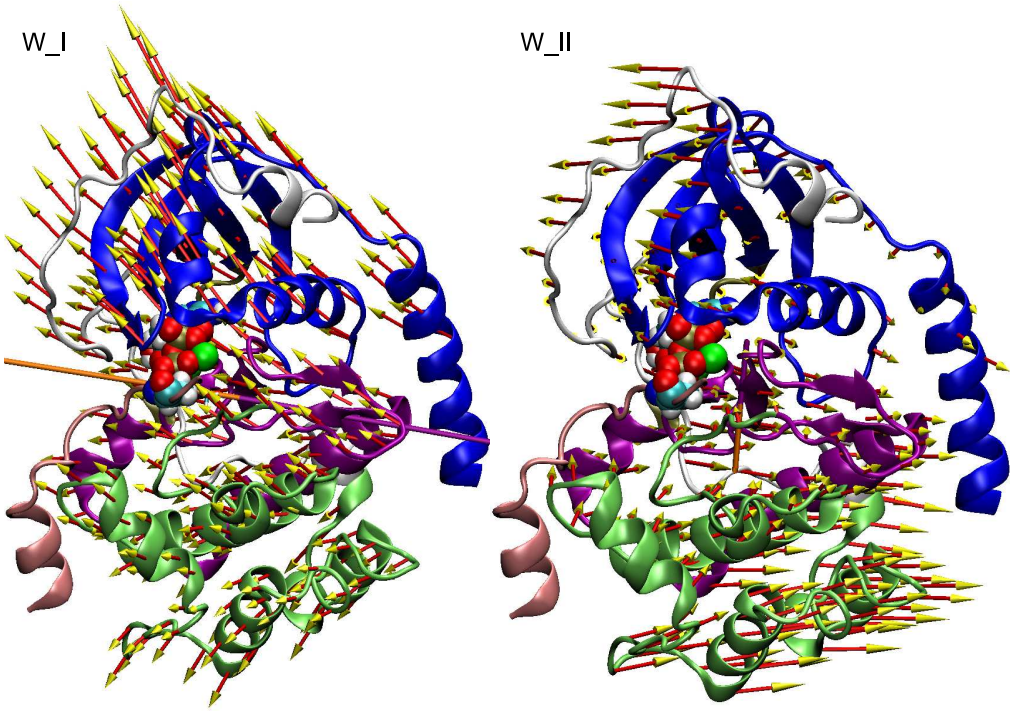

Figure I.20: Relative contributions of different modes (eigenvectors) to the overall motion are shown for the wild type and T197A mutant. The data are renormalised so that the eigenvalues for each set add up to unity.

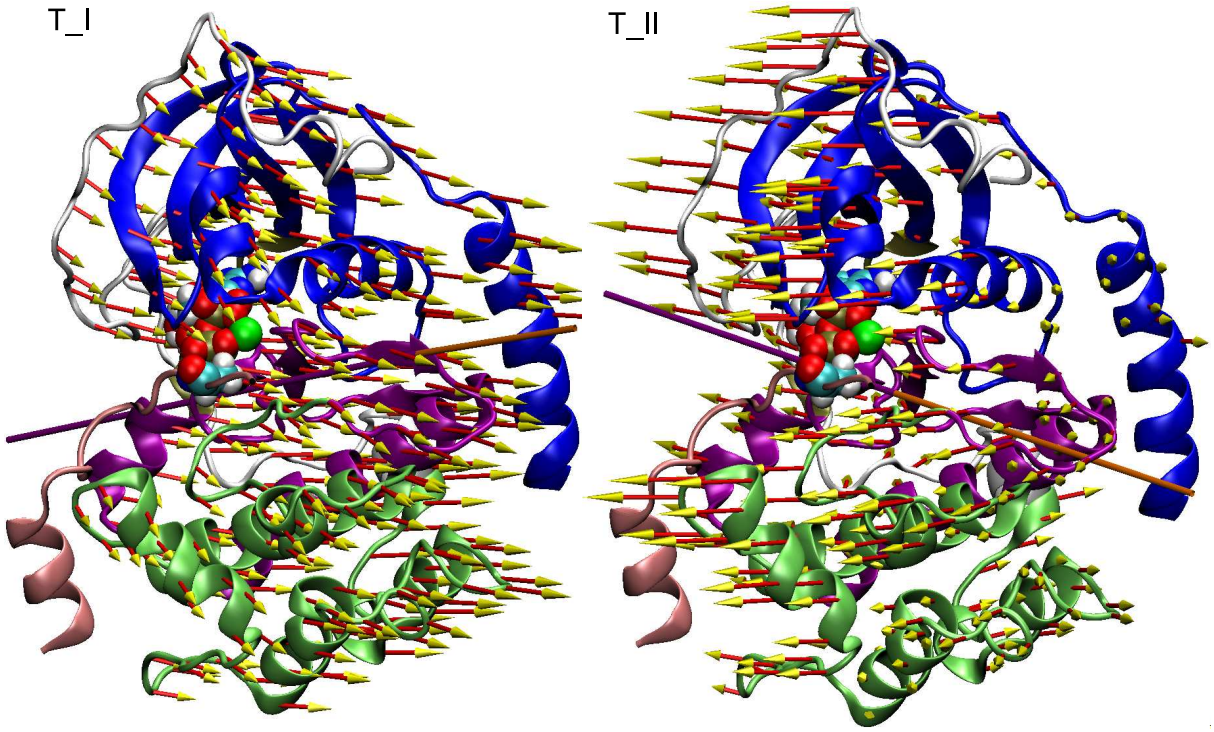

Figure I.21: Principal dynamic modes of T197A mutant. T_I and II, the first two most substantial principal motions of the T197A mutant.

In comparison with the wild-type PKA, the collective motions in the T197A mutant are quite different (Fig. I.21 and I.22,$T\_I - III$). The first three eigenvectors contribute to 49%, 29% and 9% in the overall modes. The first most significant motion corresponds to a translation-like mode. The second and third correspond to the rotation-like twisting motions. These three motions don't include inter-domain twisting, which might control the opening and closing of the active site. This result indicates that the replacement of pThr-197 not only directly disrupts part of the hydrogen bonding network between the small and large lobes, but dramatically affects the internal motion, which might play an important role in regulating the active site conformations.

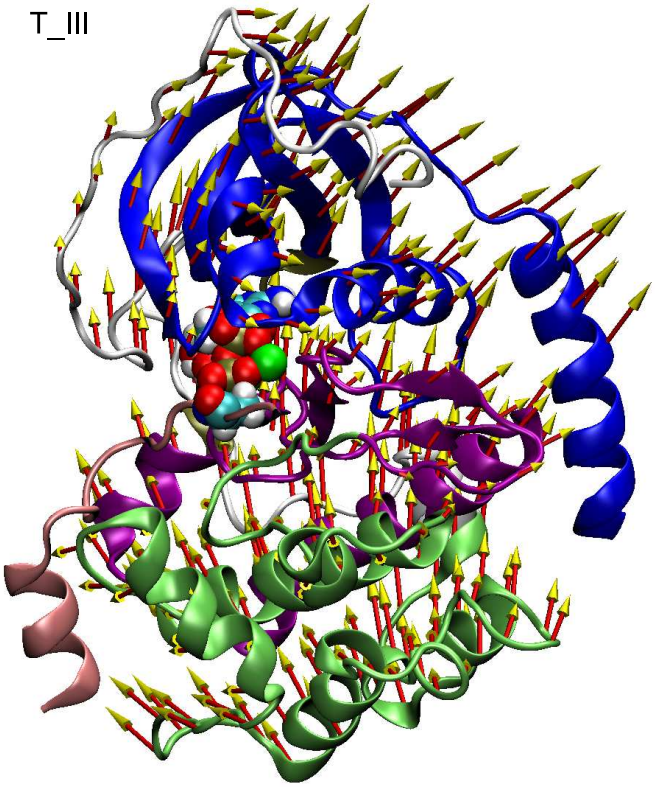

Figure I.22: Principal dynamic modes of T197A mutant. T_III, the third most substantial principal motion of the T197A mutant.

I.B.5 Conclusions

The role of the phosphorylated Thr-197 in the cAMP-dependent protein kinase has been investigated and discussed with both molecular dynamics and density functional theory QM/MM calculations. The P-site Ser mainly occupies the active G^+ state in the wild type PKA, but the alternate rotamer G^- in the T197A mutant. The transition barrier between the two states is about 5 kcal/mol. Phosphoryl transfer can only take place with the active G^+ conformation. In the T197A mutant, the inactive G^- P-site Ser dominates the MD trajectory, therefore, conformational changes must accompany the catalytic turnover.

We have calculated B3LYP(6-31+G*) QM/MM barriers for both the wild type PKA and T197A mutant with multiple initial structures. The simple averages of the 9 activation barriers are 13.7$\pm$2.2 kcal/mol for the wild type PKA, and 17.0$\pm$2.9 kcal/mol for the T197A mutant. The results are consistent with experimental reaction rates from kinetic studies. By comparison, although the auto-phosphorylation of Thr-197 doesn't substantially affect the fold of the activation segment, the electrostatic interaction with the active site contributes to the stabilization of the transition state and activation of the wild type PKA, which is consistent with our previous results using two PKA-substrate crystal structures, providing a synergistic understanding to the role of pThr-197 [80].

Our molecular dynamics simulations find different collective motion modes between the wild type PKA and T197A mutant. The inter-domain twisting motion is only captured in the wild type PKA, which might contribute to the open and closing of the active site. Cross-correlation analysis on both the wild type PKA and T197A mutant further confirms the correlated motions between the small and large domains in the wild type PKA. However, such correlation has been substantially weakened in T197A mutant. Overall, our results indicate that pThr197 not only facilitates the phosphoryl transfer reaction by electrostatically stabilizing the transition state, but also strongly affects its essential protein dynamics as well as its active site conformation.

I.B.6 Acknowledgments

This work has been supported in part by grants from the NSF and NIH. Additional support has been provided by NBCR, CTBP, HHMI, the W. M. Keck Foundation, and Accelrys,

Inc. Y. Z. thanks NYSTAR for a James D. Watson Young Investigator award.

I.C Acetylcholinesterase: Mechanisms of Covalent Inhibition of Wild-type and H447I Mutant Determined by Computational Analyses

I.C.1 Abstract

The reaction mechanisms of two inhibitors TFK^+ and TFK^0 binding to both the wild-type and H447I mutant mouse acetylcholinesterase (mAChE) have been investigated by using a combined *ab initio* quantum mechanical/molecular mechanical (QM/MM) approach and classical molecular dynamics (MD) simulations. In the wild-type mAChE, the binding reactions of TFK^+ and TFK^0 are both spontaneous processes, which proceed through the nucleophilic addition of the Ser203-O_γ to the carbonyl-C of TFK^+ or TFK^0, accompanied with a simultaneous proton transfer from Ser203 to His447. No barrier is found along the reaction paths, consistent with the experimental reaction rates approaching the diffusion-controlled limit. By contrast, TFK^+ binding to the H447I mutant may proceed with a different reaction mechanism. A water molecule takes over the role of His447 and participates in the bond breaking and forming as a "charge relayer". Unlike in the wild-type mAChE case, Glu334, a conserved residue from the catalytic triad, acts as a catalytic base in the reaction. The calculated energy barrier for this reaction is about 8 kcal/mol. These predictions await experimental verification. In the case of the neutral ligand TFK^0, however, multiple MD simulations on the TFK^0/H447I complex reveal that none of the water molecules can be retained in the active site as a "catalytic" water. Furthermore, our alchemical free energy calculation also suggests that the binding of TFK^0 to H447I is much weaker than that of TFK^+. Taken together, our computational studies confirm that TFK^0 is almost inactive in the H447I mutant, and also provide detailed mechanistic insights into the experimental observations.

I.C.2 Introduction

Acetylcholinesterase (AChE, EC 3.1.1.7) is a hydrolytic enzyme that belongs to the serine hydrolase family. It plays important roles during the course of signal transmission at cholinergic synapses. The principal biological role of acetylcholinesterase is the termination of impulse transmissions by rapidly hydrolyzing the neurotransmitter, acetylcholine (ACh) [110,

111, 112]. Dysfunctions of AChE or other components of cholinergic synapses are involved in several human diseases, including myasthenia gravis, glaucoma, Alzheimer's and Parkinson's diseases [113, 114, 115, 116, 117, 118]. As a result, AChE has become an important target for rational drug design.

The crystal structure of AChE is characterized by a deep narrow gorge which penetrates halfway into the enzyme and contains the catalytic site located near the bottom, *ca.* 20 $\AA$ deep [119]. Kinetic studies have revealed that AChE possesses a remarkably high activity, with an ACh turnover rate of about $10^4 s^{-1}$ under physiological conditions, approaching the diffusion-controlled limit [120, 121, 122].

Similar to many other proteases, the catalytic triad in AChE consisting of Ser203(200) [123], His447(440) and Glu334(327) is believed to be essential to hydrolysis. Each of these three residues has a specific role in generating the nucleophilic potential at the seryl O_γ. The replacement of any of them with Ala can cause at least 3300-fold of activity loss [124]. The detailed acylation reaction mechanism based on both experimental and theoretical explorations [125, 45] is shown in Fig.I.23(a). Ser203 and His447 are believed to be directly involved in the bond breaking and forming. Ser203 serves as a nucleophilic attacking site, and the imidazole group of His447 acts as a catalytic base which accepts one proton transferred from Ser203. However, for the third residue in the catalytic triad, Glu334, its detailed role remains elusive up to now [126]. In previous studies, in addition to maintaining the productive orientation of His447 [127], at least three different catalytic roles of Glu334 have been proposed. First, the "charge-relay" mechanism suggests that Glu334 functions as a catalytic base, which accepts one proton from the N_δ atom of His447 [128, 129, 130]; the second is a "low-barrier hydrogen bond or short, strong hydrogen bond (LBHB or SSHB)" mechanism, originally proposed based on NMR studies [131, 132, 133, 134], in which a short hydrogen bond between O_δ of Glu334 and N_δ of His447 ($< 2.65\AA$) is thought to supply 10-20 kcal/mol "resonance stabilization" to the transition state [126, 135, 136, 137]; recent experimental and theoretical studies also pointed to a third possible mechanism, in which the electrostatic interaction between the carboxylate of Glu334 and the incipient imidazolium cation stabilizes the transition state and intermediate [138, 139, 140, 45]. The proton is mostly localized on His447-N_δ, and hence it is not participating in a low-barrier hydrogen bond. When the proton hopping occurs, it has a destabilizing effect on the intermediate [141, 142].

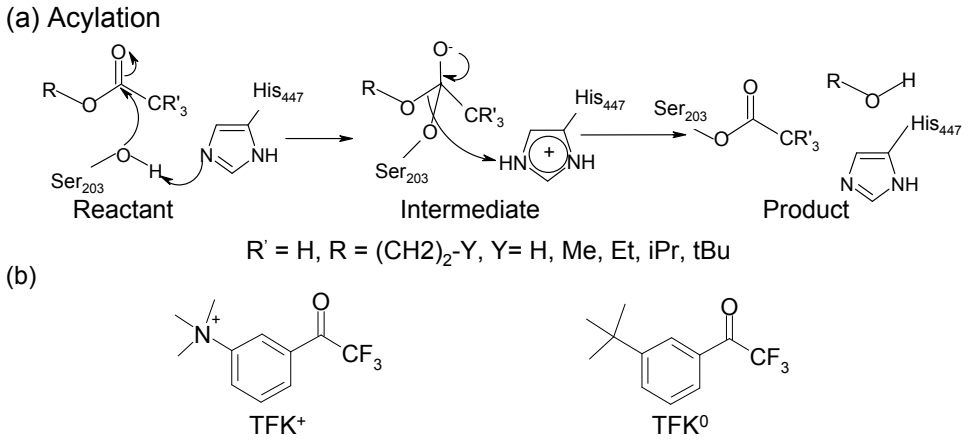

Figure I.23: (a) The acylation mechanism in the wild-type AChE enzyme; (b) The chemical structures of TFK^+ and TFK^0.

However, recent experimental mutagenesis studies have brought new challenges to all the above proposed reaction mechanisms. TFK^+ (m-(N,N,N-trimethylammonio)trifluoroacetophenone (TMTFA)) (see Fig. I.23 (b)), a common inhibitor to AChE, can still react with the mouse AChE (mAChE), even with the replacement of His447 by a hydrophobic Ile. In contrast, its neutral analog, TFK^0, shows no apparent binding activity to H447I mutant, while it shows slightly reduced binding to the wild-type mAChE as compared to TFK^+ (see Table I.23). Additionally, Ser229, which makes direct contact with the sidechain of Glu334, is believed to be essential to maintaining the integrity of the catalytic triad; its critical importance for the enzymatic activity seems unique to the cholinesterases [143]. However, substitution of Ser229 with an Asn residue, at an equivalent position in Zebra fish AChE, yields a protein with no detectable catalytic activity [144]. So far, how Ser229 is involved in AChE acylation is still an open question.

In order to explore the enzymatic activity of H447I mutant mAChE, as well as the role of Ser229 in the acylation reaction, we have performed computational studies on both TFK^+ and TFK^0 binding to the wild-type and H447I mutant mAChEs, using a combined *ab initio* quantum mechanical and molecular mechanical (QM/MM) approach, as well as multiple MD simulations. In our study, a water molecule is found to play an essential catalytic role in place of His447 in the binding reaction of TFK^+ to the H447I mutant. Along with this water molecule, Ser203 and Glu334 form a new stable catalytic triad. During reaction, Ser203 delivers a proton to the water

Table I.7: The rate constants for association and dissociation of inhibitors TFK^+ and TFK^0 with mouse AChEs measured by experiments [1, 2]. The units of k_{on} and k_{off} are $10^9 M^{-1} min^{-1}$ and $10^{-3} min^{-1}$, respectively.

	wild-type mAChE		H447I mutant mAChE	
	k_{on}	k_{off}	k_{on}	k_{off}
TFK^+	980 ± 60	1.1 ± 0.3	$\sim 10^a$	$\sim 1.0^a$
TFK^0	2.2 ± 0.3	15 ± 1	N/A^b	N/A^b

[a] Unpublished data.

[b] There is no apparent binding affinity detected.

molecule while the water molecule serves as a charge relayer to pass one proton to Glu334. The QM/MM free energy barrier for the reaction is lower than 8.0 kcal/mol. On the other hand, the water triad was unable to be retained in the corresponding TFK^0/H447I complexes from multiple MD simulations, indicating that TFK^0 might not be able to stably bind to the H447I mutant. To further validate our QM/MM calculations, we also used thermodynamic integration (TI) calculations to investigate the binding energy differences between TFK^0 and TFK^+ in both the wild-type and H447 mutant enzymes. The TI calculations also suggest that the binding of TFK^+ to both enzymes is much stronger than the neutral analog TFK^0, which is consistent with experimental observations as well as the above QM/MM calculations.

I.C.3 Computational methods

Construction of wild type complex models

Our starting point is the X-ray structure of AChE-TFK$^+$ complex (PDB code:2H9Y) [145], in which a covalent bond is formed between TFK$^+$ and Ser203-O_γ (denoted as the [W-T$^+$] model [146]). Missing hydrogen atoms for the protein were added via InsightII [147], while hydrogens for conserved crystal waters were added and optimized by WHATIF [50]. For histidine residues, calculations of the local electrostatic microenvironment and the effective pK_a with WHATIF indicated that His447 should be protonated on both N_ε and N_δ, while the others are neutral residues: HID381, HID387, HID405 with N_δ protonated; HIE212, HIE223, HIE284, HIE287, HIE393, HIE432 with N_ε protonated. The [W-T^0] model was obtained by manually

modifying TFK^+ to its neutral analogue TFK^0. The atomic charges for both TFK^+ and TFK^0 as well as Ser-TFK^+ and Ser-TFK^0 were derived by fitting to HF/6-31G* electrostatic potentials (ESP) using the RESP module. Other force parameters for TFK^+ and TFK^0 were adapted from the standard force field by following the general parametrization procedures outlined in AMBER manual [51, 148].

After relaxing the added atoms in the gas phase, each structure was immersed in a cubic TIP3P water box and neutralized by addition of Na^+ counter-ions using the AMBER Leap module. This led to the [W-T^+] simulation system of 70017 atoms and [W-T^0] simulation system of 72598 atoms, respectively. MD simulations were conducted in the NPT ensemble at 300 K and 1 atm. The SHAKE algorithm [54] was used to constrain all bond lengths involving hydrogens. A 10.0 $\AA$ cutoff was used for nonbonded interactions, the neighbor pair list was updated every 10 steps. The long-range electrostatic interactions were treated with the Particle Mesh Ewald method [53]. The two prepared systems were first equilibrated with a series of minimizations interspersed by short MD simulations, and then extended to 10 ns MD simulations.

In each MD simulation trajectory, two snapshots, one from the first 1 ns and one from the last 1 ns, were selected for the following QM/MM investigations. These selected structures were first minimized using the MM method, and then optimized with the B3LYP(6-31G*) QM/MM calculations using an iterative minimization approach [42], finally leading to four [W-T^+] and [W-T^0] structures.

Construction of H447I mutant complex models

Since there is no crystal structure of the H447I mutant so far, we tried two approaches to prepare the initial noncovalent complex structure of H447I and TFK^+ (denoted as the [$M \cdot T^+$] model). The first approach is to use the multiple docking approach introduced by Kua et al.[149]. His447 in the apo mAChE crystal structure (PDB code: 1J06) was manually modified to Ile, and then TFK^+ was docked into 1,000 snapshots evenly chosen from the last 1 ns trajectory of a 10 ns apo H447I mutant MD simulation. The Autodock 3.0 program [150] was used for all the docking studies. The search method used was the Lamarckian genetic algorithm (LGA) set at level 2 with the top 6 structures reported. Finally, according to the criteria suggested in Kua et al.[149] , the best 6 complex structures were selected and immersed into explicit water boxes , and subsequent MD simulations were set up to relax each system. To prevent TFK^+

dislocation from the esteratic binding site, a 20.0 kcal/(mol·$Å^2$) harmonic restraint between the carbonyl-C of TFK^+ and Ser203-O_γ was applied during simulations. The second approach is to start from the noncovalent [$W \cdot T^+$] structure obtained from our QM/MM calculations of the wild-type enzyme with TFK^+(see below for details), and then manually replace HID447 (Note: The N_ε proton originally in the [$W - T^+$] complex is transferred to Ser203 in the [$W \cdot T^+$] model after the QM/MM run) with Ile. Another MD simulation of the resulting system was then set up by following the same procedure as outlined in the first approach. The total number of atoms in these 7 MD simulations is around 70,000-75,000. Similarly, 7 initial models of H447I and TFK^0 ([$M \cdot T^0$]) were obtained with the same procedure. Additionally, an 8th [$M \cdot T^0$] model was obtained by directly modifying TFK^+ to TFK^0 in one of the [$M \cdot T^+$] models. Therefore, a total of 8 [$M \cdot T^0$] models were prepared and subjected to further theoretical investigations.

QM/MM free energy calculations

The pseudobond *ab initio* QM/MM approach [41, 42] has achieved great success in accurate modeling of the chemistry at an enzyme active site while properly including the effects of the enzymatic environment. It has been applied to various enzyme reactions, including enolase [44], acetylcholinesterase [45], 4-oxalocrotonate tautomerase [48], kinase [80], and methyltransferase [151]. Free energies along the reaction coordinates can be determined by free energy perturbation (FEP) calculations with the harmonic approximation [42, 43]. The effect of enzyme dynamics can be taken into account by using the ensemble of enzyme-substrate complex structures sampled from a MD simulation as initial structures for QM/MM calculations [46, 151, 152].

The QM/MM approach divides the whole enzyme-substrate system into a QM and a MM subsystem. The active site of the enzyme was described by a QM hamiltonian and the influence of the remainders of the protein and the solvent was included via a coupled MM potential. The code combining the modified Gaussian 98 [92] and Tinker 3.6 [56] was utilized for all the calculations. With the reaction coordinate driving (RCD) method, an efficient iterative restrained optimization procedure [42] was repeatedly applied to all the chosen points along the reaction coordinate, resulting in a minimum energy path. For each identified stationary point, the large MM subsystem was relaxed with the truncated Newton method in Cartesian coordinates, while the small QM subsystem was treated using the quasi-Newton minimizer at the B3LYP/6-31G*

level in redundant internal coordinates; and the corresponding vibrational frequencies were determined. The contribution of the QM subsystem fluctuation to free energy change was then calculated with the obtained frequencies using a harmonic approximation. Finally, the free energy changes associated with QM/MM interactions along the reaction path were determined by FEP calculations. In FEP calculations, sampling of the MM subsystem was carried out with the QM subsystem frozen at different states along the reaction path. The total free energy difference between any two points A and B along the reaction coordinate was obtained by adding up the contributions of the QM subsystem energy difference $\Delta E_{qm}(A \rightarrow B)$, the QM fluctuation to the free energy difference $\Delta F_{qm}^{fluc}(A \rightarrow B)$ and the free energy change associated with the QM/MM interaction $\Delta F_{qm/mm}(A \rightarrow B)$ [42, 151].

For the QM/MM calculations on the [W-T$^+$] and [W-T^0] models, the QM subsystem consists of the side chain of Ser-TFK$^+$ (or Ser-TFK^0), and HIP447 (both N_ε and N_δ are protonated) and Glu334, resulting in a total of 57 QM atoms. The boundary between the QM and MM subsystems was treated using the pseudobond approach [41]. All other atoms are described by the classical MM force fields. Similarly to the ACh-mAChE acylation QM/MM calculation [45, 46], the reaction coordinate was chosen to be $d_{C-O} + d_{N-H} - d_{O-H}$ that represents simultaneous bond breaking of carbonyl-C in Ser-TFK$^+$ (or Ser-TFK^0) and seryl O_γ, and a bond forming between Ser203 and His447, as illustrated in Fig. I.24. The noncovalent Michaelis complex, which is denoted as $[W \cdot T^+]$ or $[W \cdot T^0]$, was obtained by running a reverse reaction starting from the corresponding [W-T$^+$] or [W-T^0].

Since our interest was the acylation reaction mechanism, only those atoms within 20.0 Å of the hydroxyl oxygen atom of Ser203 were allowed to move. No cutoff for nonbonded interactions was used in the QM/MM calculations. Throughout the calculations, the pseudobond was treated with the 6-31G* basis set and its corresponding effective core potential parameters [41]. AMBER 95 all-atom force field [51] and the TIP3P model for water [153] were used. In QM/MM-FE calculations, the time step used was 2 fs, and bond lengths involving hydrogen atoms were constrained. A twin-range cutoff method was used to treat nonbonded interactions, with a long-range cutoff of 12 Å, a short-range cutoff of 8 Å, and the nonbonded pair list updated every 20 steps. The temperature was maintained at 300 K using the weak coupling method with a coupling time of 0.1 ps. Each FEP calculation consisted of 50 ps of equilibration and 200 ps of sampling. The final relative free energies were taken as the average of the "forward" and

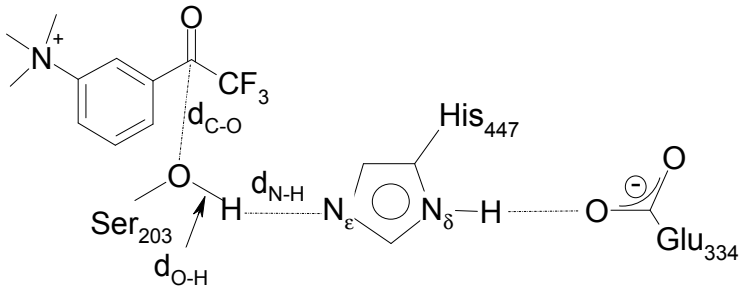

Figure I.24: Illustration of the reaction coordinate $d_{C-O} + d_{N-H} - d_{O-H}$ selected for the reverse reaction of TFK^+ (or TFK^0) binding.

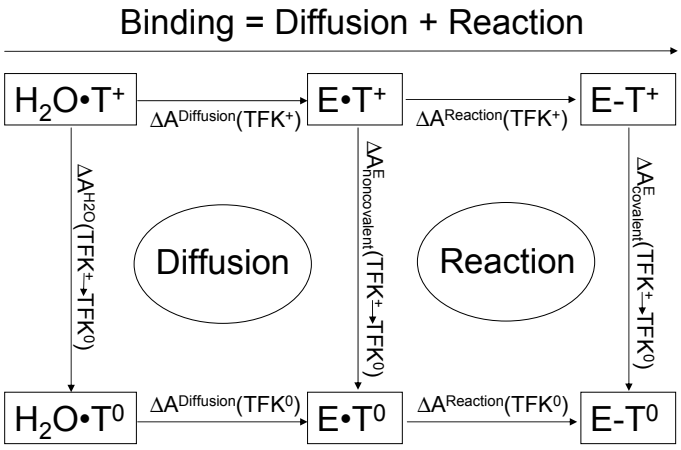

Figure I.25: The thermodynamic cycle of TFK^+ and TFK^0 bindings in the mAChE. Here $[E \cdot T^+]$ and $[E \cdot T^0]$ refer to the noncovalent enzyme-ligand complexes, while $[E-T^+]$ and $[E-T^0]$ refer to the covalent complexes. "E" can represent either "W"(wild-type mAChE) or "M"(H447I mutant mAChE).

"backward" perturbation results.

Thermodynamic Integration

To compare the binding free energy difference of TFK^+ and TFK^0 in the mAChE enzyme, we designed the "alchemical" thermodynamic cycle shown in Fig. I.25.

By Hess's law, we have:

$$\Delta\Delta A^{Diffusion/Reaction}_{TFK^+\rightarrow TFK^0} = \Delta A^{Diffusion/Reaction}_{TFK^0} - \Delta A^{Diffusion/Reaction}_{TFK^+}$$
$$= \begin{cases} \Delta A^{E,noncovalent}_{TFK^+\rightarrow TFK^0} - \Delta A^{H_2O}_{TFK^+\rightarrow TFK^0} & Diffusion \\ \Delta A^{E,covalent}_{TFK^+\rightarrow TFK^0} - \Delta A^{E,noncovalent}_{TFK^+\rightarrow TFK^0} & Reaction \end{cases} \quad (2)$$

The potential energy of the system is expressed as a function of a coupling parameter λ that describes the transformation from TFK^+ to TFK^0; i.e.:

$$U(r,\lambda) = U_0(r) + \lambda U_{TFK^0}(r) + (1-\lambda)U_{TFK^+}(r) \quad (3)$$

with λ = 0 corresponding to a system with TFK^+, and λ = 1 corresponding to a system with TFK^0. $U_{TFK^0}(r)$ is the Hamiltonian of TFK^0, $U_{TFK^+}(r)$ the Hamiltonian of TFK^+ and $U_0(r)$ the Hamiltonian of the remainder of the system.

Then the free energy difference between λ = 0 (TFK^+) and λ = 1 (TFK^0) is:

$$\Delta A_{\lambda=0\rightarrow 1} = \int_0^1 \langle \frac{\partial U(r,\lambda)}{\partial \lambda} \rangle_\lambda d\lambda \approx \sum_{i=1}^{n} w_i \langle \partial U(r,\lambda)/\partial\lambda \rangle_{\lambda_i} \quad (4)$$

The TI calculations were performed by using the AMBER 8.0 package. Two thermodynamic cycles are calculated, one corresponding to the diffusion stage and the other corresponding to the reaction stage. For each calculation, a set of 12 λ values were used with λ = 0.00922, 0.04794, 0.11505, 0.20634, 0.31608, 0.43738, 0.56262, 0.68392, 0.79366, 0.88495, 0.95206, 0.99078 respectively. For each λ, the system was equilibrated for 40 ps at 300 K and data were collected for the subsequent 100 ps. The convergence of the simulation was monitored by checking the forward and backward calculations.

I.C.4 Results and Discussions

Wild-type mAChE complexes

Fig.I.26 illustrates the calculated QM/MM potential energy paths for both TFK^+ and TFK^0 binding to the wild-type mAChE. Both binding processes are spontaneous, and there appears no apparent energy barrier associated with the nucleophilic attack of Ser203-O_γ at the

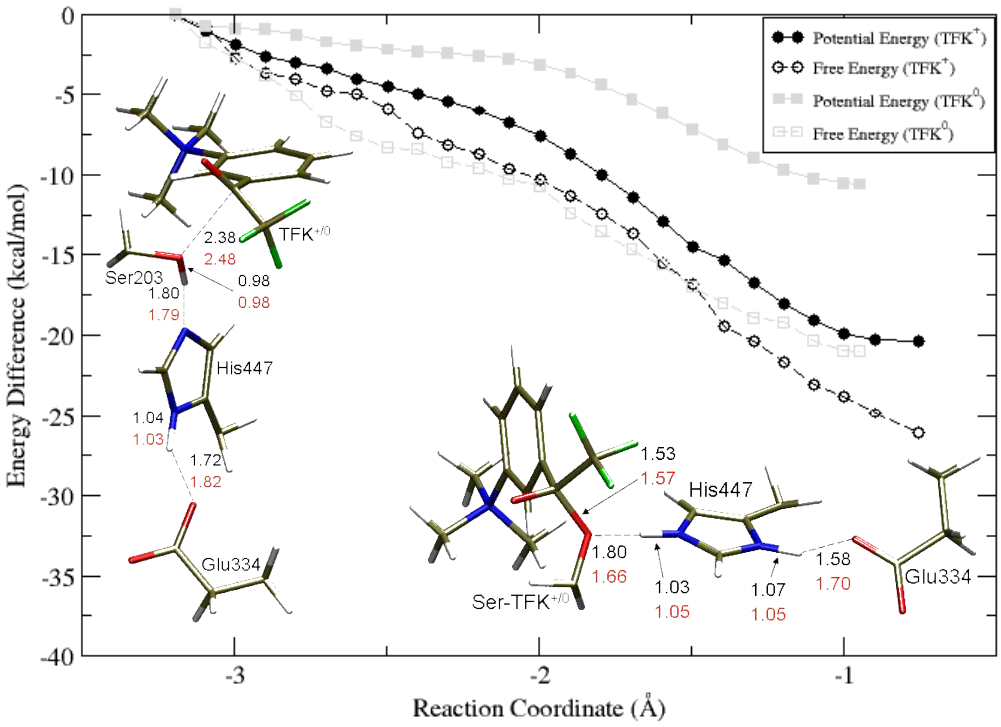

Figure I.26: Determined minimum-energy paths and corresponding free energy changes along the reaction coordinate for the TFK^+ and TFK^0 binding to the wild type mAChE. From left to right, the reaction proceeds from the reactant to the tetrahedral product without an activation barrier. The values in black and red denote the bond lengths of the TFK^+ and TFK^0 cases, respectively.

carbonyl-C of the ligand. The potential energy at the B3LYP(6-31G*) QM/MM level monotonically drops ∼19.3 kcal/mol during the covalent bond forming between Ser203-O_γ and the carbonyl-C of TFK^+, while only a 10.6 kcal/mol decrease is observed between mAChE and TFK^0. To estimate the free energy change of the acylation reaction, we carried out QM/MM-FE perturbation study on both reactions of TFK^+ and TFK^0 with mAChE; results are shown in Fig. I.26. The free energy differences between the reactant and product are 26.1 and 21.0 kcal/mol for TFK^+ and TFK^0, respectively, indicating that the covalent rearrangements associated with the binding of both inhibitors are favorable.

Additionally, two thermodynamic cycles as shown in Fig.I.25 were designed to compare the binding affinity difference of TFK^+ and TFK^0 in the same mAChE target. As shown

Table I.8: The calculated TFK^+ and TFK^0 binding free energies through thermodynamic integration. The unit is kcal/mol.

	ΔA^{H_2O}	$\Delta A^{E}_{noncovalent}$	$\Delta A^{E}_{covalent}$	$\Delta\Delta A^{Diffusion}$	$\Delta\Delta A^{Reaction}$
wild-type	37.9	48.4	58.1	10.5	9.7
H447I mutant	37.9	45.7	66.6*	7.8	20.9*
Δ(H447I - wild)	0.0	-2.7	8.5	**-2.7**	**11.2**

* Suppose the TFK^0/H447I complex exists.

in Table I.8, it turns out that the free energy differences between TFK^+ and TFK^0 are 10.5 kcal/mol at the diffusion stage (forming an initial noncovalent complex) and 9.7 kcal/mol at the reaction stage (forming a covalent complex). Since the reaction is spontaneous withoutany barrier, the diffusion stage is rate-determined. Our result at the diffusion stage is qualitatively consistent with experimental measurements that the ratio of k_{on} and k_{off} with TFK^+ is $\sim$4 order larger than that of TFK^0 [1, 2], while the reaction free energy differences of 9.7 kcal/mol derived from the thermodynamic integration is in good agreement with that from QM/MM calculations. The detailed calculations were shown in the "Supporting Information"[3].

The complex of H447I mutant and TFK^+

As mentioned in Methods section, 7 non-covalent complex $[M \cdot T^+]$ models of the H447I mutant and TFK^+ were obtained via docking and QM/MM calculations. During the subsequent MD simulations of these models, in 6 of 7 models, a water molecule was observed to diffuse into the center of the triangle formed by Ser203, Ser229 and Glu334 in the first 2 *ns* simulations; a representative snapshot from the simulation is shown in Fig. I.27. Then we extended our MD simulations to 10 *ns* for each model. The average distance of the hydroxyl oxygen O_γ of Ser203 to the oxygen O_w of the water is 2.72$\pm$0.12 $\AA$, the carboxyl oxygen of the Ser229 backbone to O_w of the water is 2.78$\pm$0.18 $\AA$, and O_w of the water to one of carboxyl oxygens $O_{\delta 1}$ of Glu334 is 2.66$\pm$0.12 $\AA$ in all of the 10 ns trajectories. Generally, an effective hydrogen bond can be characterized by the short distance between the heteroatoms (less than

[3] http://pubs.acs.org/subscribe/journals/jacsat/suppinfo/ja070601r/ja070601rsi20070326_025016.pdf

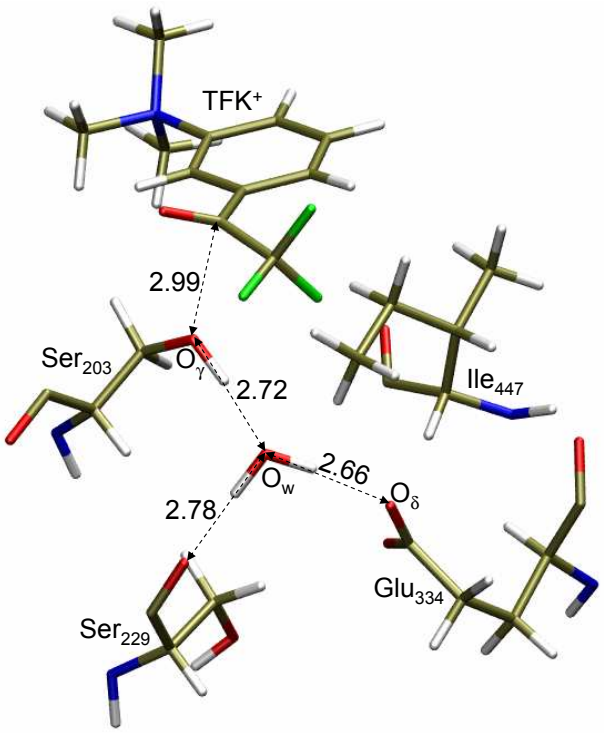

Figure I.27: The "water" triad in the active site of the six $[M \cdot T^{+}]$ models. The values of the distances in $\AA$ are averaged among six models.

3.50 $\AA$), and the bond angle greater than 135° [154, 155, 148]. Using this criteria, the hydrogen bond between the Ser203 O_γ and O_w is found in all the structures in the 10 ns simulations, while the hydrogen bond between O_w and $O_{\delta 1}$ is $\sim$ 99%, and between O_w and Ser229-O is $\sim$ 95%. The water molecule is observed to flip between Ser229-O and $O_{\delta 1}$, while the hydrogen bond between O_γ and O_w stays stable.

Three snapshots from the above MD simulations were selected to explore the acylation reaction mechanism in the H447I mutant. The water molecules beyond a 27 $\AA$ solvent water sphere, centered on the active site (the hydroxyl oxygen O_γ of Ser203) were removed. The three prepared QM/MM models have 10059 atoms (562 water molecules), 10176 atoms (602 water

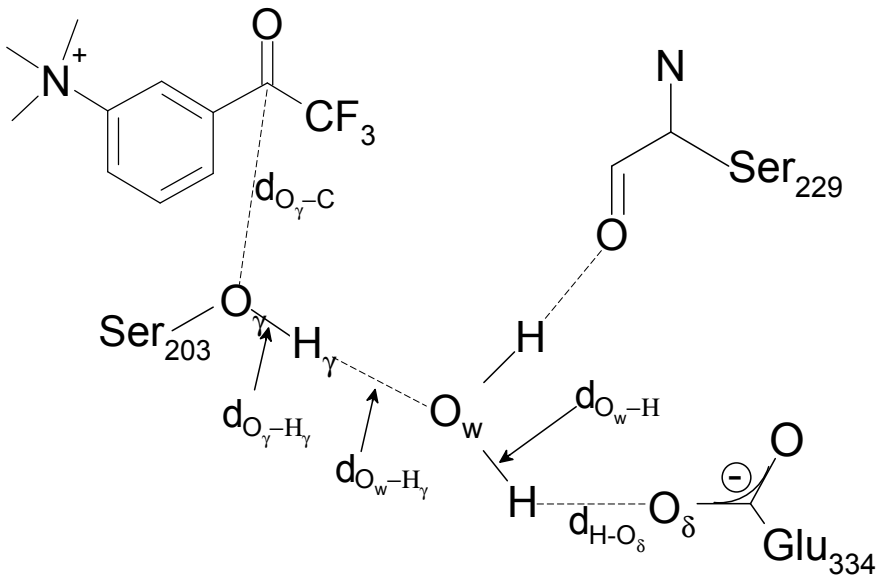

Figure I.28: Illustration of the reaction coordinate used for the H447I mutant and TFK^+ reaction, which is $d_{O_\gamma - H_\gamma} + d_{O_w - H} - d_{O_\gamma - C} - d_{O_w - H_\gamma} - d_{H - O_\delta}$.

molecules) and 10170 atoms (600 water molecules) respectively. Each snapshot was first relaxed by the MM method, and then optimized with B3LYP(6-31G*) QM/MM calculations using an iterative minimization approach [42], leading to an optimized structure for the reactant. The QM subsystem consists of the sidechains of Ser203 and Glu334, the water bridge and TFK^+, with the broken $C_\beta - C_\alpha$ bonds of Ser203 and Glu334 treated as two pseudobonds [41], resulting in a total of 48 QM atoms. All other atoms are treated by MM. The reaction coordinate (RC) is shown in Fig. I.28. Both forward and backward RC driving calculations yield consistent curves and all the reaction paths are smooth and continuous.

All the three QM/MM calculations led to very consistent results, in which the water molecule between Ser203 and Glu334 plays a "charge-relay" role during TFK^+ binding reaction with the H447I mutant. Table I.9 presents the relative potential energies in the reactant (non-covalent complex), transition state and product (covalent complex), respectively. The calculated

Table I.9: The calculated QM/MM potential energy differences (kcal/mol) for three QM/MM models. The geometries are relaxed at the B3LYP(6-31G*)/MM level, and then single-point calculations are performed at three different levels.

	MP2(6-31+G*)/MM	B3LYP(6-31+G*)/MM	B3LYP(6-31G*)/MM
		The first snapshot	
Reactant	0.0	0.0	0.0
Transition State	8.2	7.4	8.2
Intermediate	-5.0	-1.1	2.0
		The second snapshot	
Reactant	0.0	0.0	0.0
Transition State	4.2	5.8	7.5
Intermediate	-8.0	-2.5	0.0
		The third snapshot	
Reactant	0.0	0.0	0.0
Transition State	10.6	10.3	10.4
Product	0.4	3.8	4.4

potential energy barriers at the MP2(6-31+G*)/MM level are 8.2, 4.2, 10.6 kcal/mol. Several key geometry elements in the reactant, transition state and product are shown in Fig. I.29 and also listed in Table I.10. In spite of several variations in the three initial setups, the active site structures of the transition state and product are quite similar in the three calculations.

To estimate the free energy change of the acylation reaction in H447I mutant, we carried out QM/MM-FE perturbation study on all the three snapshots. Fig. I.30 depicts one of three free energy pathways, along with the corresponding potential energy path. The dynamic fluctuations of MM residues contribute at least 2 kcal/mol to the decrease of the reaction barrier.

In order to quantitatively assess the role of the individual residues in the TFK^+ binding reaction, we also calculated the Van der Waals and electrostatic interactions between each MM residue and QM subsystem for both the transition state and reactant. The structures were taken from our B3LYP(6-31G*)/MM calculations and the partial charges were determined by the single-point calculations for the transition state and reactant structures, respectively. The energy

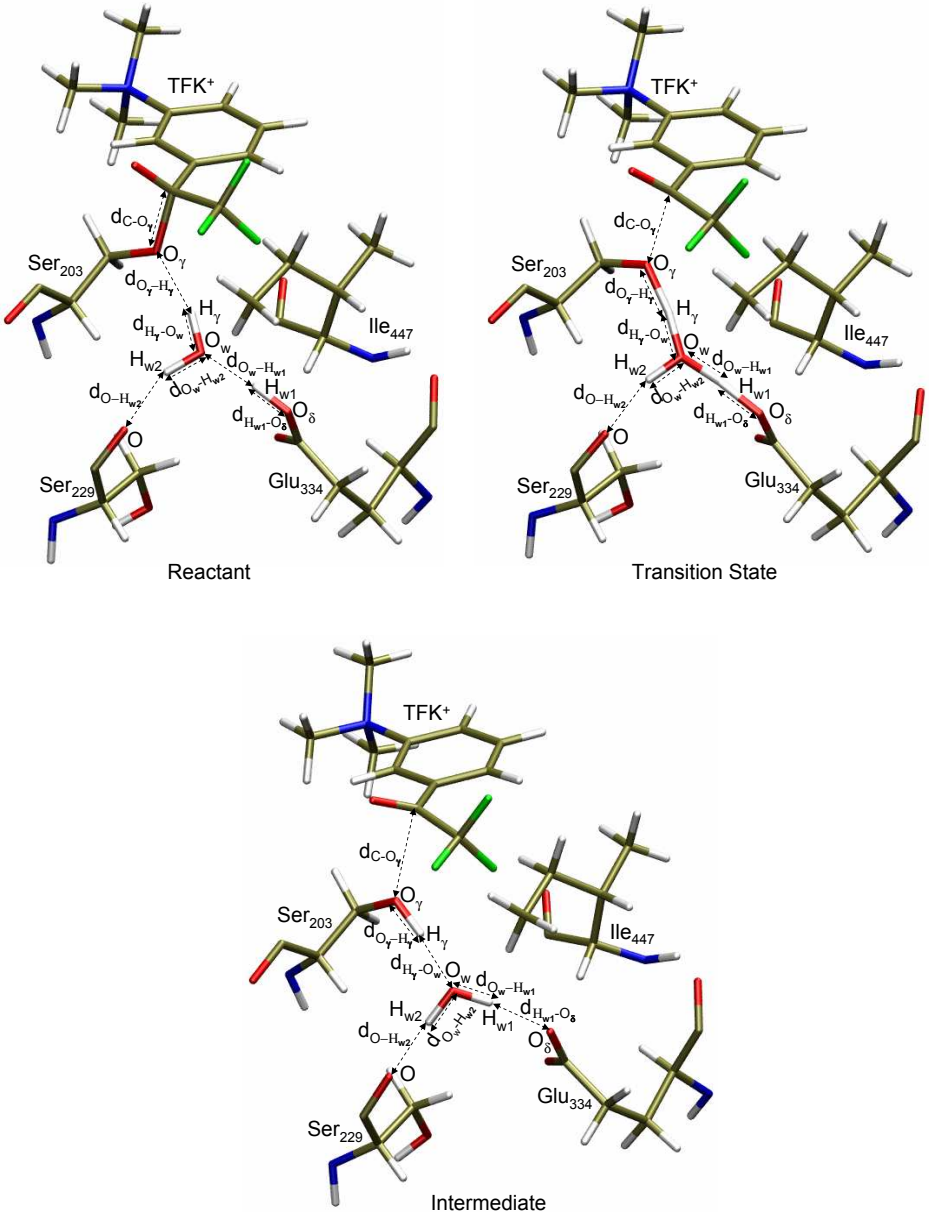

Figure I.29: The active sites of the reactant, transition state and product in QM/MM calculations for the complex of H447I mutant and TFK^+.

Table I.10: Key bond lengths in the reaction centers of the reactant, transition state and product in the QM/MM calculations of $[M \cdot T^{+}]$ models.

	d_{C-O_γ}	$d_{O_\gamma-H_\gamma}$	$d_{H_\gamma-O_w}$	$d_{O_w-H_{w1}}$	$d_{H_{w1}-O_\delta}$	$d_{O_w-H_{w2}}$	$d_{O-H_{w2}}$
The first snapshot							
Reactant	2.48	1.01	1.65	0.98	1.71	0.98	1.71
Transition State	2.03	1.29	1.16	1.17	1.27	0.98	1.75
Product	1.60	1.81	0.99	1.66	1.01	0.98	1.80
The second snapshot							
Reactant	2.72	1.01	1.67	1.01	1.63	0.98	1.89
Transition State	1.92	1.28	1.16	1.12	1.32	0.98	2.18
Product	1.58	1.79	0.99	1.66	1.02	0.98	2.29
The third snapshot							
Reactant	2.58	1.01	1.63	1.01	1.64	0.97	1.83
Transition State	2.00	1.29	1.15	1.19	1.24	0.98	1.90
Product	1.64	1.69	0.99	1.58	1.02	0.98	1.91

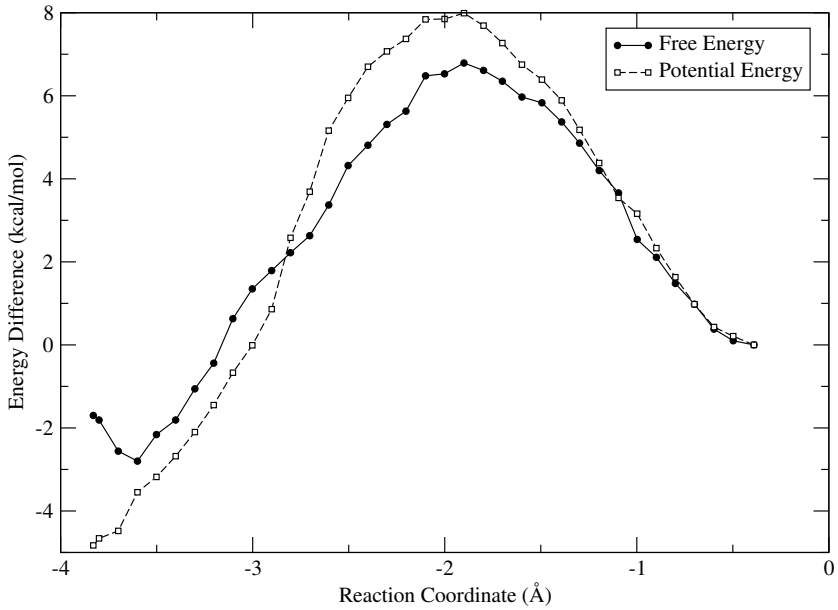

Figure I.30: The free energy and potential energy paths of the acylation reaction along the reaction coordinate in one of the three $[M \cdot T^+]$ models.

difference between the transition state and reactant is taken as the individual barrier contribution of each MM residue. All the main contributors and their average contributions are listed in Table I.11.

In accord with experimental findings, our calculations show that the oxyanion hole (Gly121, Gly122, Ala204) plays an important role in stabilizing the transition state. The reactivities of both G121A and G122A mutants toward TFK^+ were 2,000-11,000-fold lower than that of the wild type AChE [156]. G121A only affected the turnover number, and mutation of Gly122 also had an effect on the Michaelis constant [156] for substrate acetylthiocholine hydrolysis. In our 10 ns MD simulations, only the backbone nitrogens of Gly122 and Ala204 form stable hydrogen bonds with the carbonyl oxygen of TFK^+, which might help to optimize the substrate orientation to participate in the acylation reaction. The total stabilization energy contributed by the oxyanion hole is around 7.0 kcal/mol. In addition, Gly120 in the H447I mutant seems to destabilize the transition state, which is different from what is seen in the wild type AChE [45]. In all the three QM/MM calculations, Glu202 occupies the similar position as that in the wild type, and contributes around 3-7 kcal/mol destabilization to the transition state, consistent with

Table I.11: The individual residue contributions to the transition state stabilization or destabilization for three H447I mutant snapshots (calculation based on MP2(6-31+G*)/MM calculations). $E_{ele+vdw}$ refers to the total nonbonded interaction energy including electrostatic and vdW parts. Energy units are in kcal/mol.

	$E_{ele+vdw}$		
	The first snapshot	The second snapshot	The third snapshot
Asp74	1.3	1.2	2.1
Gly120	1.7	2.1	5.7
Gly121	-1.9	-8.3	-1.9
Gly122	-1.9	-2.6	-2.5
Glu202	6.1	3.0	3.7
Ala204	-2.2	-3.5	-2.5
Glu285	1.7	1.4	1.4
Lys332	2.4	1.9	2.2
Asp333	-3.1	-2.2	-2.9
Asp396	-2.1	-1.7	-2.0
Asp404	-3.2	-2.3	-2.2
Glu431	-1.6	-1.2	-1.7
Ile447	2.8	1.6	3.5
Gly448	2.1	1.8	3.9
Glu450	-2.0	-2.0	-2.1
Arg525	2.2	1.7	1.8

previous theoretical results [45]. In our MD simulations, Glu202 is found to play an important role in maintaining the overall structure of the active center. A hydrogen-bond networked cluster of polar residues, including Tyr133, Glu202, Glu450, Ser229 and two water molecules (one is between Tyr133 and Glu202, and the other is between Glu450 and Glu202) are lined on one side of the catalytic triad. Although Ser229 does not directly participate in bond breaking and forming, it plays an essential role in maintaining the integrity of the active site at both the wild-type and H447I mutant mAChEs. The enzyme loses its activity without Ser229 [157]. Finally, it must be noted that the hydrophobic Ile447 is not directly involved in the bond breaking and forming, but contributes 3 to 4 kcal/mol destabilization energy to the transition state.

The complex of H447I mutant and TFK^0

As mentioned in the Methods section, a total of 8 $[M \cdot T^0]$ complex models were obtained through three different approaches. The resulting 8 models were then subjected to 10 ns MD simulations. Unlike in the $[M \cdot T^+]$ models, none of these $[M \cdot T^0]$ models formed a stable "water triad" during the simulations. Even when the simulation started from a model based on $[M \cdot T^+]$ (the 3rd approach for generating $[M \cdot T^0]$ model as outlined in the Methods section), in which the "water triad" has been formed, the water inside the Ser203, Ser229 and Glu334 departed in less than 1 ns MD simulation. Fig. I.31 displays the positions of several key active site residues during one of the MD simulations. In all these simulations, the hydrogen bond between Ser203 and the water was either disrupted after the first 2 ns simulation or never formed. Therefore, in the $[M \cdot T^0]$ models, we failed to find any stable catalytic base that can accept a proton from Ser203 during the acylation reaction, which is consistent with experimental observations that TFK^0 shows no activity in the H447I mutant. Additionally, QM/MM calculation with the initial structure of $[M \cdot T^0]$ directly modified from $[M \cdot T^+]$ failed to reach a convergence during optimization. All these facts indicate that the positive charge of the ligand TFK^+ plays an essential role in forming an appropriate active center conformation for the H447I mutant binding reaction. The positive charge might help to stabilize the negatively charged residues Glu202, Glu334 as well as the oxyanion hole, which might have H-bonding with Ser203 and Ser229. Once the catalytic water diffuses into the center of the catalytic triangle, the triangle is "locked" and keeps very stable. However, the "lock" can be broken easily or even never formed if TFK^+ is replaced by TFK^0 as show in Fig. I.31. As compared to TFK^+, larger RMSDs for TFK^0

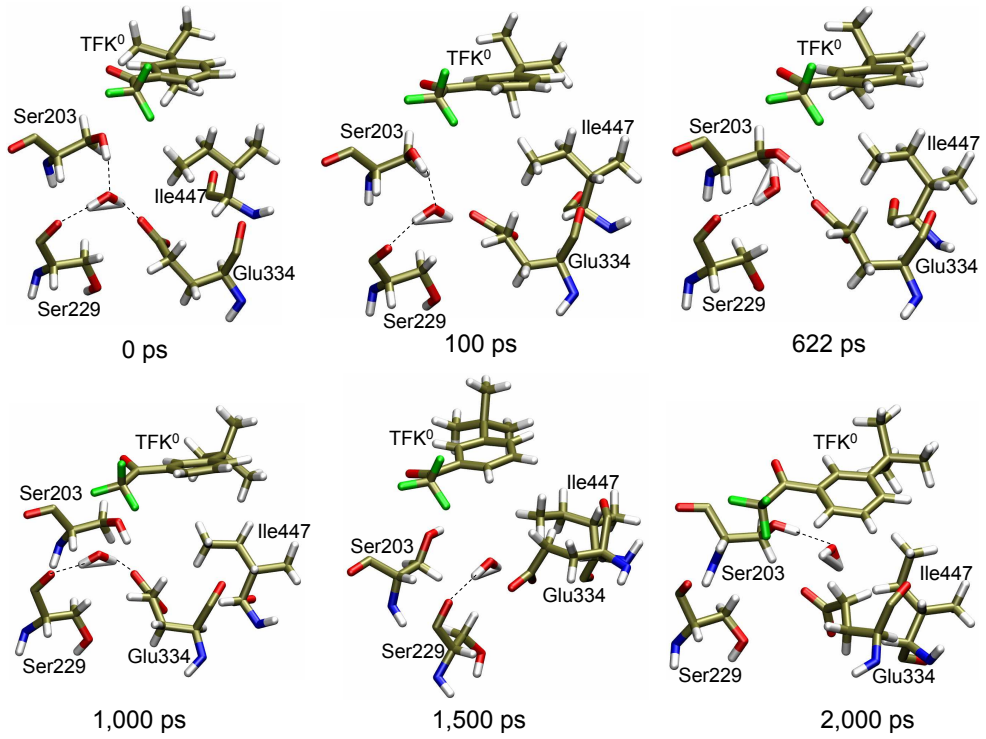

Figure I.31: Several key residue elements in the active center of the complex of H447I mutant and TFK^0 during one of MD simulations.

have been captured in MD simulations.

Furthermore, our TI calculation also confirms that thermodynamically the TFK^+/H447I complex is much more favored than the TFK^0/H447I. As shown in Table I.8, suppose we have TFK^0/H447I complex, the free energy difference of TFK^0 relative to TFK^+ is 20.9 kcal/mol when forming the covalent complex with the H447I mutant (reaction stage) which is overwhelmingly larger than the difference of 7.8 kcal/mol during the diffusion stage. Therefore, thermodynamically speaking, the binding of TFK^0 to the H447I mutant is much less favored, too. In addition, comparing the free energies during the diffusion and reaction stages between the wild type and H447I mutant (see Table 1), the substantially larger difference during the reaction stage further confirms our QM/MM results.

I.C.5 Conclusions

The present calculations suggest a new reaction mechanism for two inhibitors TFK^+ and TFK^0 binding to the H447I mutant mAChE, and provide a compelling explanation for the observed different binding behaviors for TFK^+ and TFK^0 in both the wild-type and the H447I mutant mAChEs.

First, our QM/MM calculations of TFK^+ and TFK^0 in wild-type mAChE demonstrate that the bindings of TFK^+ and TFK^0 are spontaneous. The binding of TFK^+ to mAChE contributes $\sim$27 kcal/mol stabilization to the resulting complex structure, while the binding of TFK^0 causes a nearly 20 kcal/mol energy decrease. These results are consistent with experimental binding affinities of a related series of TMTFA inhibitors.[145]

Second, multiple MD simulations of the $[M-T^+]$ complex consistently show that a water molecule resides in the position originally occupied by His447 in the wild-type mAChE. This water molecule is found to form three stable hydrogen bonds with Ser203, Glu334 and Ser229, respectively. The QM/MM calculations further demonstrate that this water molecule directly participates in the TFK^+ acylation reaction with the enzyme where it acts as a charge relayer - accepting one hydroxyl proton from Ser203 while simultaneously passing one of its protons to the carboxylate of Glu334. However, in the wild-type mAChE, no water was observed to occupy similar positions, therefore, it is unlikely for the wild-type mAChE to adopt such a "charge-relay" reaction mechanism.

Third, multiple MD simulations started from different $[M\cdot T^0]$ models all demonstrate that a stable Ser203, Ser229 and Glu334 triad with a water molecule inside can not be obtained. No other residue near Ser203 can act as a catalytic base to abstract a hydroxyl proton from Ser203 during the acylation reaction, which explains why TFK^0 is inactive in the H447I mutant.

Finally, we investigated and compared the binding affinities of TFK^+ and TFK^0 in the mAChE using TI calculations. Our result confirms that the complexes $[M\cdot T^+]$ and $[M-T^+]$ are much more stable thermodynamically than the corresponding TFK^0 complexes. And these findings corroborate the above QM/MM calculations and experimental observations.

In conclusion, we explored the TFK^+ and TFK^0 inhibition mechanisms in both the wild-type and H447I mutant mAChEs. Despite the replacement of the catalytic base His447, TFK^+ still demonstrates high binding affinity to the H447I mutant. Our computational studies suggest that a water molecule might act as a "charge relayer" and facilitate the binding of the

ligand to the enzyme while this is not true for the binding of the neutral analogue TFK^0. We hope that these results will stimulate further experimental studies.

I.C.6 Acknowledgments

Y.H.C. thanks Prof. Palmer Taylor for helpful discussions and experimental data, and Prof. Yingkai Zhang for advice and access of his QM/MM code and his brilliant idea in simulating enzymatic reactions. This work has been supported in part by grants from the NSF and NIH. Additional support has been provided by NBCR, CTBP, HHMI, the W. M. Keck Foundation, and Accelrys, Inc.

Chapter I contains material from "How Does the cAMP-Dependent Protein Kinase Catalyze the Phosphorylation Reaction: an *ab initio* QM/MM Study" published in 2005 in *J. Am. Chem. Soc.* (Volumn 127, pages 1553-1562), authored by Yuhui Cheng, Yingkai Zhang, and J. Andrew McCammon;" How does activation loop phosphorylation modulate catalytic activity in the cAMP-dependent protein kinase: A Theoretical Study" published in 2006 in *Protein Science* (Volumn 15, pages 672-683), authored by Yuhui Cheng, Yingkai Zhang, and J. Andrew McCammon; "Acetylcholinesterase: Mechanisms of Covalent Inhibition of Wild-type and H447I Mutant Determined by Computational Analyses" published in 2007 in *J. Am. Chem. Soc.* (Volumn 129, pages 6562-6570), authored by Yuhui Cheng, Xiaolin Cheng, Zoran Radić, and J. Andrew McCammon.

II

Time-Dependent Smoluchowski Solver

II.A Finite Element Analysis of the Time-Dependent Smoluchowski Equation for Acetylcholinesterase Reaction Rate Calculations

II.A.1 Abstract

This article describes the numerical solution of the time-dependent Smoluchowski equation to study diffusion in biomolecular systems. Specifically, finite element methods have been developed to calculate ligand binding rate constants for large biomolecules. The resulting software has been validated and applied to the mouse acetylcholinesterase monomer and several tetramers. Rates for inhibitor binding to mAChE were calculated at various ionic strengths with several different time steps. Calculated rates show very good agreement with experimental and theoretical steady-state studies. Furthermore, these finite element methods require significantly fewer computational resources than existing particle-based Brownian dynamics methods and are robust for complicated geometries. The key finding of biological importance is that the rate accelerations of the monomeric and tetrameric mAChE that result from electrostatic steering are preserved under the non-steady-state conditions that are expected to occur in physiological circumstances.

II.A.2 Introduction

Diffusion plays an important role in a variety of biomolecular processes, which have been studied extensively using various biophysical, biochemical and computational methods.

Computational models of diffusion have been widely studied using both discrete [158, 159, 160, 161, 162] and continuum methods [163, 164, 165, 166, 167, 11]. The discrete methods concentrate on the stochastic processes based on individual particles, which include Monte Carlo[168, 169, 170, 162], Brownian dynamics (BD)[171, 172, 173] and Langevin dynamics[174, 175] simulations. Continuum modeling describes the diffusional processes via concentration distribution probability in lieu of stochastic dynamics of individual particles. Comparing with the discrete methods, continuum approaches needn't deal with the individual Brownian particles and the computionational cost can be substantially less than for the discrete methods.

In previous work with continuum methods, Song et al. have presented finite element methods for solving the Steady-State Smoluchowski equation (SSSE), which describes the steady-state behavior of diffusion-limited ligand binding[166, 167]. These methods have been shown to be significantly more efficient than traditional Brownian dynamics (BD)approaches for evaluating reaction rate constants for diffusion-limited binding of simple ligands. Recently, Zhang et al. applied this approach for studies of several conformations of tetrameric mouse acetylcholinesterase (mAChE)[176]. However, the SSSE solution only provides the answer at the time independent stage of diffusion. In other words, we only obtain the concentration distribution and rate constant when diffusion and reaction between the ligand and the enzyme reach the steady state. Physiological conditions, however, can be expected to include nonsteady-state kinetics. One possible way to study the diffusion dynamics on biomolecular interface binding energy landscape is mean first passage time (MFPT), which was introduced recently by Wang et al. [177]. The theory suggests a way of connecting the models/simulations with single molecule experiments by analyzing the kinetic trajectories. However, it is still an open question for the diffusional problem in a large spatial and time scale.

In the present work, we apply adaptive finite element methods to solve the time-dependent Smoluchowski equation (TDSE), using *a posteriori* error estimation to iteratively refine the finite element meshes. The binding of charged and non-charged ligands to mAChEs has been described at each timestep. The diffusion results have been compared with those from steady-state Smoluchowski diffusion studies and experimental results. AChE is a serine esterase that terminates the activity of acetylcholine (ACh) within cholinergic synapses by hydrolysis of the ACh ester bond to produce acetate and choline [178]. Hydrolysis of ACh occurs in the active site of AChE, which lies at the base of a 20 $\AA$-deep gorge within the enzyme. The rate-limiting

step of ACh hydrolysis by AChE is the diffusional encounter [120, 179, 122], making the system a popular target for both experimental [180, 1, 181] and computational diffusion studies [182, 183].

II.A.3 Theory and Modeling Details

Our time-dependent SMOL solver (http://mccammon.ucsd.edu/smol/index.html) models the diffusion of ligands relative to a target molecule, subject to a potential obtained by solving the Poisson-Boltzmann equation. It is perhaps most easily explained by initially considering motion of an ensemble of Brownian particles in a prescribed external potential $W(\vec{R})$($\vec{R}$ being a particle's position) under conditions of high friction, where the Smoluchowski equation applies.

Boundaries and Initialization of the Time-Dependent Smoluchowski Equation

The starting point for development of the time-dependent SMOL solver is the steady-state SMOL solver described by Song et al. [166, 167]. The original Smoluchowski equation has the form of a continuity equation:

$$\frac{\partial p(\vec{R};t)}{\partial t} = -\vec{\nabla}\cdot\vec{j}(\vec{R};t) \tag{1}$$

where the particle flux is defined as:

$$\begin{aligned}\vec{j}(\vec{R};t) &= D(\vec{R})[\vec{\nabla}p(\vec{R};t) + \beta\vec{\nabla}W(\vec{R})p(\vec{R};t)] \\ &= D(\vec{R})e^{-\beta W(\vec{R})}\nabla e^{\beta W(\vec{R})}p(\vec{R};t)\end{aligned} \tag{2}$$

Here $p(\vec{R};t)$ is the distribution function of the ensemble of Brownian particles, $D(\vec{R})$ is the diffusion coefficient, $\beta = 1/k_B\mathrm{T}$ is the inverse Boltzmann energy, k_B is the Boltzmann constant, T is the temperature, and $W(\vec{R})$ is the potential of mean force (PMF) for a diffusing particle due to solvent mediated interactions with the target molecule. For simplicity, $D(\vec{R})$ can be assumed to be constant. The two terms contributing to the flux have clear physical meanings. The first is due to free diffusional processes, as quantified by Fick's first law. The second contribution is due to the drift velocity - $\vec{\nabla}W(\vec{R})\gamma$ induced by the systematic forces - $\vec{\nabla}W(\vec{R})$ and friction quantified by the friction constant γ. The relation beteen diffusion coefficient D and friction constant γ is given by Stokes-Einstein equation: $D\beta\gamma = 1$.

The TDSE can be solved to determine biomolecular diffusional encounter rates before steady state is established. Following the work of Song et al.[166, 167] and Zhou et al.[184, 185, 186], the application of the TDSE to this question involves the solution of Eq. 1 in a three-dimensional domain Ω, with the following boundary and initial conditions. A bulk Dirichlet condition is imposed on the outer boundary $\Gamma_b \subset \partial\Omega$,

$$p(\vec{R}_l;t) = p_{bulk}, \quad for \ \ \vec{R}_l \in \Gamma_b, \tag{3}$$

where p_{bulk} denotes the bulk concentration at the outer boundary. A reactive Robin condition is implemented on the active site boundary $\Gamma_a \subset \partial\Omega$,

$$n(\vec{R}_0) \cdot \nabla p(\vec{R}_0;t) = \alpha(\vec{R}_0) p(\vec{R}_0), \quad for \ \ \vec{R}_0 \in \Gamma_a, \tag{4}$$

providing an intrinsic reaction rate $\alpha(\vec{R}_0)$. Here, $n(\vec{R}_0)$ is the surface normal. For the diffusion-limited reaction process, such as ACh hydrolysis by mAChE, the concentration of ACh at the binding site is approximately zero. Therefore, the reactive Robin condition on the inner boundary can be simplified as:

$$p(\vec{R}_0;t) = 0, \quad for \ \ \vec{R}_0 \in \Gamma_a, \tag{5}$$

For the non-reactive surface parts of the inner boundary $\Gamma_r \subset \partial\Omega$, a reflective Neumann condition is employed.

$$n(\vec{R}_0) \cdot jp(\vec{R}_0;t) = 0, \tag{6}$$

Finally, we set up the initial conditions as

$$p(\vec{R};0) = \begin{cases} p_{bulk} & |\vec{R}| = l \\ 0 & |\vec{R}| < l \end{cases} \tag{7}$$

Therefore, the diffusion-determined biomolecular reaction rate constant during the simulation time can be obtained from the flux $\vec{j}(\vec{R};t)$ by integration over the active site boundary, i.e.

$$k(t) = p_{bulk}^{-1} \int_{\Gamma} n(\vec{R}) \cdot \vec{j}(\vec{R};t) dS \tag{8}$$

Finite Element Discrete Formulation

To numerically solve the TDSE, we employed the Galerkin finite element approximation to discretize the differential equation [187]. The original TDSE (eq. 1) can be written as described below [188, 189, 167]:

Let $\Omega \subset \mathbb{R}^3$ be an open set, and let $\partial\Omega$ denote the boundary, which can be thought of as a set in $\mathbb{R}^2$. Consider now the TDSE, a member of the class of elliptic equations:

$$\begin{aligned} -\nabla \cdot (a(\vec{R};t)\nabla u(\vec{R};t)) + \frac{\partial p(\vec{R};t)}{\partial t} &= 0 \ \ in \ \ \Omega, \\ p(\vec{R};t) &= 0 \ \ for \ \ \vec{R} \in \Gamma_a, \\ n(\vec{R}) \cdot p(\vec{R};t) &= 0 \ \ for \ \ \vec{R} \in \Gamma_r, \\ p(\vec{R};t) &= p_{bulk} \ \ for \ \ \vec{R} \in \Gamma_b, \end{aligned} \tag{9}$$

where $a(\vec{R};t) = D(\vec{R})e^{-\beta W(\vec{R})}$ and $u(\vec{R};t) = e^{\beta W(\vec{R})}p(\vec{R};t)$.

According to Holst et al.[190], the solution to the original problem also solves the following problem:

$$Find \ \ u \in \bar{u} + H_0^1(\Omega) \ \ such \ \ that \ \ \ < F(u), v >= 0 \ \ \forall v \in H_0^1(\Omega), \tag{10}$$

where u is the approximate solution found by the numerical method, $\bar{u}$ is a trace function satisfying the Dirichlet boundary conditions and H_0^1 is the test function space [191, 190]. The "weak" bilinear form $< F(u), v >$ is given by:

$$< F(u), v >= \int_\Omega (a\nabla v \cdot \nabla u + \frac{\partial u}{\partial t} v) dx, \tag{11}$$

We have used the fact that a boundary integral vanishes due to the fact that the test function v vanishes on the boundary.

For a discrete solution to eq. 11, taking $span\{\phi_1, \phi_2, ..., \phi_N\} \subset H_0^1(\Omega)$, eq. 11 reduces to a set of N nonlinear algebraic relations (implicitly defined) for N coefficients $\{\alpha_j\}$ in the expansion:

$$u_h = \sum_{j=1}^{N} \alpha_j \phi_j \tag{12}$$

According to the Galerkin approximation, N equals the number of finite element nodes.

Therefore, the corresponding "weak form" of the TDSE is

$$Find\ \ u_h - \bar{u_h} \in H_0^1\ \ such\ \ that\ \ \ < F(u_h), v_i >= 0\ \ \forall v_i \in H_0^1, \tag{13}$$

To obtain an unconditionally stable solution, two implicit algorithms have been implemented in our codes: Crank-Nicolson and backward Euler's methods.

Finally, the concentration distribution can be obtained by $p(\vec{R};t) = e^{-\beta W(\vec{R})} u(\vec{R};t)$.

a posteriori Error Estimation and Mesh Refinement

As decribed by Holst et al. [190], the adaptive mesh refinement procedure follows a "solve-estimate-refine" algorithm and has been implemented in the FEtk software (http://www.fetk.org/). Because of the inefficiency to "estimate" and "refine" in each time step, we only estimated and refined the mesh while solving the SSSE. With the refined mesh, TDSE diffusion studies were implemented. In the "estimate" step, we introduced the a posteriori error estimator η_s below holding for a Galerkin approximation u_h satisfying

$$\|u - u_h\|_{H^1(\Omega)} \leq C_0 \{\sum_{s \in S} \eta_s^2\}^{1/2} \tag{14}$$

where C_0 is a constant and the element-wise error indicator η_s is defined as:

$$\eta_s = \{{h_s}^2 \|\nabla \cdot (a \nabla u_h)\|_{L^2(s)}^2 + \frac{1}{2} \sum_{f \in s} \|[n_f \cdot (a \nabla u_h)]_f\|_{L^2(f)}^2\}^{1/2}. \tag{15}$$

where h_s and h_f represent the diameter of the simplex s and the face f, respectively. $f \in s$ denotes a face of simplex, $[v]_f$ denotes the jump across the face of function v and the Lesbegue norm

$$\|\nabla \cdot (a \nabla u_h(r))\| = De^{-\beta W(r)} \|\nabla \cdot \nabla u_h(r) - \beta \nabla W \cdot \nabla u_h(r)\| \tag{16}$$

The entire "solve-estimate-refine" cycle is repeated until the global error $\sqrt{\sum_s \eta_s^2}$ is reduced to an acceptable user-defined level.

Potential of Mean Force (PMF) Input

Currently we provide two options to map the PMF to each finite element node in the time-dependent SMOL solver code. First, it can input the PMF obtained by boundary element

methods (BEM) [192, 193]. The PMF corresponds to the electrostatic potential obtained by solving the Poisson-Boltzmann equation. Second, APBS 0.4.0 (http://sourceforge.net/projects/apbs) is used to calculate the PMF, which is the potential field W(r) in Eq. 2 [189]. The partial charges and radii of each atom in the mAChE monomer and tetramer molecules have been assigned using the CHARMM22 force field, and the dielectric constant is set as 4.0 inside the protein and 78.0 for the solvent. The solvent probe radius is set as 1.4 $\AA$, and the ion exclusion layer is set as 2.0 $\AA$. Ionic strengths varying between 0 and 0.67 M were used in the PMF calculations and following diffusion studies.

To allow the potential to approach zero at the outer boundary, a large space of 40 times the radius of the biomolecule is required. A series of nested potential grids is constructed in a multiresolution format where higher resolution meshes provide PMF values near the molecular surface while coarser meshes are used away from the molecule. The dimensions of the finest grid are given by the psize.py utility in the APBS software package, and the coarsest grid dimensions are set to cover the whole problem domain plus two grid spacings (to allow gradient calculation) in each dimension. The setup for the rest of the grid hierarchy is calculated using a geometric sequence for grid spacing. For mAChE monomer, the finest grid has dimensions of $86.3\AA\times76.4\AA\times101.4\AA$ with 161, 129 and 193 grid points in each direction, respectively. This corresponds to a $0.5\AA\times0.6\AA\times0.5\AA$ grid spacing setup. The coarsest grid has dimensions of $3400\AA\times3000\AA\times4300\AA$ with 161 grid points in each direction. The corresponding grid spacing settings are $21.1\AA\times18.6\AA\times26.7\AA$.

Adaptive Finite Element Mesh Generation

For the mAChE monomer case, similarly with previous studies [166, 167], we used a mouse AChE (mAChE) structure adapted from the crystal structure of the mAChE-fasciculin II complex (1MAH) [180] and perturbed by Tara and co-workers via molecular dynamics simulations with an ACh-like ligand in the active site gorge [183] to produce gorge conformations with wider widths than the original X-ray structure. The diffusing ligand was modeled as a sphere with an exclusion radius of 2.0 $\AA$ and a diffusion constant of $7.8\times10^4\AA^2/\mu s$. This perturbation was necessary for computational diffusion simulations with a fixed biomolecular structure. Reactive boundaries were defined using the biomolecular surface, which is exactly the same with that used in Song et al. [167].

For the mAChE tetramer cases, we used three structures: a loose, pseudosquare planar tetramer with antiparallel alignment of the two four-helix bundles and a large space in the center (PDB: 1C2B); a compact, square nonplanar tetramer with parallel arrangement of the four-helix bundles that may expose all the four t peptide sequences on a single side (PDB: 1C2O); and in addition to the crystal structures, an intermediate structure (INT) was generated by morphing the two crystal structures using the morph script in visual molecular dynamics [194]. Reactive boundary definitions are exactly the same with the above mAChE monomer case.

The tetrahedral meshes were obtained and refined from the inflated van der Waals-based accessibility data for the mAChE monomer and tetramers using the Levelset Boundary Interior Exterior-Mesher[195, 196, 197]. Initially the region between the biomolecule and a slightly larger sphere centered about the molecular center of mass, was discretized by adaptive tetrahedral meshes. It generated very fine triangular elements near the active site gorge, while coarser elements everywhere else. The mesh is then extended to the entire diffusion domain and the inside of the biomolecule with spatial adaptivity in that the mesh element size increases with increasing distance from the biomolecule. The number of tetrahedral elements varies from 50,000 to 70,000 for different tetramer geometries.

II.A.4 Results and discussion

Validation of the Time-Dependent SMOL Code with A Spherical Test Case

Before applying the time-dependent SMOL program to a biomolecular system with complicated geometries, we first tested it with the classic spherical system [198] and compared the calculated result with the known analytical solution. For this test case, we chose a diffusing sphere with a 2 $\AA$ radius and neutral charge. The entire problem domain is a sphere with a 400 $\AA$ radius, which was discretized with 745,472 tetrahedral elements. A detailed view of the surface mesh for the stationary sphere is also shown in Fig. II.1. The time-dependent Smoluchowski equation then becomes the Einstein diffusion equation. The diffusing particle's dimensionless bulk concentration was set to 1. Ignoring hydrodynamic interactions, the diffusion constant D is calculated as $7.8 \times 10^4 \AA^2/\mu s$ using the Stokes-Einstein equation with a hydrodynamic radius of 3.5 $\AA$, solvent viscosity of $0.891 \times 10^{-3} kg/(m \cdot s)$, and 300 K temperature.

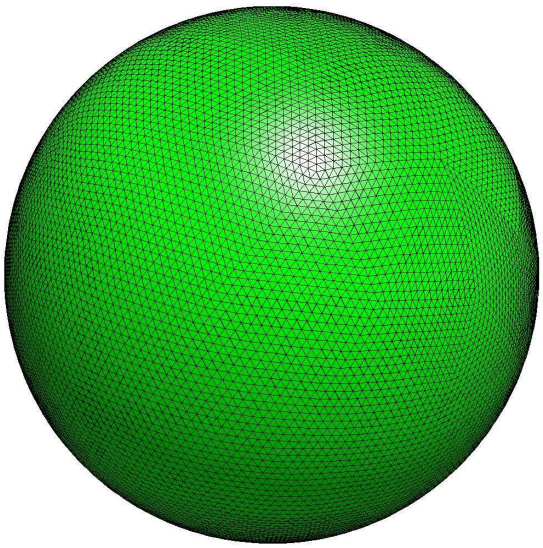

Figure II.1: Illustration of the discretized problem domain for the spherical analytical test. The green represents the outer boundary, in which the ligand concentration is kept as a constant.

Analytical solution For a spherically symmetric system without external potential, the TDSE can be written as

$$\begin{aligned}\frac{\partial p}{\partial t} &= -\frac{1}{r^2}\frac{\partial}{\partial r}(r^2 J p) \\ &= -\frac{1}{r^2}\frac{\partial}{\partial r}(r^2 D\frac{\partial p}{\partial r})\end{aligned}$$

with boundary conditions

$$p(r_0) = p_{bulk}$$

where r_0 is the radius for the outer boundary. The analytical expression for the concentration distribution is

$$p(r;t) = p_{bulk}\{1+\frac{2r_0}{\pi r}\sum_{n=1}^{\infty}\frac{(-1)^n}{n}sin\frac{n\pi r}{r_0}exp[-D(\frac{n\pi}{r_0})^2 t]\}$$

This analytical form of the solution was expressed by the sum of zero-order spherical Bessel functions. Fig. II.2 presents the concentration distributions during the simulation time with our TDSE solver, comparing with the above analytical solution.

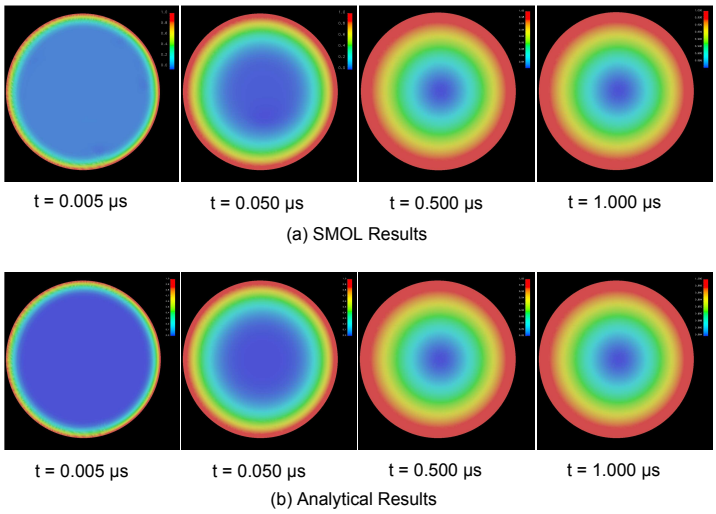

Figure II.2: Time evolution of the 2D concentration distribution contour in the problem domain. (a) our SMOL solution;(b) spherical analytical solution.

SMOL numerical solution According to Fig. II.2, the performance of the SMOL program is good, with almost the same concentration distribution as in the analytical solution. It must be noted that, the analytical solution for the time-dependent diffusion with the Columbic potential cannot be addressed with a simple formula, however, we have implemented our solver to test the same steady-state case addressed in Table 1 of Song et al.[167], and obtained very consistent results.

Application of the TDSE Solver to Mouse Acetylcholinesterase Monomer

One of the major advantages of continuum methods such as the time-dependent SMOL solver is the ability to simulate the complete diffusion dynamics for large biological systems with complicated geometries with significantly lower computational cost than the Brownian dynamics approach. This section demonstrates the implementation of TDSE to study the ligand binding kinetic process of the mAChE monomer under various ionic strength conditions [199].

With the original mesh we measured the diffusion-controlled reaction rates during the simulation time with the timestep at 50 *ps*, as shown in Fig. II.3. Separate calculations were performed at ionic strengths of 0.000, 0.050, 0.100, 0.150, 0.200, 0.250, 0.300, 0.450, 0.600,

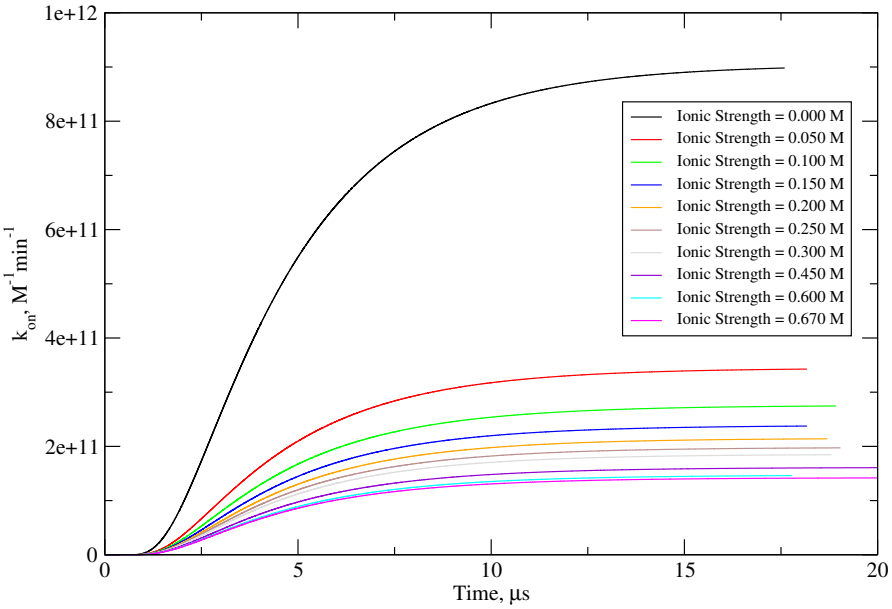

Figure II.3: k_{on}(t) values in time-dependent ACh diffusion under the various ionic strength conditions.

and 0.670 M. At the zero ionic strength, the whole system reaches the steady state in over 15 *ns*. The value of k_{on} at the end of the simulation is $9.535 \times 10^{11} M^{-1} \cdot min^{-1}$, which is very consistent with the experimental value at $(9.80 \pm 0.60) \times 10^{11} M^{-1} \cdot min^{-1}$ [1]. Meanwhile, the k_{on} value for the neutral ligand at the steady state is $9.297 \times 10^{10} M^{-1} \cdot min^{-1}$, which is consistent with the previous steady-state calculations [176]. Table II.1 listed the final k_{on} value derived from the TDSE calculations and the corresponding sets from SSSE calculations [166]. When the ionic strength becomes higher, the time to reach the steady state decreases substantially. Obviously, we have obtained consistent results, comparing with the previous SSSE and BD calculations.

Table II.1: SSSE reaction rate and TDSE final reaction rate constants as a function of ionic strength

ionic strength (M)	0.000	0.025	0.100	0.300	0.600
SSSE results $k_{on}(10^{11} M^{-1} min^{-1})$	9.562	3.681	2.304	1.572	1.302
TDSE final results $k_{on}(10^{11} M^{-1} min^{-1})$	9.535	3.673	2.298	1.569	1.298

Furthermore, our TDSE solver can report all the ligand concentration distribution his-

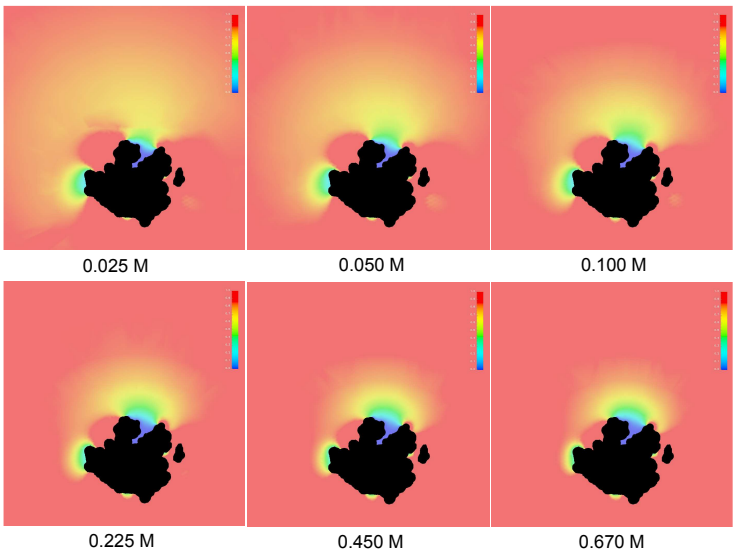

Figure II.4: 2D ligand concentration distribution contour around mAChE at the steady state under various ionic strengths. The red color represents high concentration area, while the blue represents low concentration area.

tories during the 20 μs simulation. In this case, we recorded a concentration distribution every 100 timesteps (5 ns) and a restart checkpoint every 1000 timestep (50 ns). Fig. II.4 demonstrates the 2D concentration distribution around the mAChE molecule at the end of 20 μs simulation. The origin and the normal of the clip plane have been set at (0 16.6$\AA$ 0) and (1 0 1), respectively. k_{on} exhibits an ionic strength dependence strongly indicative of electrostatistic acceleration. The high ionic strength environment lessens the electrostatic interactions between the active site of mAChE and the ligand. Therefore, the relatively low ligand concentration area shrinks while ionic strength increases. Specifically, at 0.150 M ionic strength, several dynamic snapshots have been plotted, as depicted in Fig. II.5. These snapshots demonstrate the whole diffusion process of ACh-like ligands from the area far from the enzyme until they reach the active site and react and disappear.

In this section, we explore the use of the adaptive finite element methods to implement TDSE calculations on the mAChE monomer. The first step is to interactively solve the SSSE based on the a posteriori error estimation [190, 167]. The iterative error-based refinement of the initial 656,823-simplex mesh was performed until the global error is less than a value chosen to provide reaction rates which did not change appreciably upon further refinement. The refined

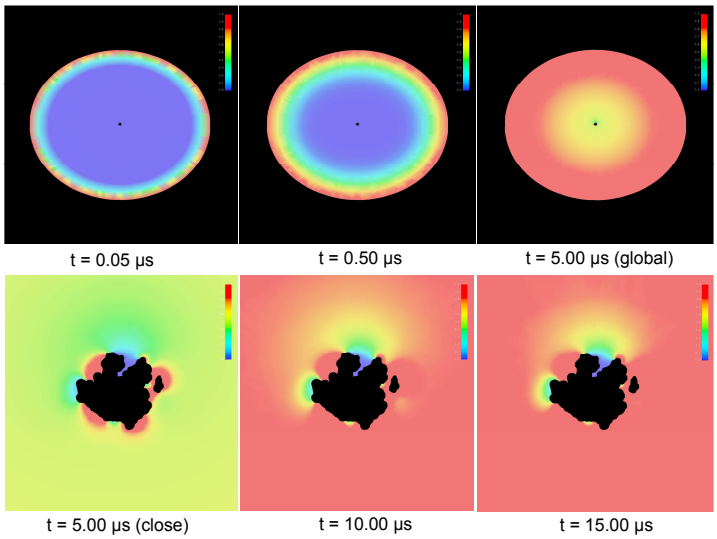

Figure II.5: The time-dependent ligand concentration distribution at 0.150 M ionic strength for the mAChE monomer.

mesh has 824,746 simplices at 150 mM ionic strength. Then, we implemented another TDSE calculations with the refined mesh. Fig. II.6 shows the kinetic curves of both the original and refined mesh. Again, the two calculations are in good overall agreement but do show some differences at the final steady state. Specifically, the refinement of the adaptive meshes shows a little increase of the k_{on} value after reaching the steady state.

Application of the TDSE Solver to mAChE Tetramers

A previous SSSE study described the effect of electrostatic forces on ACh steady-state diffusion to the mouse acetylcholinesterase tetramer [176]. Here, we extend the previous study using the same meshes and potential files with our time-dependent SMOL solver. The time step for the three tetramer models was set at 10 *ns*, and concentration histories were recorded every 100 steps. Two crystal structures (1C2O and 1C2B) and an intermediate structure (INT) are all studied by solving the TDSE. The actual conformational dynamics of the mouse acetylcholinesterase tetramer has been neglected in this work.

Fig. II.7(a) shows the time-dependent rate constant per active site at 0.150 M ionic strength for the above three mouse acetylcholinesterase tetramer structures. It takes more than

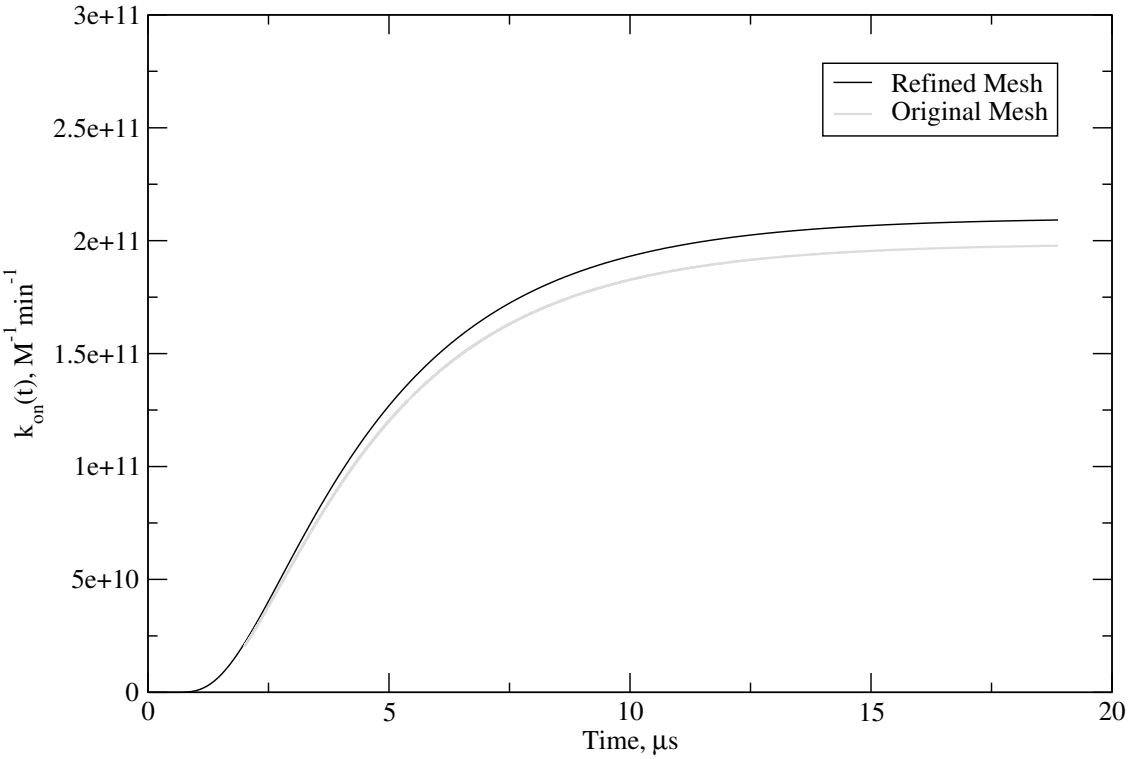

Figure II.6: The comparison of k_{on} values in time-dependent ACh diffusion between the original and refined meshes.

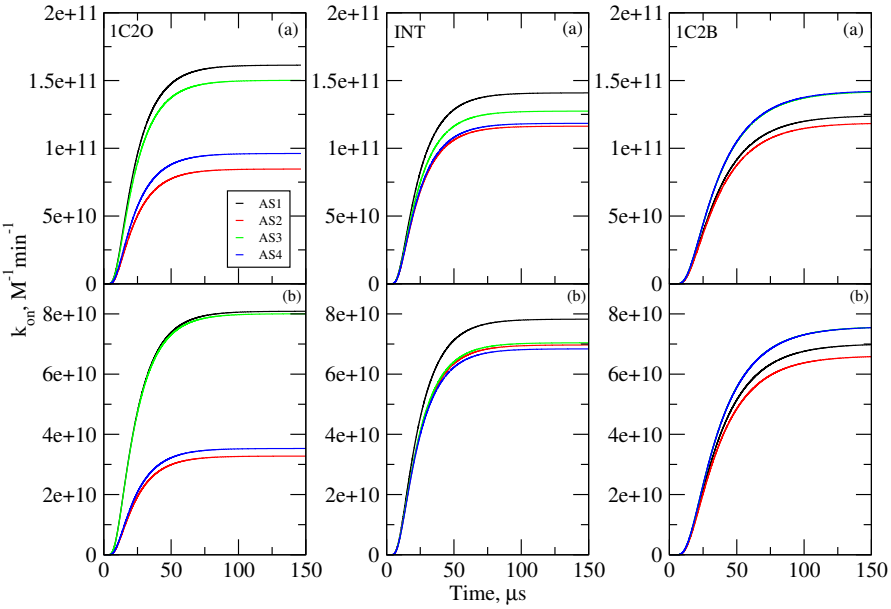

Figure II.7: The dependency of $k_{on}(t)$ values on the simulation time for the structures 1C2O, INT and 1C2B: (a) 0.150 M ionic strength and +1.0*e* ligand;(b) neutral ACh-like ligand.

75 μs for each active site to reach the steady state. For structure 1C2O, the entrances to two of the four active gorges (AS2 and AS4) are partially blocked by another subunit in the complementary dimer, while the other two gorges are completely accessible from outside (AS1 and AS3). As a result, the four kinetic curves in 1C2O can be classified into two subgroups: one subgroup corresponds to active site 1 (AS1) and active site 3 (AS3), in each of which the gorge is open, and at the end of the simulation, the reaction rates are $1.61 \times 10^{11} M^{-1} min^{-1}$ and $1.50 \times 10^{11} M^{-1} min^{-1}$, respectively; another subgroup corresponds to active site 2 (AS2) and active site 4 (AS3), where the gorges are sterically shielded by nearby subunits, and the final reaction rates are $8.47 \times 10^{10} M^{-1} min^{-1}$ and $9.62 \times 10^{10} M^{-1} min^{-1}$, respectively, which is a little more than half of that for AS1 or AS3. Fig. II.7(b) demonstrates the $k_{on}(t)$ values for the neutral ligand. Comparing with the +1.0*e* charged ligand, the neutral ligand still shows similar time-dependent curves for individual active sites, while the $k_{on}(t)$ value is much less than the corresponding +1.0*e* charged case.

Similarly, we tested the final steady-state concentration distribution in the diffusion domain under various ionic strength conditions for the AChE tetramers. For example, Fig. II.8 illustrates the different concentration profiles at 0.025, 0.050, 0.100, 0.300, 0.450, 0.670M ionic

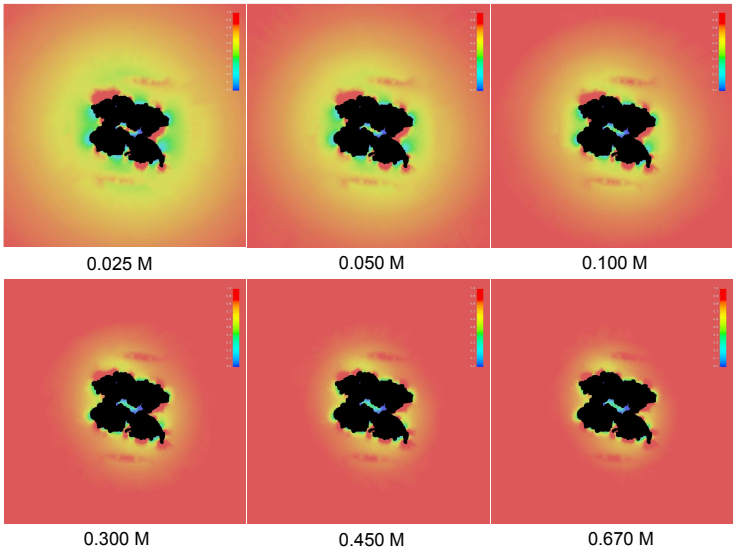

Figure II.8: Steady-state ligand concentration distribution under 6 different ionic strength conditions for structure 1C2O.

strength solutions for structure 1C2O. Comparing with the monomer case, the ACh-like ligand concentration around the 1C2O molecule is much lower when the ionic strength is small, due to the stronger electrostatic attraction between the ligands and the tetramer molecule. While the ionic strength becomes higher, the electrostatic effect on the steady-state concentration distribution turns out to be weaker.

We also obtained the time-dependent rate constant per active site for the structure 1C2B, in which all the four gorges are nearly completely accessible to the solvent (Fig. II.7). The profiles of $k_{on}(t)$ of AS3 and AS4 are almost the same, while the value of the final steady state for AS1 or AS2 is a little smaller, but still above $1.10 \times 10^{11} M^{-1} min^{-1}$. The sum of the four active sites is $5.28 \times 10^{11} M^{-1} min^{-1}$, whereas the total steady-state k_{on} in structure 1C2O is $4.92 \times 10^{11} M^{-1} min^{-1}$. It must be noted that the steady-state k_{on} in the mAChE monomer is $1.97 \times 10^{11} M^{-1} min^{-1}$ at 0.150 M ionic strength. Therefore, the average reaction rate per active site for the tetramer is around 64% that of the monomer, which is close to the result of the previous SSSE studies [176]. The four active sites show similar kinetic profiles, and reach the steady states at nearly the same time. Meanwhile, the time-dependent rate constant per active site in the structure INT appears more like that in the structure 1C2B, although the difference

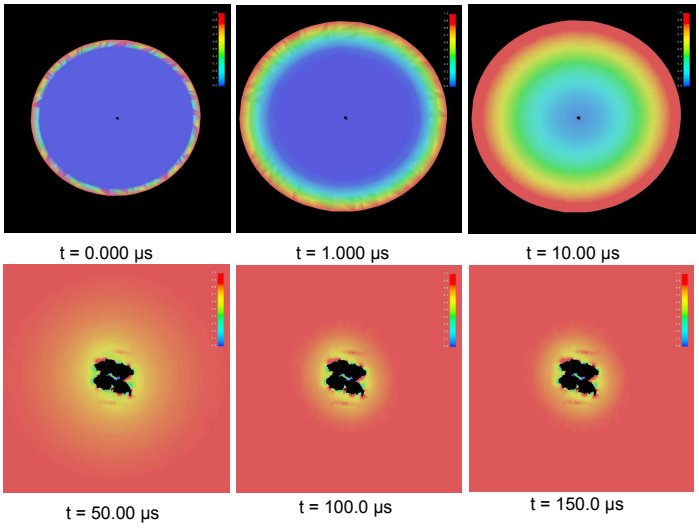

Figure II.9: ligand concentration distribution in the diffusion domain during the simulation time for structure 1C2O.

between AS1 amd AS3 is still similar with that in the structure 1C2O. Additionally, our time-dependent SMOL solver can show the detailed diffusion process. For the 1C2O case, Fig. II.9 describes the ligand concentration distribution in the problem domain. The red represents high concentration areas, while the blue represents the low concentration areas.

Conclusions

In this study, we describe new continuum-based methods for studying diffusion in biomolecular systems. Specifically, we present the time-dependent SMOL software package, a finite element-based set of tools for solving the TDSE to calculate ligand binding rate constants for large biomolecules under pre-steady-state and steady-state conditions. The main improvement from the previous SMOL solver [166, 167] can be addressed as below: first, the new solver has removed the drift term (Eq. 2) which is discontinuous for ∇W, as well as the asymmetry [200]. Theoretically, the new SMOL solver can utilize the conjugate gradient (CG) method which is a direct method for symmetric and positive definite linear systems, while the old solver can only solve SSSE with the Bi-conjugate gradient (BCG) method. Comparing with the new solver, BCG is slower and harder to converge. Therefore, our new SMOL solver can solve both

steady-state and time-dependent problems much more efficiently and stably than the old version.

With the new code, we solved the time-dependent diffusion in the analytical case of a reactive sphere, mAChE monomer and tetramer cases. Comparing with previous steady state studies, our research extends the study into the non-equilibrium diffusion dynamics and obtained very consistent results. Moreover, the calculated rates of the mAChE monomer were compared with experimental data [1] and show very good agreement with experiment while requiring substantially less computational effort than existing particle-based Brownian dynamics methods. Additionally, the value of $k_{on}(t)$ seems to be underestimated with the coarser meshes, which is consistent with previous observations [167]. Similarly, the k_{on} values in mAChE tetramers should increase if we refine the original mesh. In the previous study [176] and this one, we have found the activity of one subunit in a mAChE tetramer equals around $60\% \sim 70\%$ that of a free monomer. With the appropriate meshes, we would expect to obtain an activity closer to that in the free monomer and the catalytic activity might not be too affected by subunit association as suggested in the experiment [201].

Additionally, we describe new adaptive meshing methods developed to discretize biomolecular systems into finite element meshes which respect the geometry of the biomolecule. Although not presented in this study, it is important to note that the new meshing methods could be useful in a variety of biological simulations including computational studies of biomolecular electrophoresis [202], elasticity [46, 196], and electrostatics [189, 203, 204, 188].

Finally, this research lays the groundwork for the integration of molecular-scale information into simulations of cellular-scale systems such as the neuromuscular junction [163, 11, 205]. In particular, this new finite element framework should facilitate the incorporation of other continuum mechanics phenomena into biomolecular simulations. The ultimate goal of this work is to develop scalable methods and theories that will allow researchers to begin to study biological dynamics in a cellular context efficiently and robustly.

II.A.5 Acknowledgements

Y.H.C. thanks David Minh for proofreading, and Ben-Zhuo Lu for helpful discussions. This work has been supported in part by grants from the NSF and NIH. Additional support has been provided by NBCR, CTBP, HHMI, and the W. M. Keck Foundation.

Chapter II is taken from “Finite Element Analysis of the Time-Dependent Smolu-

chowski Equation for Acetylcholinesterase Reaction Rate Calculations" published in 2007 in *Biophys. J.* (Volumn 92, pages 3397-3406), authored by Yuhui Cheng, Jason K. Suen, Deqiang Zhang, Stephen D. Bond, Yongjie Zhang, Yuhua Song, Nathan A. Baker, Chandrajit L. Bajaj, Michael J. Holst, and J. Andrew McCammon.

III

Cellular Diffusion-reaction Dynamics Modeling

III.A Continuum Simulations of Acetylcholine Diffusion with Reaction-determined Boundaries in Neuromuscular Junction Models

III.A.1 Abstract

The reaction-diffusion system of the neuromuscular junction has been modeled in 3D using the finite element package FEtk. The numerical solution of the dynamics of acetylcholine with the detailed reaction processes of acetylcholinesterases and nicotinic acetylcholine receptors has been discussed with the reaction-determined boundary conditions. The simulation results describe the detailed acetylcholine hydrolysis process, and reveal the time-dependent interconversion of the closed and open states of the acetylcholine receptors as well as the percentages of unliganded/monoliganded/diliganded states during the neurotransmission. The finite element method has demonstrated its flexibility and robustness in modeling large biological systems.

III.A.2 Introduction

The nature of neuronal signaling has been a problem of special interest in both biology and neuroscience [206, 207, 208, 209]. During neurotransmission, a neurotransmitter must be released from the terminal bouton of the presynaptic neuron, diffuse cross the synaptic gap, and activate postsynaptic receptors.

The neuromuscular junction (NMJ), the point of communication between neurons and muscle fiber, provides a classic example of synaptic transmission. The terminals of motor axons contain thousands of vesicles filled with acetylcholine (ACh). When an action potential reaches the axon terminal, hundreds of these vesicles discharge their ACh molecules onto a specialized area of postsynaptic membrane on the fiber. This area contains a cluster of transmembrane channels, i.e. the nicotinic acetylcholine receptors (nAChRs), which are opened by the association of ACh; sodium or potassium ions (Na^+ & K^+) can then diffuse through the channels, Na^+ inward and K^+ outward [210, 211, 212, 213, 214].

ACh molecules remain in the cleft between the presynaptic and postsynaptic membranes until they are hydrolyzed by acetylcholinesterase (AChE), the biomolecular off-switch for synaptic transmission. AChE is present as clusters of three tetramers suspended by collagen stalks bound to the muscle membrane at varying densities (600 μm^{-2} to 2500 μm^{-2}) throughout the junctional folds (JFs). Acetylcholinesterase breaks down the ACh in the neuromuscular junction at a maximum speed of $\sim$2000 ACh molecules per second per AChE active site in the case of human enzyme. Therefore, it provides a very efficient mechanism to terminate synaptic transmission for subsequent signaling [215, 216]. Drug molecules such as competitive inhibitors can bind with AChE and regulate the breakdown rate of ACh and affect the subsequent signaling rate and strength.

The receptor nAChR is a ligand-gated sodium channel that opens briefly upon binding ACh. This allows entry of sodium ions into the interior of the muscle cell, which results in partial depolarization of the postsynaptic membrane. If the number of open channels reaches the proper threshold, a self-propagating muscle action potential is generated in the postsynaptic membrane. nAChRs are present in small quantities over most of the muscle membrane surface but are concentrated heavily at the tips of the NMJs.

In adult NMJ, nAChR is a transmembrane pentamer consisting of 5 subunits assembled with a stoichiometry $\alpha_2\beta\gamma\delta$ around an axis of pseudosymmetry perpendicular to the plane of the membrane [217, 214]. One nAChR pentamer has two activation binding sites for ACh: one lies at the interface between one α and the γ subunit while the other is between the second α subunit and the δ subunit [217, 214]. The binding of ACh molecules to the binding sites induces the ion channel to open. Spontaneous opening of a single vesicle causes generation of the miniature endplate current (mEPC).

Simulations of partial differential equation (PDE) based synapse models have provided a great deal of insight into several aspects of synaptic transmission [218, 219, 220, 221, 222, 223, 224, 225]. However, these models assumed the synapse to be two dimensional only and employed relatively out-of-date kinetic models for ACh hydrolysis and state changes of nAChR. These limitations are largely due to the complexity of solving three dimensional (3D) PDEs with complex boundary conditions [226, 227, 228, 229, 230]. Recently, solutions of 3D PDEs in synaptic transmission models became possible with the advance of finite element methods [231, 191, 163, 11]. However, simple AChE reaction models have been used, and the nAChRs were not treated explicitly. On the other hand, stochastic or Monte Carlo (MC) based models such as that embedded in the MCell software enables 3D NMJ simulations with realistic kinetic models for ACh hydrolysis and binding and dissociation [162, 232, 233]. In this paper, we report a complementary approach to the MC model to describe the behavior of a NMJ based on a 3D PDE with recent kinetic models for ACh hydrolysis and the various nAChR conformational changes initiated by ACh binding. Competitive inhibitors of AChE can also be integrated with the AChE reaction model. Our approach allows coupling of the detailed chemical reactions with the physical diffusion processes taking place during synaptic transmission. We can model many more physiological phenomena in the ACh diffusion, such as substrate and competitive inhibition, and the conformational variations of nAChR. In addition, simulation of surface dynamics at the postsynaptic membrane could be incorporated. Therefore, our approach shall enable pharmacokinetics and pharmacodynamics analysis of rationally designed drugs involving synaptic transmission. Implementation of the numerical algorithm for simulating the NMJ model was performed using FEtk and the Manifold Code [190].

III.A.3 Model setup and mathematical background

The AChE model

The kinetic model for ACh hydrolysis is built based on a mechanism proposed by Radić et al. [234, 235, 2] (Fig. III.1 (d)). This model incorporates the effect of substrate inhibition and therefore enables an accurate representation of the reaction over a large range of ACh concentrations. In Fig. III.1 (d), E and S represent AChE and ACh respectively. S combines at two discrete sites, forming two binary complexes, ES (ACh in the active site) and

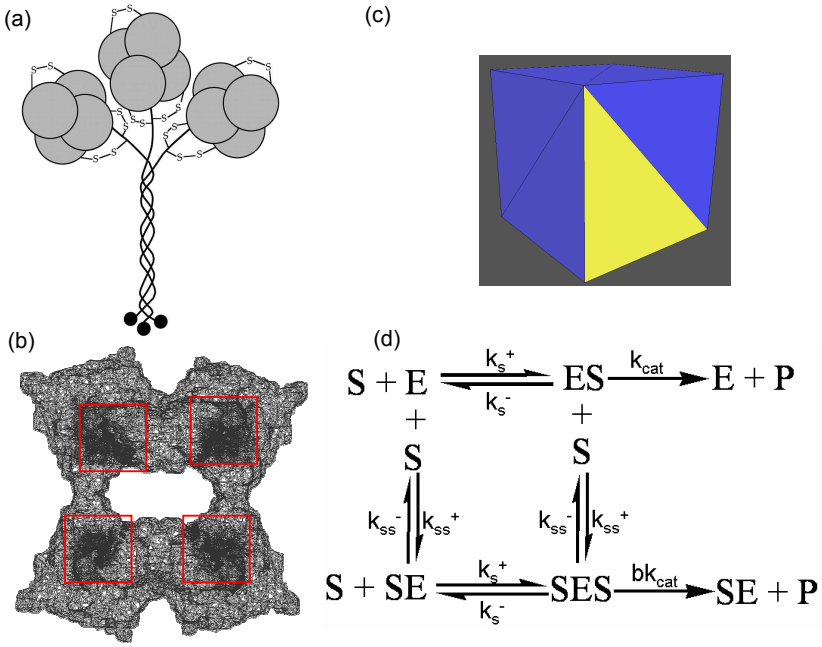

Figure III.1: (a) A cluster of three AChE tetrameters suspended by collagen stalks bound to the muscle membrane; (b) An AChE tetramer with four active sites exposed; (c) The AChE cluster representing Fig. 1(a), the blue surface denotes the nonreactive Neumann boundary, while yellow corresponds to the reactive Robin boundary; (d) The AChE kinetic scheme. S represents ACh, while ES and SE represent the binary complexes with ACh in the active site and peripheral site, respectively.

SE (ACh in the peripheral site [234, 236]), only one of which, ES, results in substrate hydrolysis. The following values of the kinetic parameters were used in this study: $k_s^+ = k_{ss}^+ = 10^9 M^{-1}s^{-1}$, $k_s^- = 4.6 \times 10^4 s^{-1}$, $k_{ss}^- = 1.5 \times 10^7 s^{-1}$, $k_{cat} = 1.4 \times 10^5 min^{-1}$, and b = 0.23.

Assuming AChEs are fixed in space, the conservation equations for describing the various states of AChE with a given ACh concentration on the surface are:

$$\frac{d\theta_1}{dt} = k_s^+ p(x,t)(1-\sum_{i=1}^{3}\theta_i) + k_{ss}^- \theta_3 - (k_s^- + k_{ss}^+ p(x,t) + k_{cat})\theta_1$$

$$\frac{d\theta_2}{dt} = k_{ss}^+ p(x,t)(1-\sum_{i=1}^{3}\theta_i) + k_s^- \theta_3 - (k_s^+ p(x,t) + k_{ss}^-)\theta_2$$

$$\frac{d\theta_3}{dt} = k_s^+ p(x,t)\theta_2 + k_{ss}^+ p(x,t)\theta_1 - (k_s^- + k_{ss}^- + bk_{cat})\theta_3 \quad (1)$$

Here, θ_1, θ_2, θ_3 and $1-\sum_{i=1}^{3}\theta_i$ denote the normalized concentrations of ES, SE, SES and E, respectively, relative to the total concentration of AChE involved intermediates and products, $[AChE]_{total}$; p(x,t) represents ACh concentration in the position "x" at time "t". Solution procedure for the above ordinary differential equations (ODEs) is outlined in the "Supplementary Material"[1].

In addition to the reaction mechanism, an important attribute in modeling NMJ is the representation of the AChE structure in space. As in our previous effort of using rectilinear AChE model[163, 11], we represent an AChE cluster including 3 AChE tetramers using a cubic box with 1/8 of the surface considered to be active. In terms of the PDE model for ACh diffusion, the active boundary is implemented by a Robin boundary (radiation or essential boundary) with θ_1, θ_2 and θ_3 calculated from Eq. 1, while other parts of the AChE cluster are represented by the Neumann boundary (reflecting boundary) (Fig. III.1 (c)).

The binding level of ACh to AChE that gives rise to a specific intermediate is monitored by the integral of the total fraction of that given intermediate on the reactive surfaces of AChE, L_i(t),

$$L_i(t) = \int_{\partial\Omega_{AChE}^{act}} \theta_i(t)dS \quad (2)$$

Here $\partial\Omega_{AChE}^{act}$ is the surface of the active site of AChE. With i = 1, 2, 3, we are able to observe general timescale trends of all AChE intermediates.

[1] http://www.sciencedirect.com/science/MiamiMultiMediaURL/B6TFB-4MVN14T-1/B6TFB-4MVN14T-1-X/5222/503c91579d03fcf4f319a01b00490000/applic1.pdf

The nAChR model

The nAChR is a heteropentameric trans-membrane protein that protrudes into the synaptic and intracellular compartments, with a five-fold axis of quasi-symmetry perpendicular to the membrane. Measured from the separations of the Cys-loop disulfide bonds, the average protomer-protomer separation (the distance between two nearby subunit centers) is around 29 $\AA$ [237]. The side length of the extracellular domains including the ligand-binding region and the interface is around 70 $\AA$ [212].

Experimental studies on nAChR have shown several conformations under physiological conditions. At least three different conformations have been differentiated: the closed state (C), the open state (O) and the desensitized state (D). These conformations can interconvert with one another. Among the different nAChR conformations, the desensitized state is still elusive experimentally. Therefore to illustrate the feasibility of our approach, this work focuses on using a simple nAChR gating process, based on the experimental reaction scheme suggested by Land et al. [238]. With ACh occupying the binding sites, the closed $\rightleftharpoons$ open reaction ("gating") of the diliganded nAChR is much more favorable ($\Theta = \beta/\alpha \cong 28$) than that of unliganded receptor ($\Theta \cong 10^{-7} - 10^{-6}$) [239]. Here, α and β are the rate constants for opening and closing, respectively. The affinity of the nAChR for ACh is circa 12,000-fold higher in the open than in the closed conformation. Based on the kinetic measurements, the reaction mechanism corresponding to different conformation states of nAChR are shown in Fig. III.2 (b).

The conservation equations of all the different conformations of nAChR in Fig. III.2 (b), with a given concentration of ACh on the active surface of nAChR are,

$$\begin{aligned}
\frac{d\phi_1}{dt} &= 2k_+ p(x,t)(1 - \sum_{i=1}^{3} \phi_i) + 2k_- \phi_2 - (k_- + k_+ p(x,t))\phi_1 \\
\frac{d\phi_2}{dt} &= k_+ p(x,t)\phi_1 + \beta\phi_3 - (2k_- + \alpha)\phi_2 \\
\frac{d\phi_3}{dt} &= \alpha\phi_2 - \beta\phi_3
\end{aligned} \tag{3}$$

Where ϕ_1, ϕ_2 and ϕ_3 represent the fractions of the monoliganded receptors [AR^{1or2}], and the diliganded receptors [C] and [O] relative to the total concentration of nAChR, i.e. we define $[R_{total}] = [AR^{1or2}] + [C] + [O] + [R^0]$, $\phi_1 = [AR^{1or2}]/[R_{total}]$, $\phi_2 = [C]/[R_{total}]$ and $\phi_3 = [O]/[R_{total}]$, Therefore, $[R^0] = 1 - \sum_{i=1}^{3} \phi_i$.

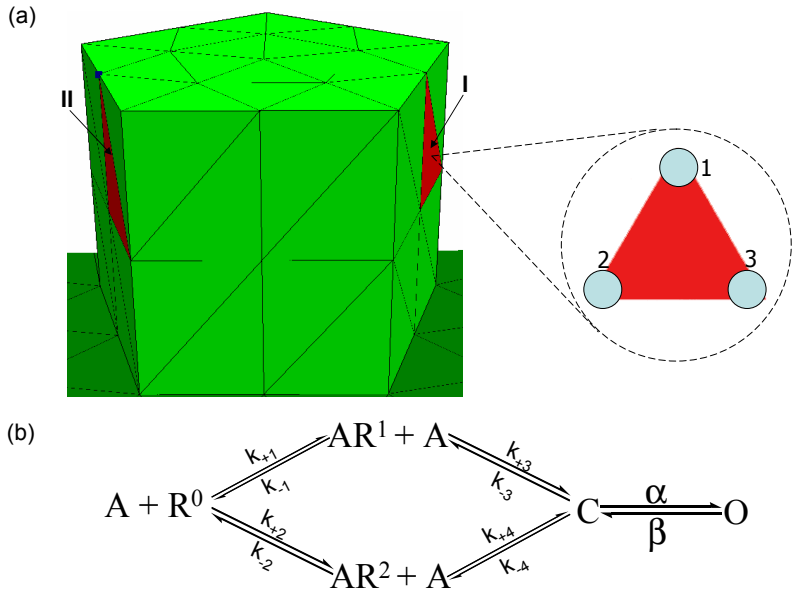

Figure III.2: (a) View of the finite element mesh of the nAChR and part of the external box. Two red triangles represent two ACh binding sites and are assigned the reactive boundary, and all other green triangles belong to non-active sites and are assigned the neumann boundary; (b) The nAChR kinetic scheme. R^0 denotes the unliganded nAChR, AR^1 or AR^2 denotes the monoliganded nAChR; C and O represent diliganded closed and open states.

The corresponding kinetic parameters [238, 240, 241] for our simulation are:

$$
\begin{aligned}
&k_+ = k_{+1} = k_{+2} = k_{+3} = k_{+4} = 3.0 \times 10^7 M^{-1} s^{-1};\\
&k_- = k_{-1} = k_{-2} = k_{-3} = k_{-4} = 1.0 \times 10^4 s^{-1};\\
&\alpha = 2.0 \times 10^4 s^{-1};\\
&\beta = 5.0 \times 10^3 s^{-1};
\end{aligned} \tag{4}
$$

The detailed solution to the above equations is similar to that for the AChE kinetic equations.

To represent the complex morphology of nAChR pentamers, we modeled each nAChR pentamer as pentagonal prism and placed the pentamer at the bottom of a large cubic box (Fig. III.2). Specifically, the length of the edge of the top or bottom pentagons is 5.84 *n*m and the length of the side of the pentagonal prism is 7.0 *n*m. All the pentagonal prisms were placed at the base of a cubic box with 0.50 μm edges (Fig.III.3). For each nAChR pentagonal prism, mixed boundary conditions were employed. The active-site boundaries $\partial\Omega^{act}_{nAChR}$ were distributed on two sides of the pentagonal prism, of which only 1/8 of each side is defined as the active site, i.e. the ACh-binding site. When coupled with the ACh diffusion dynamics, the boundary condition at the active sites of nAChR were assumed to be Robin boundary conditions with ϕ_i evaluated using Eq. 3, whereas the remaining surface of nAChR was modeled as Neumann boundary conditions.

To model large quantities of nAChRs, the pentameric nAChR is currently too expensive for computation. Therefore, we consider a tetrahedral nAChR instead of a pentameric nAChR. Two faces of each tetrahedron are labeled as ACh binding sites. The total surface area of the tetrahedron is determined by matching the correlation of the ion-channel maximum open probabilities with ACh concentration using the pentameric nAChR (Fig. III.4). The surface area of the tetrahedron is found to be around 1.2×10^{-4} μm^2.

Weak formulation of the time-dependent diffusion equations

In this section, we present the weak formulations of the time-dependent diffusion equations for use in the finite element calculations [242, 243].

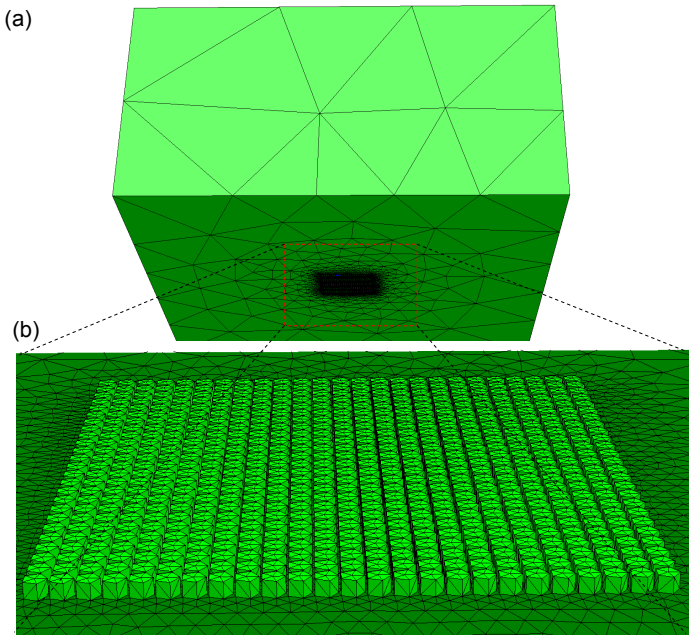

Figure III.3: Two views of the finite element mesh for the nAChR model. (a) the outside of the model, with the 625 nAChRs integrated at the bottom of the rectangular box. (b) a close up view of the bottom surface with the nAChR pentamers.

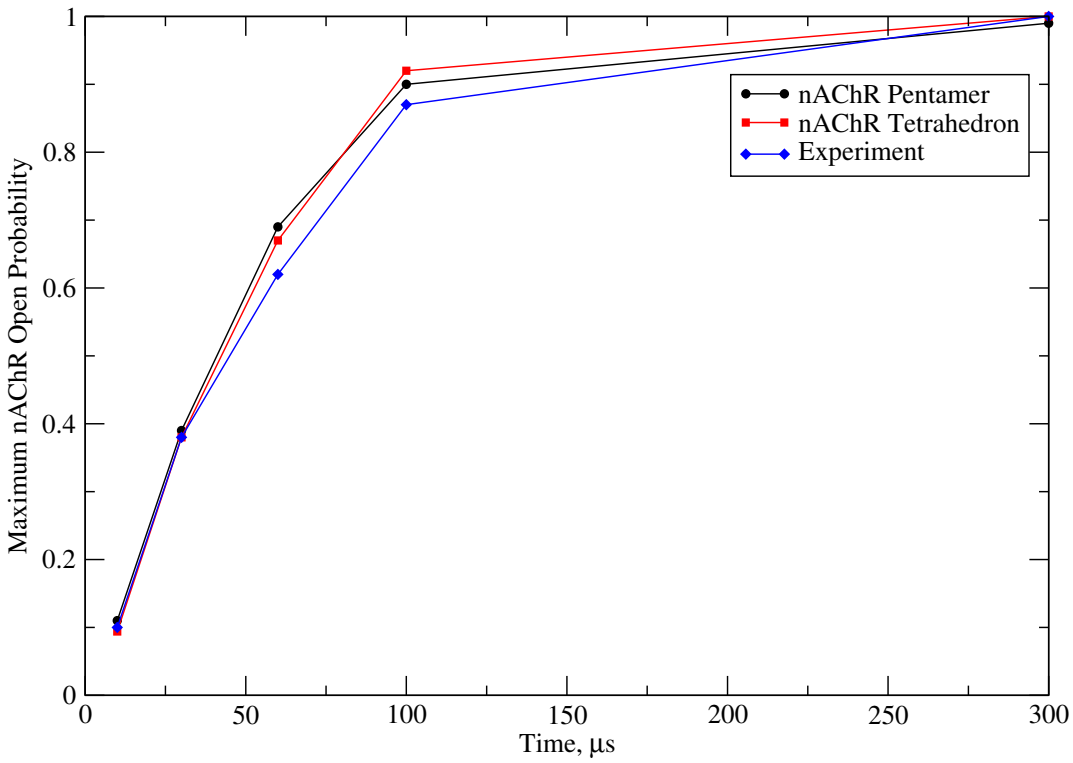

Figure III.4: The maximal open probabilities of the ion channel under different ACh concentrations for the pentameric, tetrahedral nAChR and the experiment, respectively.

Let Ω be the computational domain of the NMJ model and denote $\partial\Omega$ as the boundary. The strong form of the diffusion equation of our NMJ model [163, 11] for the ACh dynamics is:

$$\frac{\partial p(x,t)}{\partial t} = \nabla \cdot D\nabla p(x,t) \text{ in } \Omega \tag{5}$$

With boundary conditions read as,

$$\hat{n} \cdot D\nabla p(x,t) = \begin{cases} -k'_{act,AChE}[k_s^+(1-\sum_{i=1}^{3}\theta_i)p(x,t) - \frac{k_s^-\theta_1}{p(x,0)}], \text{ on } \partial\Omega^{\text{act}}_{\text{AChE}} \\ -k'_{act,nAChR}(k_{bind}^+ p(x,t) - k_{bind}^-), \text{ on } \partial\Omega^{\text{act}}_{\text{nAChR}} \\ 0, \text{ otherwise} \end{cases} \tag{6}$$

Where $k'_{act,AChE}$ and $k'_{act,nAChR}$ are defined as the AChE and nAChR reaction coefficients respectively, which were determined by sampling (see Section 3.1 below); $k_{bind}^+ = k_+[2(1-\sum_{i=1}^{3}\phi_i)+\phi_1]$, and $k_{bind}^- = \frac{k_-(\phi_1+2\phi_2)}{p(x,0)}$. $\partial\Omega^{act}_{nAChR}$ corresponds to a single ACh binding site boundary on a nAChR and $p(x,0)$ is the initial concentration of ACh. The intermediates for ACh hydrolysis $\{\theta_i\}$ and the different nAChR conformation states $\{\phi_i\}$ are determined through the corresponding sets of ODEs (Eq. 1 and 3) with ACh concentration evaluated at the corresponding boundaries. Following the definition in Holst et al. [188] and Cheng et al. [244], the "weak" formulation reads as

Find $p(x,t) \in V$ such that

$$< F(p(x,t)), v >= 0 \ \ \forall v \in V, \tag{7}$$

where

$$\begin{aligned} < F(p(x,t)), v >= & \int_\Omega (D\nabla p(x,t)\cdot\nabla v + \frac{\partial p(x,t)}{\partial t} v)dx \\ & - \int_{\partial\Omega^{act}_{AChE}} (-k'_{act,AChE}[k_s^+(1-\sum_{i=1}^{3}\theta_i)p(x,t) - \frac{k_s^-\theta_1}{p(x,0)}])dS \\ & - \int_{\partial\Omega^{act}_{nAChR}} (-k'_{act,nAChR}(k_{bind}^+ p(x,t) - k_{bind}^-))dS \end{aligned} \tag{8}$$

The neuromuscular junction model

A complete NMJ model includes a vesicle fused to the presynaptic membrane, a primary cleft, AChE clusters and nAChR pentamers. AChE clusters consisting of three AChE

tetramers are represented explicitly in the mesh as a cubic box with $1/8$ of the surface being active. The nAChR pentamers are modeled as pentagonal prisms placed at the bottom of a large cubic box with active sites occupying $1/8$ of the surface on two sides of each pentagonal prism, representing the independent treatment of the two ACh binding sites. To elucidate the geometric influence of the NMJ on the system dynamics, two different NMJ models have been prepared in this study.

The first NMJ model (denoted as Model I) presented in Fig. III.5 consists of 8 explicit cubic AChE clusters and 750 nAChR pentamers. The vesicle fused to the middle of the presynaptic membrane is modeled as a sphere of radius 0.024 μm centered at 0.016 μm above this membrane, leaving a circular area of radius 0.018 μm as the pore opening. The dimensions of the primary cleft are 0.30 μm (length), 0.10 μm (width) and 0.10 μm (height). The depth of the junction fold (JF) is 1.0 μm. 750 nAChR pentameric prisms are evenly distributed on the inner surface of the primary cleft and JF. The density of nAChR on the postsynaptic membrane of the primary cleft is circa 10,000 μm^{-2}. In the JF, from the crest to 0.25 μm into the fold, the density remains at 10,000 μm^{-2}, and then falls off to 5,000 μm^{-2} over another 0.4 μm, below which the density decreases dramatically until zero. 8 AChE clusters were put in the space of the primary cleft and JF, which represented 96 AChE monomers.

The second model (denoted as Model II) is depicted in Fig III.6. 323 cubic AChE and 29462 tetrahedral nAChRs are integrated. The tetrahedral nAChR models are developed similarly to the pentameric ones (see section 3.2), but reduce the computational demands. Model II includes a vesicle with the same size as Model I but with a different amount of AChE and nAChR. The length, width and height of the primary cleft for Model II are 0.95 μm, 2.0 μm and 0.1 μm, respectively. The depth of the junction fold (JF) is 0.8 μm. 29462 tetrahedral nAChRs (see Section 3.2 below) are placed on the surface of the primary cleft and JF. The density setup is the same as in the above model. 323 AChE clusters are integrated in the space of the primary cleft and JF, representing 3876 AChE monomers.

Numerical solution scheme for the complete NMJ model

Spatial approximation of the NMJ cleft space is performed by using a finite element method. The physical domain Ω of the NMJ cleft space is divided into a collection of tetrahedra by using NETGEN [245], a flexible mesh generation package. The detailed discretized weak

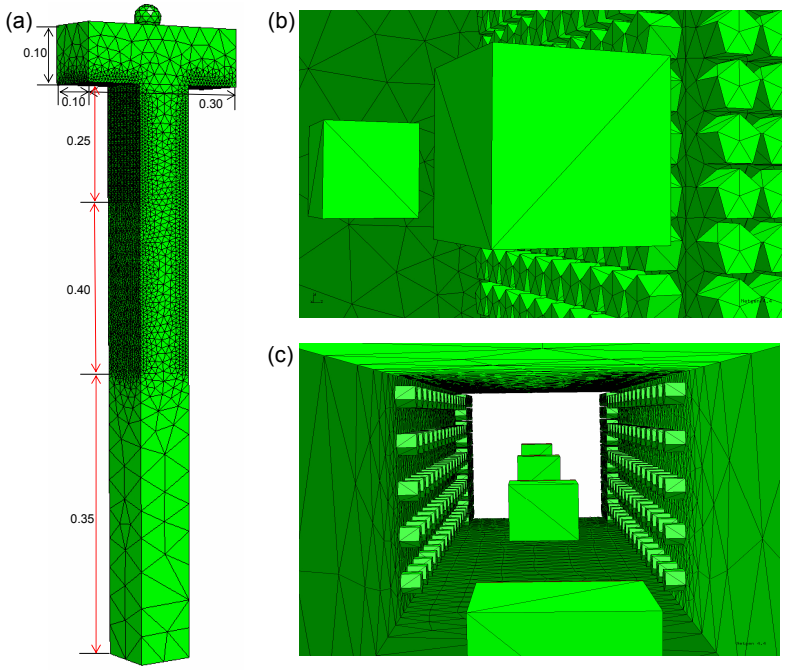

Figure III.5: Three views of the finite element mesh for Model I, with one secondary cleft and a spherical vesicle fused to the presynaptic membrane. The cubic boxes represent AChE, and pentameric prisms represent nAChR. (a) outside view; (b) inside of the primary cleft; (c) inside of the secondary cleft. The length unit is μm.

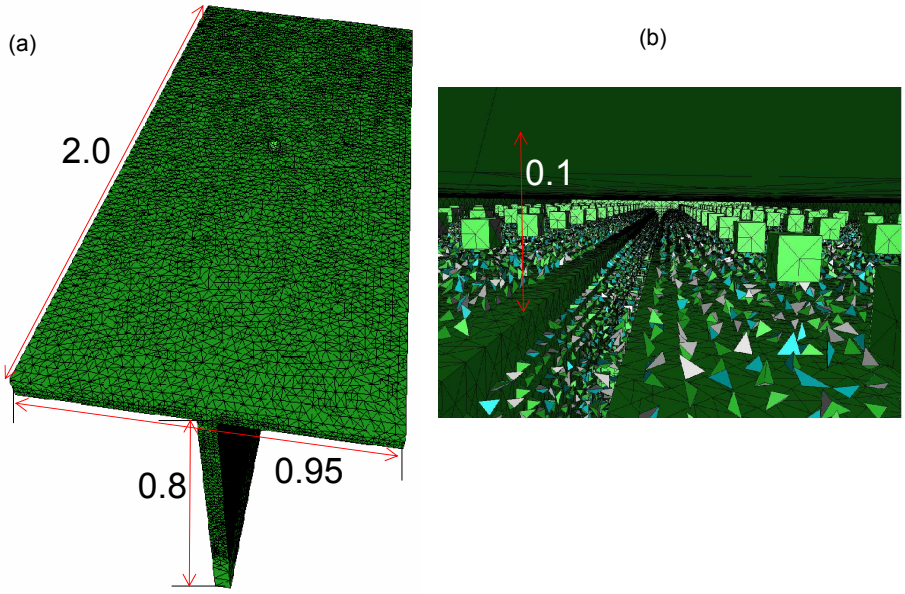

Figure III.6: Two views of the finite element mesh for Model II, in which each nAChR is represented as a tetrahedron. (a) outside view; (b) inside of the primary and secondary clefts. The length unit is μm.

formulation is listed in "Supplementary Material"[2].

The numerical solution of the above NMJ models is achieved by an iterative method to solve the 3D diffusion problem with reaction-determined boundaries. At each time step, the ACh concentration is first updated with the intermediates corresponding to different states of AChE and nAChR. Specifically, numerical solution of the linear algebraic problem arose from the temporal discretization with $\{\theta_i\}$ and $\{\phi_i\}$ evaluated at the previous time step is solved by using the conjugate gradient method with tolerance of 10^{-10}. Then with the updated ACh concentration profile, the various states of AChE and nAChR are evaluated by the solution of the corresponding kinetic equations of ACh binding. The spatial independence of the different states of AChE and nAChR enables a nodal solution for the ACh kinetic equations, for which we employed analytical solution to invert the linear algebraic problem raised from the temporal discretization using the Crank-Nicholson scheme. To ensure convergence and adequate resolution of the reaction kinetics and postsynaptic response, timesteps ranging from 10^{-1} μs to 10^{1} μs were used for the simulation. We have also attempted other solution schemes for solving the coupled ODE/PDE system and found that the current numerical scheme provided the best balance between overall stability and the computational demand of the solution algorithm. It takes less than 10 minutes to complete 1,000 timesteps on a single Intel Xeon 3.60GHz CPU for a system of $\sim$20,000 vertices (Model I).

Evaluation of the various states and conformations of the nAChR ion channel

nAChR can exist in unliganded, monoliganded and diliganded states. We evaluate the flux of ACh binding to the two active sites as,

$$I(t) = \int_{\partial\Omega^{act}_{nAChR}} k'_{act,nAChR}(k^{+}_{bind}\,p(x,t) - k^{-}_{bind})dS \tag{9}$$

The integration area is over the two ACh binding sites for each nAChR.

The number of bound ACh molecules (or postsynaptic coverage) can then be defined as the accumulating quantity of ACh:

[2]http://www.sciencedirect.com/science/MiamiMultiMediaURL/B6TFB-4MVN14T-1/B6TFB-4MVN14T-1-X/5222/503c91579d03fcf4f319a01b00490000/applic1.pdf

$$N(t) = \int_0^t I(\tau) d\tau \tag{10}$$

A receptor with $N(t) \geq 2$ represents the diliganded state, while $1 \leq N(t) < 2$ the monoliganded state and $0 \leq N(t) < 1$ the unliganded state.

The partial number of open channels in one ACh binding site of a nAChR can be calculated using the average value of ϕ_3.

$$\begin{aligned} p(O)^I &= \frac{\int_{\partial\Omega^I_{nAChR}} \phi_3 dS}{\int_{\partial\Omega^I_{nAChR}} dS} \\ p(O)^{II} &= \frac{\int_{\partial\Omega^{II}_{nAChR}} \phi_3 dS}{\int_{\partial\Omega^{II}_{nAChR}} dS} \end{aligned} \tag{11}$$

Here "I" and "II" denote the two ACh binding sites of one nAChR pentamer (Fig. III.2 (a)).

Then the partial number of open channels for one nAChR is $p(O) = p(O)^I + p(O)^{II}$, and the nominal (equivalent) number of open channels in the NMJ cleft is $N(O) = N_{nAChR} p(O)$.

III.A.4 Results and Discussion

Reactivity of the AChE

In this section, we compare the reactivity of the AChE model with experimental results by considering an *in silico* experiment by computing the reaction rate constant of an isolated AChE cluster confined in a cubic box. The concentration of ACh at the boundary of the cubic box is assumed to be constant. Specifically, we place an AChE cluster as described in Section 2 at the center of a cube with 0.30 μm edges. The boundary condition for $\partial\Omega^{act}_{AChE}$ in Eq. 7 is used on the surface of the interior cube, the AChE cluster. On the exterior cube boundary $\partial\Omega$ - $\partial\Omega^{act}_{AChE}$, the concentration of ACh is held at a different constant value for each "trial" simulation. At steady state, the analytical reaction rate of an AChE monomer can be written in the reaction scheme depicted in Fig. III.1 (d):

$$\upsilon(t \to \infty) = [AChE]_0 \left(\frac{k_{cat}}{1 + \frac{K_m}{p(x,t)}}\right)\left(\frac{1 + \frac{bp(x,t)}{K_{ss}}}{1 + \frac{p(x,t)}{K_{ss}}}\right) \tag{12}$$

Here $k_{cat} = (1.4 \pm 0.1) \times 10^5 min^{-1}$, $K_m = \frac{k_s^-}{k_s^+} = 46 \pm 3\mu M$ and $K_{ss} = \frac{k_{ss}^-}{k_{ss}^+} = 15 \pm 2mM$.

The recent calculations on an isolated AChE tetramer [176] suggest the reaction activity of one AChE cluster is approximately equivalent to that of 9 independent AChE monomers. Therefore, the analytical reaction rate of one AChE cluster $V(t \to \infty) = 9\upsilon(t \to \infty)$.

Following the mechanism in Fig. III.1 (d), the reaction rate at each node of one AChE active site is

$$\upsilon_i(t) = [AChE]_0 k_{cat}(\theta_1 + b\theta_3) \tag{13}$$

Therefore, the average reaction rate of one AChE cluster is

$$\upsilon(t) = \frac{\int \sum_{i=1}^{N_{tot}} \upsilon_i(t) dS}{\int 1 dS} \tag{14}$$

From the above equations, $k'_{act,AChE}$ can be determined by evaluating $V(\infty) = \lim_{t\to\infty} \upsilon(t)$ for ACh concentration on the outer boundary ranging from 0.01 mM to 100 mM. Fig. III.7 suggests an excellent agreement between the experimental and computational reaction rates [234]. Based on these results, we deduce $k'_{act,AChE} = 1.50 \times 10^{-5} M \cdot m^{-2}$.

Reactivity of the nAChR

Now we consider another *in silico* experiment by considering the behavior of nAChR. Specifically, 625 nAChRs are evenly placed at the base center of a large cubic box with 0.5 μm edges (Fig. III.3). Except the side with the embedded nAChRs (Neumann or reflecting boundary), all other sides are assigned as Dirichlet constant concentration boundaries. ACh molecules fill the space inside the cubic box with the initial concentration at 10.0 μM, 30.0 μM, 60.0 μM, 100.0 μM for each trial, respectively.

Evaluation of the ion-channel maximum open probabilities under different initial ACh concentrations using Eq. 11 yields the results shown in Fig.III.4. All the open percentages have been calibrated with the experimental data in [246]. Following Smart and McCammon et al.(1998), $k'_{act,nAChR}$ can finally be determined as $6.6\times10^{-6} M \cdot m^{-2}$.

The complete NMJ models

We simulated Model I (Fig. III.5) with an initial ACh distributed only inside the vesicle to examine the dynamics of the ACh, AChE and conformational chances of nAChR. The initial concentration of ACh of 300 mM corresponds to a ACh density of $1.8\times10^{8} \mu m^{-3}$ [247, 248, 163,

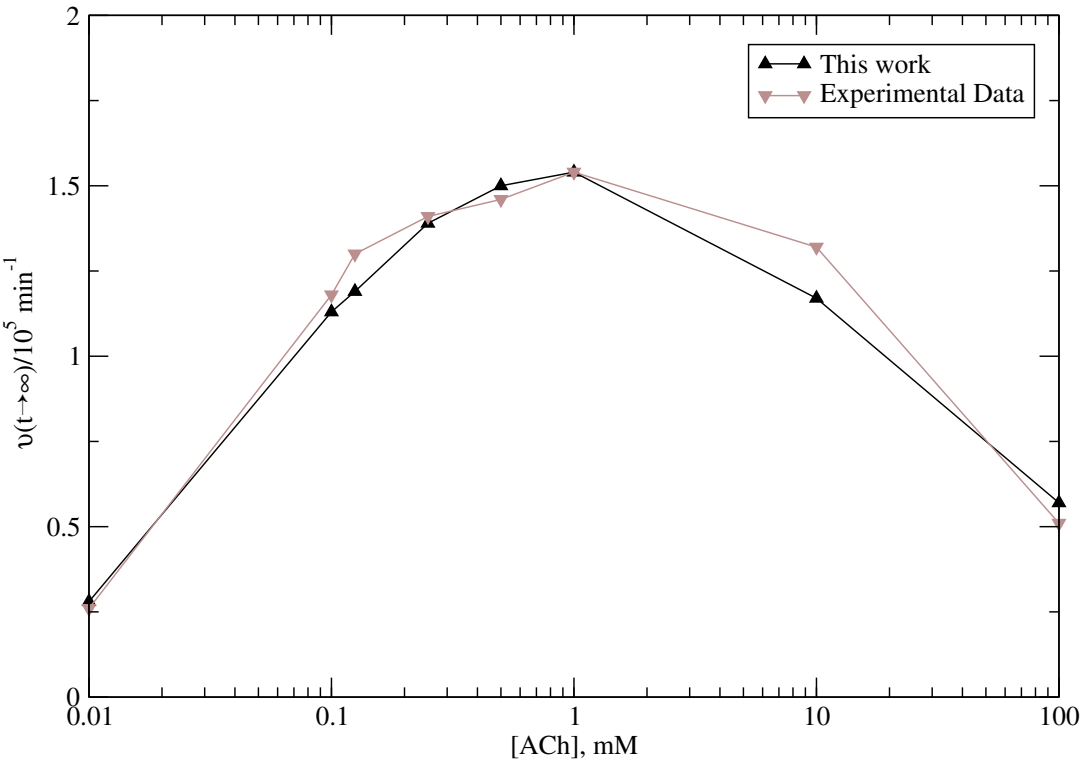

Figure III.7: Concentration dependencies of the AChE activity in both the experiment and this work.

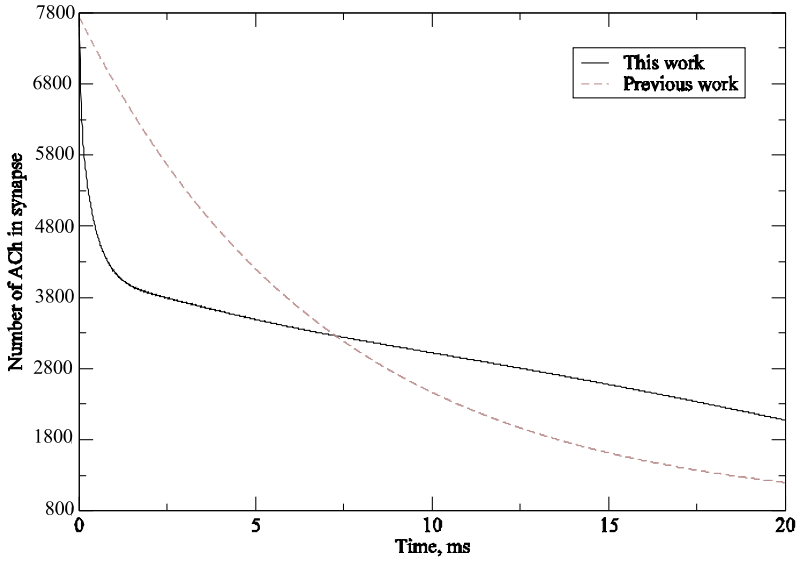

Figure III.8: Total number of ACh molecules in Model I, comparing with the simple AChE kinetic model in the previous work [11].

249, 11]. The time evolution of ACh is monitored to elucidate insights for the neurotransmission process.

Fig. III.8 depicts the time course of the total number of ACh molecules during the first 20 *ms* following the release of ACh into the junction. With the complete kinetic model in this work, the overall time course can be separated into two phases. The first phase corresponds to approximately the first 1.5 *ms* following release. During this phase, the number of ACh molecules in the model drops dramatically due to rapid binding of ACh to both AChE and nAChR. In the second phase ($t \geq 1.5ms$), ACh concentration decays gradually due to the "slower" consumption of ACh through hydrolysis by AChE. If only a linear reaction rate is used for ACh hydrolysis and ACh-nAChR binding is assumed to be at equilibrium (dotted line in Fig. III.8), then only a gradual consumption of ACh is observed. This is consistent with the previous observation by Tai et al. [11].

Comparing with previous studies [163, 11], the reactive boundaries in the present work are determined by the kinetics of ACh binding to AChE or nAChR. The AChE kinetics in response to a quantal release of ACh are shown in Fig. III.9. The amounts of three AChE complexes have been determined with timesteps of 0.1 μs. The high accumulation of the complex

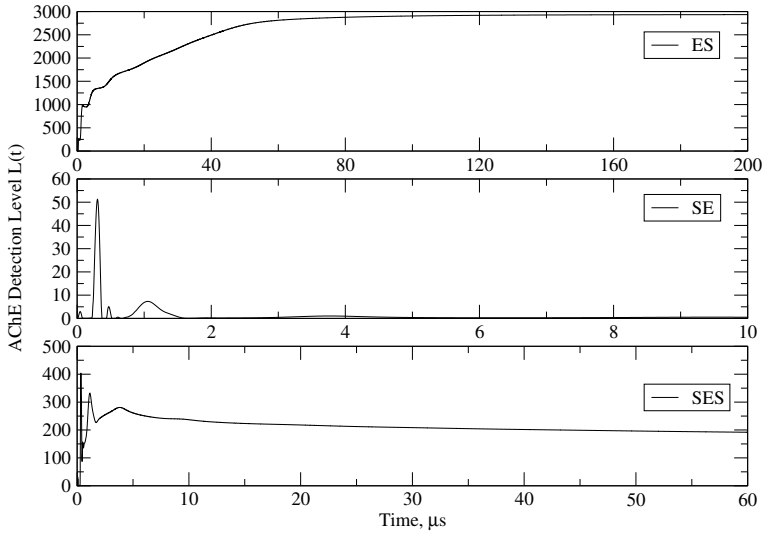

Figure III.9: The time course of three AChE complexes in Model I: ES, SE and SES represent complexes that the substrate ACh occupies the active site, the peripheral site and both two sites, respectively.

ES (ACh in the active site) suggests that most of ACh are trapped as this intermediate and the complete hydrolysis of ACh may take much longer. On the other hand, the amount of SE (ACh in the peripheral site) stays near zero after the first few μs. The relative amount of SES (ACh in both the active and peripheral sites) remains less than 10% of ES. This suggests that the substrate inhibition in the NMJ might be negligible in the case of single vesicle release.

Previous work didn't explicitly model nAChRs on the postsynaptic membrane. Here, not only two nAChR models have been proposed, but also various nAChR conformations have been analyzed. In Model I, the nAChR pentamers undergo continuous conformational changes during the simulation (Fig. III.10). Fig. III.10 (c) indicates that the number of the unliganded nAChRs exponentially decreases to below 200 during the first 20 μs of simulation. The number of monoliganded nAChR jumps to nearly 200 in a short time and rapidly decays to below 25. Most of the nAChRs rapidly become diliganded. It takes around 150μs to 200 μs for the whole system to reach a nearly steady state with about 700 nAChRs in the diliganded conformation. The number of closed state diliganded receptors increases to above 200 in the first 15 μs, and then decays exponentially. The open state shows a parabola-shaped increase to a maximum, and then the number of open channels slowly decreases. It must be noted that most of the nAChR receptors keep two ACh bound during 1 ms of simulation. The dissociation rate of ACh from the

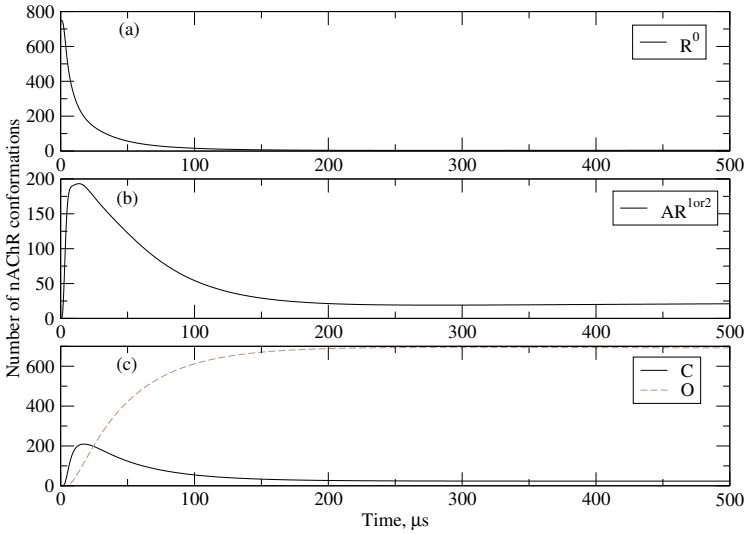

Figure III.10: The Number of various nAChR conformations in Model I: R^0 denotes the unliganded nAChR, AR^{1or2} the monoliganded nAChR, C and O the diliganded closed and open nAChR, respectively.

diliganded state is quite slow in experiments ($>$1 s).

We also tested model sensitivities by varying the number of AChE clusters in the model. Fig.III.11 shows the effect of modulating the density of AChE. The number of open channels gradually reduces along with the increase of AChE clusters, which aligns well with physical intuition and is qualitatively consistent with observations by using Monte Carlo simulation [233].

To validate the above observation from the simulation results, we extended our study on Model II (Fig. III.6). Fig. III.12 shows the time courses of all the AChE intermediates and the number of open channels. The qualitatively consistent trends suggest similar dynamics and behavior to Model I, but geometric features of the primary cleft and the distribution of AChE clusters and nAChRs play an important role in determining the quantitative feature of the pharmacokinetics and pharmacodynamics analysis. It takes around 100 μs to reach the nearly steady state. Around 300 of 323 AChE clusters remain in the ES complex state. Meanwhile, the maximal open percentage of nAChR decreases to 0.3% while above 95% in Model I. This is reasonable since we have a large number of AChE clusters and nAChRs in Model II.

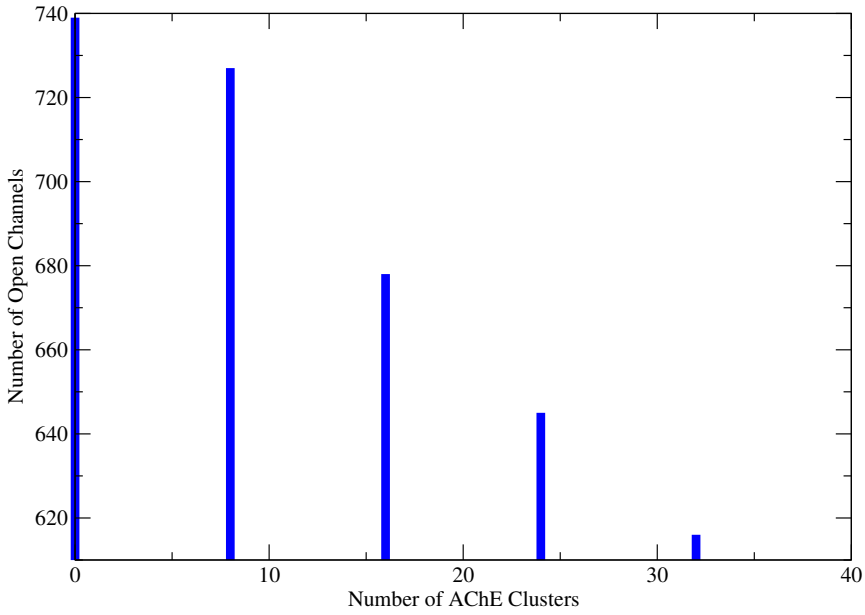

Figure III.11: Effect of varying the number of AChE clusters on the number of open channels in Model I.

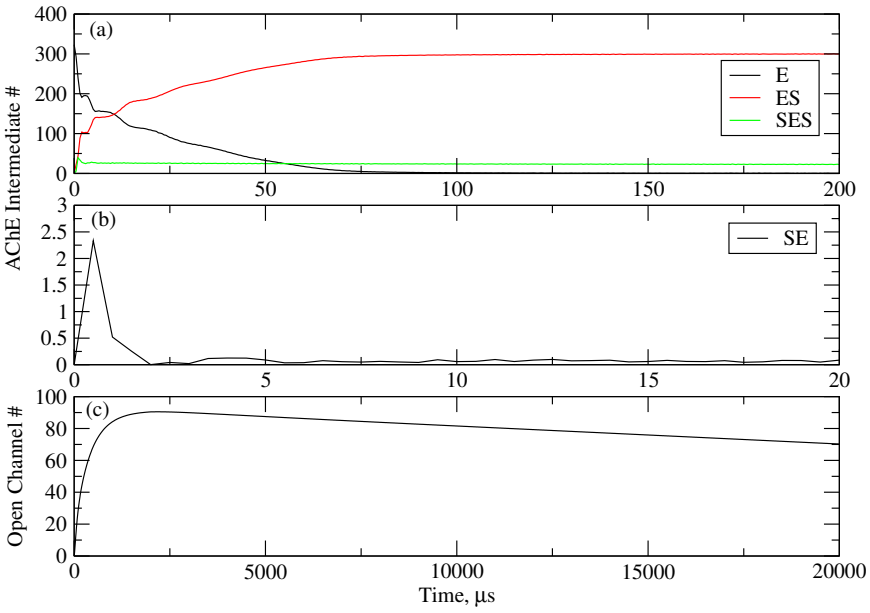

Figure III.12: Finite element solutions of Model II: (a) and (b) Number of all the AChE complexes; (c) Number of open channels.

III.A.5 Conclusions

In this work, 3D neuromuscular junction models with explicit geometric details of both AChEs and nAChRs have been studied with the finite element method. By considering detailed kinetic processes of AChE and nAChR, time-dependent conformational state conversion of the nAChR can be observed during the simulations. In addition, through comparison with simple kinetic models in previous works, we discovered unique characteristics in the consumption of ACh in a neuromuscular junction after the release of a quanta of ACh into the synapse.

Our simulation results suggest that model geometry and size have profound effects on the postsynaptic nAChR open probabilities, implying that the quantal release can have different amplification characteristics with the fixed amount of ACh. Comparing with the 2D NMJ model in Naka et al.[250, 222], our 3D models revealed additional detailed information and features during ACh diffusion, binding and hydrolysis. We derived a numerical solution strategy for solving the system of partial differential equations (describing ACh diffusion) with time dependent, ODE based boundary conditions (describing ACh hydrolysis and ACh-nAChR binding/dissociation). Such reaction-diffusion coupling models might aid future pharmacokinetics studies for NMJ-related diseases by considering the activities of compounds at both AChE and AChR. To this end, both 3D geometry and comprehensive kinetic models are essential for an integrative NMJ model.

During the 15 ms simulation, the dynamics of ACh in the synaptic cleft might be characterized into two stages. In the first stage, ACh molecules bind with nAChRs while some of them are destroyed by AChE. Then AChE removes the unreacted ACh from the synaptic cleft in a subsequent stage. Our results further support previous observations that most of the neurotransmitters will be eliminated before subsequent rebinding to nAChR can occur [238, 251, 252]. In addition, although the concentration of ACh in the vesicle is much higher than 1 mM, the overall ACh concentration at the AChE clusters after one quantal ACh release never reaches 1 mM, therefore, the ACh substrate inhibition might be negligible in the case of single vesicle release.

The ACh binding with nAChRs occurs within 5 μs after a ACh quantal release. nAChRs undergo several conformation changes and then some channels will open to conduct Na^+/K^+ ions. In our simulations, the number of unliganded, monoliganded and diliganded ion channels has been recorded along with the simulation time. Additionally, the time course of open channels

is traced and analyzed for the diliganded ion channels.

While our simulation results reveal many of the features in ACh diffusion in a neuromuscular junction upon the release of a quanta of ACh from the presynaptic membrane, a major shortcoming in the current work is that the model does not take into account stochasticity and discrete processes occurring in the NMJ. The local concentration of ACh is of order μM and therefore the number of ACh molecules surviving for few of μs after release of one vesicle may range from 100 to 1000. This number of ACh molecules makes the continuum assumption approximate. However, our preliminary results for comparing stochastic and deterministic models suggests qualitative similarities between these two methods for the same synapse model. Given the computationally efficient nature of deterministic models and finite element methods, our model is a reasonable alternative to stochastic methods for studying cholinergic synaptic transmission.

To illustrate the principle and usefulness of our approach, we focused our effort on models with relatively simple pre/post-synaptic membrane geometries. Despite the lack of realism of the NMJ model, our simulation is capable of capturing the geometrical difference, and extending the software for simulating large and realistic meshes replicating complex NMJ structures as observed by electronmicroscopy is straightforward. Constructing large and realistic meshes requires powerful adaptive meshing methods that are capable of reconstructing real NMJ structures. Part of this work has recently proven to be possible as with the adaptive meshing tool of "Mol-LIBIE" by Zhang et al. [253]. The development of such models will enable a realistic description of synapse activity, as well as modeling the interplay between morphological changes of the synapse, chemical and molecular reactions of AChE and nAChR, and ACh diffusion in the complicated geometry.

Of equal importance to building a realistic synapse model is to construct detailed kinetic models for both AChE hydrolysis and AChE-nAChR binding. These kinetic models represents both the kinetic events happened during the reaction, as well as the molecular conformation changes of the enzyme and receptors. A detailed understanding of these events will enable modeling of different AChE and nAChR mutations, as well as catalyze the development of pharmaceutical agents for various NMJ diseases. Of specific interest is to describe desensitized conformations for complementing new experimental findings through kinetic modeling of nAChR. Moreover, the role of substrate inhibition of AChE in synaptic activity can be ex-

amined through releasing large numbers of quanta. Some of these topics are currently under investigation and will be described in forthcoming manuscripts.

III.A.6 Acknowledgments

This work has been supported in part by grants from the NSF and NIH. Additional support has been provided by NBCR, CTBP, HHMI, the W. M. Keck Foundation.

Chapter III is adapted from "Continuum Simulations of Acetylcholine Diffusion with Reaction-determined Boundaries in Neuromuscular Junction Models" published in 2007 in *Biophys. Chem.* (Volumn 127, pages 129-139), authored by Yuhui Cheng, Jason K. Suen, Zoran Radić, Stephen D. Bond, Michael J. Holst and J. Andrew McCammon.

Bibliography

[1] Z. Radić, D. M. Quinn, J. A. McCammon, and P. Taylor. Electrostatic influence on the kinetics of ligand binding to acetylcholinesterase - distinctions between active center ligands and fasciculin. *J. Biol. Chem.*, 272(37):23265–23277, 1997.

[2] Z. Radić and P. Taylor. Interaction kinetics of reversible inhibitors and substrates with acetylcholinesterase and its fasciculin 2 complex. *J. Biol. Chem.*, 276(7):4622–4633, 2001.

[3] J. C. Hart, D. W. Sheppard, I. H. Hillier, and N. A. Burton. What is the mechanism of phosphoryl transfer in protein kinases? a hybrid quantum mechanical/molecular mechanical study. *Chem. Commun.*, (1):79–80, 1999.

[4] J. C. Hart, I. H. Hillier, N. A. Burton, and D. W. Sheppard. An alternative role for the conserved asp residue in phosphoryl transfer reactions. *J. Am. Chem. Soc.*, 120(51):13535–13536, 1998.

[5] M. C. Hutter and V. Helms. Influence of key residues on the reaction mechanism of the cAMP-dependent protein kinase. *Protein Sci.*, 8(12):2728–2733, 1999.

[6] Y. Hirano, M. Hata, T. Hoshino, and M. Tsuda. Quantum chemical study on the catalytic mechanism of the C- subunit of cAMP-dependent protein kinase. *J. Phys. Chem. B*, 106(22):5788–5792, 2002.

[7] A. Cavalli, M. De vivo, and M. Recanatini. Density functional study of the enzymatic reaction catalyzed by a cyclin-dependent kinase. *Chem. Commun.*, (11):1308–1309, 2003.

[8] M. Valiev, R. Kawai, J. A. Adams, and J. H. Weare. The role of the putative catalytic base in the phosphoryl transfer reaction in a protein kinase: First-principles calculations. *J. Am. Chem. Soc.*, 125(33):9926–9927, 2003.

[9] N. Diaz and M. J. Field. Insights into the phosphoryl-transfer mechanism of cAMP-dependent protein kinase from quantum chemical calculations and molecular dynamics simulations. *J. Am. Chem. Soc.*, 126(2):529–542, 2004.

[10] G. Henkelman, M. X. LaBute, C. S. Tung, P. W. Fenimore, and B. H. McMahon. Conformational dependence of a protein kinase phosphate transfer reaction. to be published.

[11] K. Tai, S. D. Bond, H. R. Macmillan, N. A. Baker, M. J. Holst, and J. A. McCammon. Finite element simulations of acetylcholine diffusion in neuromuscular junctions. *Biophys. J.*, 84(4):2234–2241, 2003.

[12] Y. H. Cheng and Q. X. Guo. Several preliminary applications of *ab initio* dft theory in physical organic chemistry. *USTC BS thesis*, 2002.

[13] D. A. Johnson, P. Akamine, E. Radzio-Andzelm, Madhusudan, and S. S. Taylor. Dynamics of cAMP-dependent protein kinase. *Chem. Rev.*, 101(8):2243–2270, 2001.

[14] D. A. Walsh, John P. Perkins, and Edwin G. Krebs. An adenosine 3',5'-monophosphate-dependent protein kinase from rabbit skeletal muscle. *J .Biol. Chem.*, 243(13):3763–3774, JUN 1968.

[15] S. Shoji, K. Titani, J. G. Demaille, and E. H. Fischer. Sequence of 2 phosphorylated sites in the catalytic subunit of bovine cardiac-muscle adenosine 3'-5'-monophosphate-dependent protein-kinase. *J. Biol. Chem.*, 254(14):6211–6214, 1979.

[16] L. W. Slice and S. S. Taylor. Expression of the catalytic subunit of cAMP-dependent protein kinase in escherichia coli. *J. Biol. Chem.*, 264(35):20940–20946, 1989.

[17] C. S. Gibbs and M. J. Zoller. Rational scanning mutagenesis of a protein-kinase identifies functional regions involved in catalysis and substrate interactions. *J. Biol. Chem.*, 266(14):8923–8931, 1991.

[18] C. S. Gibbs, D. R. Knighton, J. M. Sowadski, S. S. Taylor, and M. J. Zoller. Systematic mutational analysis of cAMP-dependent protein-kinase identifies unregulated catalytic subunits and defines regions important for the recognition of the regulatory subunit. *J. Biol. Chem.*, 267(7):4806–4814, 1992.

[19] J. A. Adams, M. L. McGlone, R. Gibson, and S. S. Taylor. Phosphorylation modulates catalytic function and regulation in the cAMP-dependent protein-kinase. *Biochemistry*, 34(8):2447–2454, 1995.

[20] W. Yonemoto, M. L. McGlone, B. Grant, and S. S. Taylor. Autophosphorylation of the catalytic subunit of cAMP-dependent protein kinase in escherichia coli. *Protein Eng.*, 10(8):915–925, 1997.

[21] B. D. Grant and J. A. Adams. Pre-steady-state kinetic analysis of cAMP-dependent protein kinase using rapid quench flow techniques. *Biochemistry*, 35(6):2022–2029, 1996.

[22] W. Hemmer, M. McGlone, I. Tsigelny, and S. S. Taylor. Role of the glycine triad in the atp-binding site of camp- dependent protein kinase. *J. Biol. Chem.*, 272(27):16946–16954, 1997.

[23] R. T. Aimes, W. Hemmer, and S. S. Taylor. Serine-53 at the tip of the glycine-rich loop of cAMP-dependent protein kinase: role in catalysis, p-site specificity, and interaction with inhibitors. *Biochemistry*, 39(28):8325–8332, 2000.

[24] M. H. J. Seifert, C. B. Breitenlechner, D. Bossemeyer, R. Huber, T. A. Holak, and R. A. Engh. Phosphorylation and flexibility of cyclic-amp-dependent protein kinase (pka) using p-31 nmr spectroscopy. *Biochemistry*, 41(19):5968–5977, 2002.

[25] J. Lew, N. Coruh, I. Tsigelny, S. Garrod, and S. S. Taylor. Synergistic binding of nucleotides and inhibitors to cAMP-dependent protein kinase examined by acrylodan fluorescence spectroscopy. *J. Biol. Chem.*, 272(3):1507–1513, 1997.

[26] J. Shaffer and J. A. Adams. Detection of conformational changes along the kinetic pathway of protein kinase a using a catalytic trapping technique. *Biochemistry*, 38(37):12072–12079, 1999.

[27] X. Cheng, S. Shaltiel, and S. S. Taylor. Mapping substrate-induced conformational changes in cAMP-dependent protein kinase by protein footprinting. *Biochemistry*, 37(40):14005–14013, 1998.

[28] Madhusudan, P. Akamine, N. H. Xuong, and S. S. Taylor. Crystal structure of a transition state mimic of the catalytic subunit of cAMP-dependent protein kinase. *Nat. Struct. Biol.*, 9(4):273–277, 2002.

[29] D. Bossemeyer, R. A. Engh, V. Kinzel, H. Ponstingl, and R. Huber. Phosphotransferase and substrate binding mechanism of the cAMP-dependent protein-kinase catalytic subunit from porcine heart as deduced from the 2.0 angstrom structure of the complex with Mn2+ adenylyl imidodiphosphate and inhibitor peptide PKI(5-24). *Embo J.*, 12(3):849–859, 1993.

[30] J. Yang, L. F. Ten eyck, N. H. Xuong, and S. S. Taylor. Crystal structure of a cAMP-dependent protein kinase mutant at 1.26 angstrom: new insights into the catalytic mechanism. *J. Mol. Biol.*, 336(2):473–487, 2004.

[31] Madhusudan, E. A. Trafny, N. H. Xuong, J. A. Adams, L. F. Teneyck, S. S. Taylor, and J. M. Sowadski. cAMP-dependent protein-kinase - crystallographic insights into substrate recognition and phosphotransfer. *Protein Sci.*, 3(2):176–187, 1994.

[32] J. Zheng, D. R. Knighton, N. H. Xuong, S. S. Taylor, J. M. Sowadski, and L. F. Teneyck. Crystal-structures of the myristylated catalytic subunit of cAMP-dependent protein-kinase reveal open and closed conformations. *Protein Sci.*, 2(10):1559–1573, 1993.

[33] M. Y. Yoon and P. F. Cook. Chemical mechanism of the adenosine cyclic 3',5'-monophosphate dependent protein-kinase from pH studies. *Biochemistry*, 26(13):4118–4125, 1987.

[34] J. Zhou and J. A. Adams. Is there a catalytic base in the active site of cAMP-dependent protein kinase? *Biochemistry*, 36(10):2977–2984, 1997.

[35] S. K. Hanks and A. M. Quinn. Protein-kinase catalytic domain sequence database - identification of conserved features of primary structure and classification of family members. *Method Enzymol.*, 200:38–62, 1991.

[36] D. R. Knighton, D. L. Cadena, J. Zheng, L. F. Teneyck, S. S. Taylor, J. M. Sowadski, and G. N. Gill. Structural features that specify tyrosine kinase-activity deduced from homology modeling of the epidermal growth-factor receptor. *Proc. Natl. Acad. Sci. U. S. A.*, 90(11):5001–5005, 1993.

[37] F. Li, M. Gangal, C. Juliano, E. Gorfain, S. S. Taylor, and D. A. Johnson. Evidence for an internal entropy contribution to phosphoryl transfer: a study of domain closure, backbone flexibility, and the catalytic cycle of cAMP-dependent protein kinase. *J. Mol. Biol.*, 315(3):459–469, 2002.

[38] D. W. Sheppard, N. A. Burton, and I. H. Hillier. *ab initio* hybrid quantum mechanical/molecular mechanical studies of the mechanisms of the enzymes protein kinase and thymidine phosphorylase. *Theochem-J. Mol. Struct.*, 506:35–44, 2000.

[39] K. Ginalski, P. Grochowski, B. Lesyng, and D. Shugar. DFT calculations and parameterization of the approximate valence bond method to describe the phosphoryl transfer reaction in a model system. *Int. J. Quantum Chem.*, 90(3):1129–1139, 2002.

[40] S. Hur and T. C. Bruice. The near attack conformation approach to the study of the chorismate to prephenate reaction. *Proc. Natl. Acad. Sci. U. S. A.*, 100(21):12015–12020, 2003.

[41] Y. Zhang, T. S. Lee, and W. Yang. A pseudobond approach to combining quantum mechanical and molecular mechanical methods. *J. Chem. Phys.*, 110(1):46–54, 1999.

[42] Y. Zhang, H. Liu, and W. Yang. Free energy calculation on enzyme reactions with an efficient iterative procedure to determine minimum energy paths on a combined *ab initio* QM/MM potential energy surface. *J. Chem. Phys.*, 112(8):3483–3492, 2000.

[43] Yingkai Zhang, Haiyan Liu, and Weitao Yang. *ab initio* QM/MM and free energy calculations of enzyme reactions. In et al. T. Schlick, editor, *Methods for Macromolecular Modeling*, pages 332–354. Springer-Verlag, New York, 2002.

[44] H. Liu, Y. Zhang, and W. Yang. How is the active site of enolase organized to catalyze two different reaction steps? *J. Am. Chem. Soc.*, 122(28):6560–6570, 2000.

[45] Y. K. Zhang, J. Kua, and J. A. McCammon. Role of the catalytic triad and oxyanion hole in acetylcholinesterase catalysis: an *ab initio* QM/MM study. *J. Am. Chem. Soc.*, 124(35):10572–10577, 2002.

[46] Y. Zhang, J. Kua, and J. A. McCammon. Influence of structural fluctuation on enzyme reaction energy barriers in combined quantum mechanical/molecular mechanical studies. *J. Phys. Chem. B*, 107(18):4459–4463, 2003.

[47] G. A. Cisneros, H. Liu, Y. Zhang, and W. Yang. *ab initio* QM/MM study shows there is no general acid in the reaction catalyzed by 4-oxalocrotonate tautornerase. *J. Am. Chem. Soc.*, 125(34):10384–10393, 2003.

[48] G. A. Cisneros, M. Wang, P. Silinski, M. C. Fitzgerald, and W. Yang. The protein backbone makes important contributions to 4-oxalocrotonate tautomerase enzyme catalysis: understanding from theory and experiment. *Biochemistry*, 43:6885–6892, 2004.

[49] D. A. Case, D. A. Pearlman, J. W. Caldwell, T. E. Cheatham, W. S. Ross, C. L. Simmerling, T. A. Darden, K. M. Merz, R. V. Stanton, A. L. Cheng, J. J. Vincent, M. Crowley, D. M. Ferguson, V. Tsui, R. J. Radmer, Y. Duan, J. Pitera, I. Massova, G. L. Seibel, U. C. Singh, P. K. Weiner, and P. A. Kollman. *Amber 7.0*. University of California, San Francisco, CA., 2002.

[50] G. Vriend. WHAT IF - a molecular modeling and drug design program. *J. Mol. Graph.*, 8(1):52–56, 1990.

[51] W. D. Cornell, P. Cieplak, C. I. Bayly, I. R. Gould, K. M. Merz, D. M. Ferguson, D. C. Spellmeyer, T. Fox, J. W. Caldwell, and P. A. Kollman. A 2nd generation force-field for the simulation of proteins, nucleic-acids, and organic-molecules. *J. Am. Chem. Soc.*, 117(19):5179–5197, 1995.

[52] K. L. Meagher, L. T. Redman, and H. A. Carlson. Development of polyphosphate parameters for use with the amber force field. *J. Comput. Chem.*, 24(9):1016–1025, 2003.

[53] T. Darden, D. York, and L. Pedersen. Particle mesh ewald - an n.log(n) method for ewald sums in large systems. *J. Chem. Phys.*, 98(12):10089–10092, 1993.

[54] J. P. Ryckaert, G. Ciccotti, and H. J. C. Berendsen. Numerical-integration of cartesian equations of motion of a system with constraints - molecular-dynamics of n-alkanes. *J. Comput. Phys.*, 23(3):327–341, 1977.

[55] I. H. Williams and G. M. Maggiora. Use and abuse of the distinguished-coordinate method for transition-state structure searching. *Theochem-J. Mol. Struct.*, 6(3-4):365–378, 1982.

[56] J. W. Ponder. *TINKER, Software Tools for Molecular Design, Version 3.6*. The most updated version for the TINKER program can be obtained from J. W. Ponder's World Wide Web site at http://dasher.wustl.edu/tinker., February 1998.

[57] A. S. Mildvan. Mechanisms of signaling and related enzymes. *Proteins*, 29(4):401–416, 1997.

[58] K. Kim and P. A. Cole. Measurement of a bronsted nucleophile coefficient and insights into the transition state for a protein tyrosine kinase. *J. Am. Chem. Soc.*, 119(45):11096–11097, 1997.

[59] K. Kim and P. A. Cole. Kinetic analysis of a protein tyrosine kinase reaction transition state in the forward and reverse directions. *J. Am. Chem. Soc.*, 120(28):6851–6858, 1998.

[60] D. M. Williams and P. A. Cole. Proton demand inversion in a mutant protein tyrosine kinase reaction. *J. Am. Chem. Soc.*, 124(21):5956–5957, 2002.

[61] K. Parang, J. H. Till, A. J. Ablooglu, R. A. Kohanski, S. R. Hubbard, and P. A. Cole. Mechanism-based design of a protein kinase inhibitor. *Nat. Struct. Biol.*, 8(1):37–41, 2001.

[62] J. Granot, A. S. Mildvan, H. N. Bramson, and E. T. Kaiser. Magnetic-resonance measurements of intersubstrate distances at the active-site of protein-kinase using substitution-inert cobalt(iii) and chromium(iii) complexes of adenosine 5'- (beta,gamma-methylenetriphosphate). *Biochemistry*, 19(15):3537–3543, 1980.

[63] A. Cook, E. D. Lowe, E. D. Chrysina, V. T. Skamnaki, N. G. Oikonomakos, and L. N. Johnson. Structural studies on phospho-CDK2/cyclin a bound to nitrate, a transition state analogue: implications for the protein kinase mechanism. *Biochemistry*, 41(23):7301–7311, 2002.

[64] A. J. Ablooglu, M. Frankel, E. Rusinova, J. B. A. Ross, and R. A. Kohanski. Multiple activation loop conformations and their regulatory properties in the insulin receptor's kinase domain. *J. Biol. Chem.*, 276(50):46933–46940, 2001.

[65] R. R. Poyner, T. M. Larsen, S. W. Wong, and G. H. Reed. Functional and structural changes due to a serine to alanine mutation in the active-site flap of enolase. *Arch. Biochem. Biophys.*, 401:155–163, 2002.

[66] M. J. Moore, J. R. Kanter, K. C. Jones, and S. S. Taylor. Phosphorylation of the catalytic subunit of protein kinase a - autophosphorylation versus phosphorylation by phosphoinositide-dependent kinase-1. *J. Biol. Chem.*, 277(49):47878–47884, 2002.

[67] M. J. Moore, J. A. Adams, and S. S. Taylor. Structural basis for peptide binding in protein kinase a - role of glutamic acid 203 and tyrosine 204 in the peptide-positioning loop. *J. Biol. Chem.*, 278(12):10613–10618, 2003.

[68] S. K. Hanks and T. Hunter. Protein kinases .6. the eukaryotic protein-kinase superfamily - kinase (catalytic) domain-structure and classification. *Faseb J.*, 9(8):576–596, 1995.

[69] J. A. Adams and S. S. Taylor. Energetic limits of phosphotransfer in the catalytic subunit of cAMP-dependent protein-kinase as measured by viscosity experiments. *Biochemistry*, 31(36):8516–8522, 1992.

[70] F. W. Herberg, M. L. Doyle, S. Cox, and S. S. Taylor. Dissection of the nucleotide and metal-phosphate binding sites in cAMP-dependent protein kinase. *Biochemistry*, 38(19):6352–6360, 1999.

[71] L. N. Johnson, M. E. M. Noble, and D. J. Owen. Active and inactive protein kinases: Structural basis for regulation. *Cell*, 85(2):149–158, APR 19 1996.

[72] P. Cohen. The role of protein phosphorylation in human health and disease - delivered on June 30th 2001 at the FEBS meeting in Lisbon. *Eur. J. Biochem.*, 268(19):5001–5010, 2001.

[73] P. Blume-jensen and T. Hunter. Oncogenic kinase signalling. *Nature*, 411(6835):355–365, 2001.

[74] R. A. Engh and D. Bossemeyer. Structural aspects of protein kinase control - role of conformational flexibility. *Pharmacol. Ther.*, 93(2-3):99–111, 2002.

[75] J. A. Adams. Activation loop phosphorylation and catalysis in protein kinases: is there functional evidence for the autoinhibitor model? *Biochemistry*, 42(3):601–607, 2003.

[76] B. Nolen, S. Taylor, and G. Ghosh. Regulation of protein kinases: controlling activity through activation segment conformation. *Mol. Cell*, 15(5):661–675, 2004.

[77] S. K. Hanks, A. M. Quinn, and T. Hunter. The protein-kinase family - conserved features and deduced phylogeny of the catalytic domains. *Science*, 241(4861):42–52, JUL 1 1988.

[78] P. Taylor and Z. Radić. The cholinesterases: from genes to proteins. *Annu. Rev. Pharmacol. Toxicol.*, 34:281–320, 1994.

[79] D. Bossemeyer. Protein-kinases - structure and function. *FEBS Lett.*, 369(1):57–61, 1995.

[80] Y. Cheng, Y. Zhang, and J. A. McCammon. How does the cAMP-dependent protein kinase catalyze the phosphorylation reaction: an *ab initio* QM/MM study. *J. Am. Chem. Soc.*, 127(5):1553–1562, 2005.

[81] R. A. Engh and D. Bossemeyer. The protein kinase activity modulation sites: mechanisms for cellular regulation - targets for therapeutic intervention. In *ADVANCES IN ENZYME REGULATION J9 ADVAN ENZYM REGUL*, volume 41, pages 121–149. 2001.

[82] S. R. Hubbard. Crystal structure of the activated insulin receptor tyrosine kinase in complex with peptide substrate and ATP analog. *Embo J.*, 16(18):5572–5581, 1997.

[83] Y. Zhang, H. Liu, and W. Yang. *ab initio QM/MM and Free Energy Calculations of Enzyme Reactions*. Springer-Verlag, 2002.

[84] Y. Zhang. Improved pseudobonds for combined *ab initio* quantum mechanical/molecular mechanical methods. *J. Chem. Phys.*, 122(2):024114, 2005.

[85] Y. Zhang. Pseudobond *ab initio* QM/MM approach and its applications to enzyme reactions. *Theor. Chem. Acc.*, in press, 2005.

[86] Y. Zhang, J. Kua, and J. A. McCammon. Role of the catalytic triad and oxyanion hole in acetylcholinesterase catalysis: an *ab initio* QM/MM study. *J. Am. Chem. Soc.*, 124(35):10572–10577, 2002.

[87] *SYBYL 7.0*. Tripos Inc., 1699 South Hanley Rd., St. Louis, Missouri, 63144, USA.

[88] G. M. Torrie and J. P. Valleau. Monte Carlo free-energy estimates using non-boltzmann sampling - application to subcritical lennard-jones fluid. *Chem. Phys. Lett.*, 28(4):578–581, 1974.

[89] Valleau J.P. and Torrie G.M. *A guide for Monte Carlo for statistical mechanics.* Plenum Press, Inc., New York, 1977.

[90] C. Bartels and M. Karplus. Probability distributions for complex systems: adaptive umbrella sampling of the potential energy. *J. Phys. Chem. B*, 102(5):865–880, 1998.

[91] S. Kumar, D. Bouzida, R. H. Swendsen, P. A. Kollman, and J. M. Rosenberg. The weighted histogram analysis method for free-energy calculations on biomolecules .1. the method. *J. Comput. Chem.*, 13(8):1011–1021, 1992.

[92] M. J. Frisch, G. W. Trucks, H. B. Schlegel, G. E. Scuseria, M. A. Robb, J. R. Cheeseman, G. A. Petersson T. Keith, J. A. Montgomery, K. Raghavachari, M. A. Al-Laham, V. G. Zakrzewski, J. V. Ortiz, J. B. Foresman, J. Cioslowski, B. B. Stefanov, A. Nanayakkara, M. Challacombe, C. Y. Peng, P. Y. Ayala, P. M. W. Gill, B. G. Johnson, W. Chen, M. W. Wong, J. L. Andres, E. S. Replogle, R. Gomperts, R. L. Martin, D. J. Fox, J. S. Binkley, D. J. Defrees, J. Baker, J. P. Stewart, M. Head-Gordon, C. Gonzalez, and J. A. Pople. *Gaussian 98, Revision A.11*. Gaussian, Inc., Pittsburgh PA, 1998.

[93] J. A. McCammon and S. C. Harvey. Dynamics of Proteins and nucleic Acids. Cambridge Univ. Press, Cambridge, U.K., 1986.

[94] T. H. Rod, J. L. Radkiewicz, and C. L. Brooks. Correlated motion and the effect of distal mutations in dihydrofolate reductase. *Proc. Natl. Acad. Sci. U. S. A.*, 100(12):6980–6985, 2003.

[95] J. L. Radkiewicz and C. L. Brooks. Protein dynamics in enzymatic catalysis: exploration of dihydrofolate reductase. *J. Am. Chem. Soc.*, 122(2):225–231, 2000.

[96] T. Ichiye and M. Karplus. Collective motions in proteins - a covariance analysis of atomic fluctuations in molecular-dynamics and normal mode simulations. *Proteins*, 11(3):205–217, 1991.

[97] S. Swaminathan, W. E. Harte, and D. L. Beveridge. Investigation of domain-structure in proteins via molecular-dynamics simulation - application to hiv-1 protease dimer. *J. Am. Chem. Soc.*, 113(7):2717–2721, 1991.

[98] A. E. Garcia. Large-amplitude nonlinear motions in proteins. *Phys. Rev. Lett.*, 68(17):2696–2699, 1992.

[99] A. Amadei, A. B. M. Linssen, and H. J. C. Berendsen. Essential dynamics of proteins. *Proteins*, 17(4):412–425, 1993.

[100] S. Hayward, A. Kitao, F. Hirata, and N. Go. Effect of solvent on collective motions in globular protein. *J. Mol. Biol.*, 234(4):1207–1217, 1993.

[101] M. A. Balsera, W. Wriggers, Y. Oono, and K. Schulten. Principal component analysis and long time protein dynamics. *J. Phys. Chem.*, 100(7):2567–2572, 1996.

[102] O. M. Becker. Geometric versus topological clustering: an insight into conformation mapping. *Proteins*, 27(2):213–226, 1997.

[103] K. Tai, T. Shen, U. Borjesson, M. Philippopoulos, and J. A. McCammon. Analysis of a 10-ns molecular dynamics simulation of mouse acetylcholinesterase. *Biophys. J.*, 81(2):715–724, 2001.

[104] C. G. Sridhar, W. A. Hines, and E. T. Samulski. Polypeptide liquid-crystals - magnetic-susceptibility, twist elastic-constant, rotational viscosity coefficient, and poly-gamma-benzyl-l-glutamate sidechain conformation. *J. Chem. Phys.*, 61(3):947–953, 1974.

[105] J. W. Verhoeven. Glossary of terms used in photochemistry. *Pure Appl. Chem.*, 68(12):2223–2286, 1996.

[106] E. D. Lowe, M. E. M. Noble, V. T. Skamnaki, N. G. Oikonomakos, D. J. Owen, and L. N. Johnson. The crystal structure of a phosphorylase kinase peptide substrate complex: kinase substrate recognition. *Embo J.*, 16(22):6646–6658, 1997.

[107] V. T. Skamnaki, D. J. Owen, M. E. M. Noble, E. D. Lowe, G. Lowe, N. G. Oikonomakos, and L. N. Johnson. Catalytic mechanism of phosphorylase kinase probed by mutational studies. *Biochemistry*, 38(44):14718–14730, 1999.

[108] B. Hess. Similarities between principal components of protein dynamics and random diffusion. *Phys. Rev. E*, 62(6):8438–8448, 2000.

[109] B. Lu, C. F. Wong, and J. A. McCammon. Release of ADP from the catalytic subunit of protein kinase a: a molecular dynamics simulation study. *Protein Sci.*, 14(1):159–168, 2005.

[110] T. L. Rosenberry. Acetylcholinesterase. *Adv. Enzymol. Relat. Areas Mol. Biol.*, 43:103–218, 1975.

[111] M. Schumacher, S. Camp, Y. Maulet, M. Newton, K. Macpheequigley, S. S. Taylor, T. Friedmann, and P. Taylor. Primary structure of acetylcholinesterase - implications for regulation and function. *Fed. Proc.*, 45(13):2976–2981, 1986.

[112] P. Taylor. The Pharmacological Basis of Therapeutics. MacMillan, New York, 1985.

[113] A. Contestabile, T. Fila, R. Bartesaghi, A. Contestabile, and E. Ciani. Choline acetyltransferase activity at different ages in brain of Ts65Dn mice, an animal model for down's syndrome and related neurodegenerative diseases. *J. Neurochem.*, 97(2):515–526, 2006.

[114] L. Piazzi, A. Rampa, A. Bisi, S. Gobbi, F. Belluti, A. Cavalli, M. Bartolini, V. Andrisano, P. Valenti, and M. Recanatini. 3-(4-{[benzyl(methyl)amino]methyl}-phenyl)-6,7-dimethoxy-2h-2-chromenone (AP2238) inhibits both acetylcholinesterase and acetylcholinesterase-induced beta-amyloid aggregation: a dual function lead for alzheimer's disease therapy. *J. Med. Chem.*, 46(12):2279–2282, 2003.

[115] S. O. Bachurin. Medicinal chemistry approaches for the treatment and prevention of alzheimer disease. *Med. Res. Rev.*, 23(1):48–88, 2003.

[116] J. J. Sramek, V. Zarotsky, and N. R. Cutler. Review of drug development and therapeutic role of cholinesterase inhibitors in alzheimer's disease. *Drug Dev. Res.*, 56(3):347–353, 2002.

[117] G. Kryger, I. Silman, and J. L. Sussman. Structure of acetylcholinesterase complexed with E2020 (aricept (r)): implications for the design of new anti-alzheimer drugs. *Struct. Fold. Des.*, 7(3):297–307, 1999.

[118] T. M. Egan and R. A. North. Acetylcholine hyperpolarizes central neurons by acting on an M2 muscarinic receptor. *Nature*, 319(6052):405–407, 1986.

[119] J. L. Sussman, M. Harel, F. Frolow, C. Oefner, A. Goldman, L. Toker, and I. Silman. Atomic-structure of acetylcholinesterase from torpedo-californica - a prototypic acetylcholine-binding protein. *Science*, 253(5022):872–879, 1991.

[120] M. Bazelyansky, E. Robey, and J. F. Kirsch. Fractional diffusion-limited component of reactions catalyzed by acetylcholinesterase. *Biochemistry*, 25(1):125–130, 1986.

[121] B. B. Hasinoff. Kinetics of acetylthiocholine binding to electric-eel acetylcholinesterase in glycerol water solvents of increased viscosity - evidence for a diffusion-controlled reaction. *Biochim. Biophys. Acta*, 704(1):52–58, 1982.

[122] H. J. Nolte, T. L. Rosenberry, and E. Neumann. Effective charge on acetylcholinesterase active-sites determined from the ionic-strength dependence of association rate constants with cationic ligands. *Biochemistry*, 19(16):3705–3711, 1980.

[123] *Amino acids and numbers refer to mouse or Human AChE, and the numbers in parentheses refer to the positions of analogous residues in TcAChE.*

[124] A. Shafferman, C. Kronman, Y. Flashner, M. Leitner, H. Grosfeld, A. Ordentlich, Y. Gozes, S. Cohen, N. Ariel, D. Barak, M. Harel, I. Silman, J. L. Sussman, and B. Velan. Mutagenesis of human acetylcholinesterase - identification of residues involved in catalytic activity and in polypeptide folding. *J. Biol. Chem.*, 267(25):17640–17648, 1992.

[125] D. M. Quinn. Acetylcholinesterase - enzyme structure, reaction dynamics, and virtual transition-states. *Chem. Rev.*, 87(5):955–979, 1987.

[126] D. Quinn, R. Medhekar, and N. Baker. *Ester hydrolysis.* Elsevier Science, Oxford, U.K., 1999.

[127] G. Dodson and A. Wlodawer. Catalytic triads and their relatives. *Trends Biochem.Sci.*, 23(9):347–352, 1998.

[128] D. M. Blow, J. J. Birktoft, and B. S. Hartley. Role of a buried acid group in mechanism of action of chymotrypsin. *Nature*, 221(5178):337–340, 1969.

[129] W. W. Bachovchin and J. D. Roberts. N-15 nuclear magnetic-resonance spectroscopy - state of histidine in catalytic triad of alpha-lytic protease - implications for charge-relay mechanism of peptide-bond cleavage by serine proteases. *J. Am. Chem. Soc.*, 100(26):8041–8047, 1978.

[130] H. Tachikawa, M. Igarashi, J. Nishihira, and T. Ishibashi. *ab initio* model study on acetylcholinesterase catalysis: potential energy surfaces of the proton transfer reactions. *J. Photochem. Photobiol. B-Biol.*, 79(1):11–23, 2005.

[131] J. A. Gerlt and P. G. Gassman. An explanation for rapid enzyme-catalyzed proton abstraction from carbon acids - importance of late transition-states in concerted mechanisms. *J. Am. Chem. Soc.*, 115(24):11552–11568, 1993.

[132] J. A. Gerlt and P. G. Gassman. Understanding the rates of certain enzyme-catalyzed reactions - proton abstraction from carbon acids, acyl-transfer reactions, and displacement-reactions of phosphodiesters. *Biochemistry*, 32(45):11943–11952, 1993.

[133] W. W. Cleland and M. M. Kreevoy. Low-barrier hydrogen-bonds and enzymatic catalysis. *Science*, 264(5167):1887–1890, 1994.

[134] P. A. Frey, S. A. Whitt, and J. B. Tobin. A low-barrier hydrogen-bond in the catalytic triad of serine proteases. *Science*, 264(5167):1927–1930, 1994.

[135] M. A. Massiah, C. Viragh, P. M. Reddy, I. M. Kovach, J. Johnson, T. L. Rosenberry, and A. S. Mildvan. Short, strong hydrogen bonds at the active site of human acetylcholinesterase: proton nmr studies. *Biochemistry*, 40(19):5682–5690, 2001.

[136] G. R. Stranzl, K. Gruber, G. Steinkellner, K. Zangger, H. Schwab, and C. Kratky. Observation of a short, strong hydrogen bond in the active site of hydroxynitrile lyase from hevea brasiliensis explains a large pk(a) shift of the catalytic base induced by the reaction intermediate. *J. Biol. Chem.*, 279(5):3699–3707, 2004.

[137] L. Zhao, H. Liao, and M. D. Tsai. The catalytic role of aspartate in a short strong hydrogen bond of the ASP(274)-HIS(32) catalytic dyad in phosphatidylinositol-specific phospholipase c can be substituted by a chloride ion. *J. Biol. Chem.*, 279(31):31995–32000, 2004.

[138] A. Warshel, G. Narayszabo, F. Sussman, and J. K. Hwang. How do serine proteases really work. *Biochemistry*, 28(9):3629–3637, 1989.

[139] M. Fuxreiter and A. Warshel. Origin of the catalytic power of acetylcholinesterase: computer simulation studies. *J. Am. Chem. Soc.*, 120(1):183–194, 1998.

[140] G. Katona, R. C. Wilmouth, P. A. Wright, G. I. Berglund, J. Hajdu, R. Neutze, and C. J. Schofield. X-ray structure of a serine protease acyl-enzyme complex at 0.95-angstrom resolution. *J. Biol. Chem.*, 277(24):21962–21970, 2002.

[141] M. Topf, P. Varnai, and W. G. Richards. *ab initio* QM/MM dynamics simulation of the tetrahedral intermediate of serine proteases: insights into the active site hydrogen-bonding network. *J. Am. Chem. Soc.*, 124(49):14780–14788, 2002.

[142] T. Ishida. Low-barrier hydrogen bond hypothesis in the catalytic triad residue of serine proteases: correlation between structural rearrangement and chemical shifts in the acylation process. *Biochemistry*, 45(17):5413–5420, 2006.

[143] A. Shafferman, D. Barak, D. Kaplan, A. Ordentlich, C. Kronman, and B. Velan. Functional requirements for the optimal catalytic configuration of the ache active center. *Chem.-Biol. Interact.*, 157:123–131, 2005.

[144] M. Behra, X. Cousin, C. Bertrand, J. L. Vonesch, D. Biellmann, A. Chatonnet, and U. Strahle. Acetylcholinesterase is required for neuronal and muscular development in the zebrafish embryo. *Nat. Neurosci.*, 5(2):111–118, 2002.

[145] Y. Bourne, Z. Radić, G. Sulzenbacher, E. Kim, P. Taylor, and P. Marchot. Substrate and product trafficking through the active center gorge of acetylcholinesterase analyzed by crystallography and equilibrium binding. *J. Biol. Chem.*, 281(39):29256–29267, 2006.

[146] *"W", "M", "T^+" and "T^0" represent the wild-type mAChE, H447I mutant, TFK^+ and TFK^0 respectively; [X-Y] and [$X \cdot Y$] represent the covalent and noncovalent complexes of the X enzyme and Y ligand, respectively.*

[147] *InsightII, Version 2000.1*. Accelrys Software Inc., San Diego, CA, 2000.

[148] D.A. Case, T.A. Darden, III T.E. Cheatham, C.L. Simmerling, J. Wang, R.E. Duke, R. Luo, K.M. Merz, B. Wang, D.A. Pearlman, M. Crowley, S. Brozell, V. Tsui, H. Gohlke, J. Mongan, V. Hornak, G. Cui, P. Beroza, C. Schafmeister, J.W. Caldwell, W.S. Ross, and P.A. Kollman. *Amber 8.0*. University of California, San Francisco, CA., 2004.

[149] J. Kua, Y. K. Zhang, and J. A. McCammon. Studying enzyme binding specificity in acetylcholinesterase using a combined molecular dynamics and multiple docking approach. *J. Am. Chem. Soc.*, 124(28):8260–8267, 2002.

[150] G. M. Morris, D. S. Goodsell, R. S. Halliday, R. Huey, W. E. Hart, R. K. Belew, and A. J. Olson. Automated docking using a lamarckian genetic algorithm and an empirical binding free energy function. *J. Comput. Chem.*, 19(14):1639–1662, 1998.

[151] P. Hu and Y. K. Zhang. Catalytic mechanism and product specificity of the histone lysine methyltransferase SET7/9: an *ab initio* QM/MM-FE study with multiple initial structures. *J. Am. Chem. Soc.*, 128(4):1272–1278, 2006.

[152] Y. H. Cheng, Y. K. Zhang, and J. A. McCammon. How does activation loop phosphorylation modulate catalytic activity in the cAMP-dependent protein kinase: A theoretical study. *Protein Sci.*, 15(4):672–683, 2006.

[153] W. L. Jorgensen, J. Chandrasekhar, J. D. Madura, R. W. Impey, and M. L. Klein. Comparison of simple potential functions for simulating liquid water. *J. Chem. Phys.*, 79(2):926–935, 1983.

[154] M. A. L. Eriksson and L. Nilsson. Structural and dynamic differences of the estrogen receptor dna binding domain, binding as a dimer and as a monomer to dna: molecular dynamics simulation studies. *Eur. Biophys. J. Biophys. Lett.*, 28(2):102–111, 1999.

[155] S. Y. Sheu, D. Yang, H. L. Selzle, and E. W. Schlag. Energetics of hydrogen bonds in peptides. *Proc. Natl. Acad. Sci. U. S. A.*, 100(22):12683–12687, 2003.

[156] A. Ordentlich, D. Barak, C. Kronman, N. Ariel, Y. Segall, B. Velan, and A. Shafferman. Functional characteristics of the oxyanion hole in human acetylcholinesterase. *J. Biol. Chem.*, 273(31):19509–19517, 1998.

[157] J. E. Stok, A. Goloshchapov, C. Song, C. E. Wheelock, M. B. H. Derbel, C. Morisseau, and B. D. Hammock. Investigation of the role of a second conserved serine in carboxylesterases via site-directed mutagenesis. *Arch. Biochem. Biophys.*, 430(2):247–255, 2004.

[158] D. L. Ermak and J. A. McCammon. Brownian dynamics with hydrodynamic interactions. *J. Chem. Phys.*, 69(4):1352–1360, 1978.

[159] S. H. Northrup, S. A. Allison, and J. A. McCammon. Brownian dynamics simulation of diffusion-influenced bimolecular reactions. *J. Chem. Phys.*, 80(4):1517–1526, 1984.

[160] N. Agmon and A. L. Edelstein. Collective binding properties of receptor arrays. *Biophys. J.*, 72(4):1582–1594, 1997.

[161] R. R. Gabdoulline and R. C. Wade. Brownian dynamics simulation of protein-protein diffusional encounter. *Methods*, 14(3):329–341, 1998.

[162] J. R. Stiles and T. M. Bartol. Monte Carlo methods for simulating realistic synaptic microphysiology using MCell. In E. De Schutter, editor, *Computational Neuroscience: Realistic Modeling for Experimentalists*, pages 87–127. CRC Press, Inc., New York, 2000.

[163] J. L. Smart and J. A. McCammon. Analysis of synaptic transmission in the neuromuscular junction using a continuum finite element model. *Biophys. J.*, 75(4):1679–1688, 1998.

[164] M. G. Kurnikova, R. D. Coalson, P. Graf, and A. Nitzan. A lattice relaxation algorithm for three-dimensional poisson-nernst-planck theory with application to ion transport through the gramicidin a channel. *Biophys. J.*, 76(2):642–656, 1999.

[165] Z. Schuss, B. Nadler, and R. S. Eisenberg. Derivation of poisson and nernst-planck equations in a bath and channel from a molecular model. *Phys. Rev. E*, 6403(3), 2001.

[166] Y. H. Song, Y. J. Zhang, C. L. Bajaj, and N. A. Baker. Continuum diffusion reaction rate calculations of wild-type and mutant mouse acetylcholinesterase: adaptive finite element analysis. *Biophys. J.*, 87(3):1558–1566, 2004.

[167] Y. H. Song, Y. J. Zhang, T. Y. Shen, C. L. Bajaj, A. McCammon, and N. A. Baker. Finite element solution of the steady-state smoluchowski equation for rate constant calculations. *Biophys. J.*, 86(4):2017–2029, 2004.

[168] H. Berry. Monte Carlo simulations of enzyme reactions in two dimensions: fractal kinetics and spatial segregation. *Biophys. J.*, 83(4):1891–1901, 2002.

[169] D. Genest. A Monte Carlo simulation study of the influence of internal motions on the molecular-conformation deduced from two-dimensional nmr experiments. *Biopolymers*, 28(11):1903–1911, 1989.

[170] M. J. Saxton. Lateral diffusion and aggregation - a Monte Carlo study. *Biophys. J.*, 61(1):119–128, 1992.

[171] J. A. McCammon. Computer-aided molecular design. *Science*, 238(4826):486–491, 1987.

[172] S. H. Northrup, J. O. Boles, and J. C. L. Reynolds. Brownian dynamics of cytochrome-c and cytochrome-c peroxidase association. *Science*, 241(4861):67–70, 1988.

[173] R. C. Wade, M. E. Davis, B. A. Luty, J. D. Madura, and J. A. McCammon. Gating of the active-site of triose phosphate isomerase - brownian dynamics simulations of flexible peptide loops in the enzyme. *Biophys. J.*, 64(1):9–15, 1993.

[174] P. Eastman and S. Doniach. Multiple time step diffusive langevin dynamics for proteins. *Proteins*, 30(3):215–227, 1998.

[175] L. Yeomans-Reyna and M. Medina-Noyola. Self-consistent generalized langevin equation for colloid dynamics. *Phys Rev E Stat Nonlin Soft Matter Phys.*, 64(6):066114, 2001.

[176] D. Q. Zhang, J. Suen, Y. J. Zhang, Y. H. Song, Z. Radić, P. Taylor, M. J. Holst, C. Bajaj, N. A. Baker, and J. A. McCammon. Tetrameric mouse acetylcholinesterase: continuum diffusion rate calculations by solving the steady-state Smoluchowski equation using finite element methods. *Biophys. J.*, 88(3):1659–1665, 2005.

[177] J. Wang. Diffusion and single molecule dynamics on biomolecular interface binding energy landscape. *Chem. Phys. Lett.*, 418(4-6):544–548, 2006.

[178] J. M. Berg, J. L. Tymoczko, and L. Stryer. In *Biochemistry*. W. H. Freeman & Co., New York, NY, 1995.

[179] H. A. Berman, K. Leonard, and M. W. Nowak. In *Cholinesterases: Structure, Function, Mechanism, Genetics and Cell Biology.* American Chemical Society, Washington, DC., 1991. J. Massoulie, editor.

[180] Y. Bourne, P. Taylor, and P. Marchot. Acetylcholinesterase inhibition by fasciculin - crystal-structure of the complex. *Cell*, 83(3):503–512, 1995.

[181] L. W. Velsor, C. A. Ballinger, J. Patel, and E. M. Postlethwait. Influence of epithelial lining fluid lipids on NO_2-induced membrane oxidation and nitration. *Free Radic. Biol. Med.*, 34(6):720–733, 2003.

[182] R. C. Tan, T. N. Truong, J. A. McCammon, and J. L. Sussman. Acetylcholinesterase - electrostatic steering increases the rate of ligand-binding. *Biochemistry*, 32(2):401–403, 1993.

[183] S. Tara, A. H. Elcock, J. M. Briggs, Z. Radić, P. Taylor, and J. A. McCammon. Rapid binding of a cationic active site inhibitor to wild type and mutant mouse acetylcholinesterase: brownian dynamics simulation including diffusion in the active site gorge. *Biopolymers*, 46(7):465–474, 1998.

[184] H. X. Zhou. On the calculation of diffusive reaction-rates using brownian dynamics simulations. *J. Chem. Phys.*, 92(5):3092–3095, 1990.

[185] H. X. Zhou, S. T. Wlodek, and J. A. McCammon. Conformation gating as a mechanism for enzyme specificity. *Proc. Natl. Acad. Sci. U. S. A.*, 95(16):9280–9283, 1998.

[186] H. X. Zhou, J. M. Briggs, S. Tara, and J. A. McCammon. Correlation between rate of enzyme-substrate diffusional encounter and average boltzmann factor around active site. *Biopolymers*, 45(5):355–360, 1998.

[187] O. Axelsson and V. A. Barker. In *Finite Element Solution of Boundary Value Problems. Theory and Computation.* Society for Industrial and Applied Mathematics, Philadelphia, PA., 2001.

[188] M. Holst, N. Baker, and F. Wang. Adaptive multilevel finite element solution of the poisson-boltzmann equation i. algorithms and examples. *J. Comput. Chem.*, 21(15):1319–1342, 2000.

[189] N. Baker, M. Holst, and F. Wang. Adaptive multilevel finite element solution of the poisson-boltzmann equation ii. refinement at solvent-accessible surfaces in biomolecular systems. *J. Comput. Chem.*, 21(15):1343–1352, 2000.

[190] M. Holst. Adaptive numerical treatment of elliptic systems on manifolds. *Adv. Comput. Math.*, 15(1-4):139–191, 2001.

[191] D Braess. In *Finite Elements: Theory, Fast Solvers, and Applications in Solid Mechanics.* Cambridge University Press, New York, NY, 1997.

[192] B. Z. Lu, X. L. Cheng, T. J. Hou, and J. A. McCammon. Calculation of the maxwell stress tensor and the poisson-boltzmann force on a solvated molecular surface using hypersingular boundary integrals. *J. Chem. Phys.*, 123(8), 2005.

[193] B. Z. Lu, D. Q. Zhang, and J. A. McCammon. Computation of electrostatic forces between solvated molecules determined by the poisson-boltzmann equation using a boundary element method. *J. Chem. Phys.*, 122(21), 2005.

[194] W. Humphrey, A. Dalke, and K. Schulten. Vmd: visual molecular dynamics. *J. Mol. Graph.*, 14(1):33–38, 1996.

[195] Y. J. Zhang, C. L. Bajaj, and B. S. Sohn. Adaptive and quality 3-D meshing from imaging data. In *Proc. 8th ACM Symposium on Solid Modeling and Applications.*, page 286291. ACM Press, Seattle, WA., 2003.

[196] Y. J. Zhang, C. L. Bajaj, and B. S. Sohn. 3d finite element meshing from imaging data. *the special issue of Computer Methods in Applied Mechanics and Engineering (CMAME) on Unstructured Mesh generation*, 194(48-49):5083–5106, 2004.

[197] Y. J. Zhang, G. L. Xu, and C. Bajaj. Quality meshing of implicit solvation models of biomolecular structures. *Comput. Aided Geom. Des.*, 23(6):510–530, 2006.

[198] E. B. Krissinel and N. Agmon. Spherical symmetric diffusion problem. *J. Comput. Chem.*, 17(9):1085–1098, 1996.

[199] D. M. Quinn, J. Seravalli, H. K. Nair, R. Medhekar, B. Husseini, Z. Radić, D. C. Vellom, N. Pickering, and P. Taylor. The function of electrostatics in acetylcholinesterase catalysis. In *Enzymes of the Cholinesterase Family.*, page 203207. Plenum Publishing, New York, NY, 1995. D. M. Quinn, A. S. Balasubramanian, B. P. Doctor, and P. Taylor, editors.

[200] M. Holst and S. Vandewalle. Schwarz methods: to symmetrize or not to symmetrize. *SIAM J. Numer. Anal.*, 34(2):699–722, 1997.

[201] A. Saxena, R. S. Hur, C. Y. Luo, and B. P. Doctor. Natural monomeric form of fetal bovine serum acetylcholinesterase lacks the C-terminal tetramerization domain. *Biochemistry*, 42(51):15292–15299, 2003.

[202] S. A. Allison. Boundary element modeling of biomolecular transport. *Biophys. Chem.*, 93(2-3):197–213, 2001.

[203] C. M. Cortis and R. A. Friesner. Numerical solution of the poisson-boltzmann equation using tetrahedral finite-element meshes. *J. Comput. Chem.*, 18(13):1591–1608, 1997.

[204] C. M. Cortis and R. A. Friesner. An automatic three-dimensional finite element mesh generation system for the poisson-boltzmann equation. *J. Comput. Chem.*, 18(13):1570–1590, 1997.

[205] Y. H. Cheng, J. K. Suen, Z. Radić, S. D. Bond, M. J. Holst, and J. A. McCmmon. Continuum simulations of acetylcholine diffusion with reaction-determined boundaries in neuromuscular junction models. *Biophys. Chem.*, 127(3):129–139, 2007.

[206] J. C. Wathey, M. M. Nass, and H. A. Lester. Numerical reconstruction of the quantal event at nicotinic synapses. *Biophys. J.*, 27(1):145–164, 1979.

[207] A. Friboulet and D. Thomas. Reaction diffusion coupling in a structured system - application to the quantitative simulation of end-plate currents. *J. Theor. Biol.*, 160(4):441–455, 1993.

[208] T. Nagado, K. Arimura, Y. Sonoda, A. Kurono, Y. Horikiri, A. Kameyama, M. Kameyama, O. Pongs, and M. Osame. Potassium current suppression in patients with peripheral nerve hyperexcitability. *Brain*, 122:2057–2066, 1999.

[209] A. B. Smit, N. I. Syed, D. Schaap, J. van Minnen, J. Klumperman, K. S. Kits, H. Lodder, R. C. van der Schors, R. van Elk, B. Sorgedrager, K. Brejc, T. K. Sixma, and W. P. M. Geraerts. A glia-derived acetylcholine-binding protein that modulates synaptic transmission. *Nature*, 411(6835):261–268, 2001.

[210] M. Harel, R. Kasher, A. Nicolas, J. M. Guss, M. Balass, M. Fridkin, A. B. Smit, K. Brejc, T. K. Sixma, E. Katchalski-katzir, J. L. Sussman, and S. Fuchs. The binding site of acetylcholine receptor as visualized in the X-ray structure of a complex between alpha-bungarotoxin and a mimotope peptide. *Neuron*, 32(2):265–275, 2001.

[211] S. M. Sine and A. G. Engel. Recent advances in cys-loop receptor structure and function. *Nature*, 440(7083):448–455, 2006.

[212] A. Miyazawa, Y. Fujiyoshi, and N. Unwin. Structure and gating mechanism of the acetylcholine receptor pore. *Nature*, 423(6943):949–955, 2003.

[213] N. Unwin. Structure and action of the nicotinic acetylcholine receptor explored by electron microscopy. *FEBS Lett.*, 555(1):91–95, 2003.

[214] N. Unwin. Refined structure of the nicotinic acetylcholine receptor at 4 angstrom resolution. *J. Mol. Biol.*, 346(4):967–989, 2005.

[215] P. Taylor. Anticholinesterase agents. In *The Pharmacological Basis of Therapeutics*, pages 161–176. McGraw-Hill, New York., 1996. J. G. Hardman, L. E. Limbird, P. B. Molinoff, R. W. Ruddon, and A. G. Gilman, editors.

[216] T. Shen, K. Tai, R. Henchman, and J. A. McCammon. Molecular dynamics of acetylcholinesterase. *Acc. Chem. Res.*, 35(6):332–340, 2002.

[217] A. Karlin. Emerging structure of the nicotinic acetylcholine receptors. *Nat. Rev. Neurosci.*, 3(2):102–114, 2002.

[218] R. Bertram. A simple model of transmitter release and facilitation. *Neural. Comput.*, 9(3):515–523, 1997.

[219] R. Bertram, A. Sherman, and E. F. Stanley. Single-domain/bound calcium hypothesis of transmitter release and facilitation. *J. Neurophysiol.*, 75(5):1919–1931, 1996.

[220] P. J. Kruk, H. Korn, and D. S. Faber. The effects of geometrical parameters on synaptic transmission: a Monte Carlo simulation study. *Biophys. J.*, 73(6):2874–2890, 1997.

[221] L. M. Wahl, C. Pouzat, and K. J. Stratford. Monte Carlo simulation of fast excitatory synaptic transmission at a hippocampal synapse. *J. Neurophysiol.*, 75(2):597–608, 1996.

[222] T. Naka and N. Sakamoto. Localization effects of acetylcholine release from a synaptic vesicle at the neuromuscular junction. *Biosystems*, 51(2):73–78, 1999.

[223] T. Ghaffari-farazi, J. S. Liaw, and T. W. Berger. Consequence of morphological alterations on synaptic function. *Neurocomputing*, 26-7:17–27, 1999.

[224] T. Naka. Evaluation of characteristic parameters for the neurotransmitter release mechanisms at the neuromuscular junction. *Biosystems*, 49(2):143–149, 1999.

[225] T. Naka. Simulation analysis of the effects of the junctional folds on spontaneous generation of the miniature endplate current at neuromuscular junction. *Math. Comput. Simul.*, 46(5-6):631–639, 1998.

[226] S. Aharon, M. Bercovier, and H. Parnas. Parallel computation enables precise description of Ca2+ distribution in nerve terminals. *Bull. Math. Biol.*, 58(6):1075–1097, 1996.

[227] R. L. Cooper, J. L. Winslow, C. K. Govind, and H. L. Atwood. Synaptic structural complexity as a factor enhancing probability of calcium-mediated transmitter release. *J. Neurophysiol.*, 75(6):2451–2466, 1996.

[228] W. M. Yamada and R. S. Zucker. Time course of transmitter release calculated from simulations of a calcium diffusion-model. *Biophys. J.*, 61(3):671–682, 1992.

[229] H. Parnas, G. Hovav, and I. Parnas. Effect of Ca^{2+} diffusion on the time course of neurotransmitter release. *Biophys. J.*, 55(5):859–874, 1989.

[230] R. S. Zucker and N. Stockbridge. Pre-synaptic calcium diffusion and the time courses of transmitter release and synaptic facilitation at the squid giant synapse. *J. Neurosci.*, 3(6):1263–1269, 1983.

[231] O. Axelsson and V. A. Baker. Finite element solution of boundary value problems. In *Theory and Computation*. Academic Press, San Diego, 1984.

[232] J. R. Stiles, T. M. Bartol, M. M. Salpeter, and T. J. Sejnowski. Synaptic variability: new insights from reconstructions and Monte Carlo simulations with MCell. In W. M. Cowan, T. C. Sudhof, and C. F. Stevens, editors, *Synapses*, pages 681–731. Johns Hopkins University Press, Baltimore, Maryland., 2001.

[233] J. S. Coggan, T. M. Bartol, E. Esquenazi, J. R. Stiles, S. Lamont, M. E. Martone, D. K. Berg, M. H. Ellisman, and T. J. Sejnowski. Evidence for ectopic neurotransmission at a neuronal synapse. *Science*, 309(5733):446–451, 2005.

[234] Z. Radić, N. A. Pickering, D. C. Vellom, S. Camp, and P. Taylor. 3 distinct domains in the cholinesterase molecule confer selectivity for acetylcholinesterase and butyrylcholinesterase inhibitors. *Biochemistry*, 32(45):12074–12084, 1993.

[235] Z. Kovarik, Z. Radić, H. A. Berman, V. Simeon-rudolf, E. Reiner, and P. Taylor. Acetylcholinesterase active centre and gorge conformations analysed by combinatorial mutations and enantiomeric phosphonates. *Biochem. J.*, 373:33–40, 2003.

[236] Y. Bourne, P. Taylor, Z. Radic, and P. Marchot. Structural insights into ligand interactions at the acetylcholinesterase peripheral anionic site. *Embo J.*, 22(1):1–12, 2003.

[237] N. Unwin, A. Miyazawa, J. Li, and Y. Fujiyoshi. Activation of the nicotinic acetylcholine receptor involves a switch in conformation of the a subunits. *J. Mol. Biol.*, 319(5):1165–1176, 2002.

[238] B. R. Land, W. V. Harris, E. E. Salpeter, and M. M. Salpeter. Diffusion and binding constants for acetylcholine derived from the falling phase of miniature endplate currents. *Proc. Natl. Acad. Sci. U. S. A.*, 81(5):1594–1598, 1984.

[239] C. Grosman and A. Auerbach. The dissociation of acetylcholine from open nicotinic receptor channels. *Proc. Natl. Acad. Sci. U. S. A.*, 98(24):14102–14107, 2001.

[240] F. N. Salamone, M. Zhou, and A. Auerbach. A re-examination of adult mouse nicotinic acetylcholine receptor channel activation kinetics. *J. Physiol.-London*, 516(2):315–330, 1999.

[241] C. Grosman, F. N. Salamone, S. M. Sine, and A. Auerbach. The extracellular linker of muscle acetylcholine receptor channels is a gating control element. *J. Gen. Physiol.*, 116(3):327–339, 2000.

[242] S. Fucik and A. Kufner. In *Nonlinear differential equations*. Elsevier Scientific Publishing Company, New York., 1980.

[243] W. Hackbusch. In *Elliptic differential equations*. Springer-Verlag, Berlin, Germany, 1994.

[244] Y. H. Cheng, J. Suen, D. Q. Zhang, S. Bond, Y. J. Zhang, Y. H. Song, N. Baker, C. Bajaj, M. Holst, and J. A. McCammon. Finite element analysis of the time-dependent smoluchowski equation for acetylcholinesterase reaction rate calculations. *Biophys. J.*, 92(10):3397–3406, 2007.

[245] J. Schöberl. Netgen: an advancing front 2D/3D-mesh generator based on abstract rules. *Comput. Visual Sci.*, 1:41–52, 1997.

[246] G. Akk and A. Auerbach. Activation of muscle nicotinic acetylcholine receptor channels by nicotinic and muscarinic agonists. *Br. J. Pharmacol.*, 128(7):1467–1476, 1999.

[247] J. H. Schwartz. Synaptic vesicles. In E. R. Kandel, J. H. Schwartz, and T. M. Jessell, editors, *Principles of Neural Science*, pages 225–234. Appleton and Lange, Norwalk, Connecticut., 1991.

[248] H. Zimmermann. In *Synaptic Transmission: Cellular and Molecular Basis*. Thieme, Stuttgart, Germany, 1993.

[249] T. C. Südhof and R. H. Scheller. Mechanism and regulation of neurotransmitter release. In *Synapses*. Johns Hopkins University Press, Baltimore, Maryland., 2000. W. M. Cowan, T. C. Südhof, and C. F. Stevens, editors.

[250] T. Naka, K. Shiba, and N. Sakamoto. A two-dimensional compartment model for the reaction-diffusion system of acetylcholine in the synaptic cleft at the neuromuscular junction. *Biosystems*, 41(1):17–27, 1997.

[251] K. L. Magleby and D. A. Terrar. Factors affecting time course of decay of endplate currents - possible cooperative action of acetylcholine on receptors at frog neuromuscular-junction. *J. Physiol.-London*, 244(2):467–495, 1975.

[252] B. Katz and R. Miledi. Binding of acetylcholine to receptors and its removal from synaptic cleft. *J. Physiol.-London*, 231(3):549–574, 1973.

[253] Y. J. Zhang, C. Bajaj, and B. S. Sohn. 3d finite element meshing from imaging data. *Comput. Meth. Appl. Mech. Eng.*, 194(48-49):5083–5106, 2005.